

Two-dimensional hybrid perovskites with alkylammonium cations for field-effect transistors

Shankeerthan Kalyanasundaram

Thesis supervisors:
Dr. Tomasz Marszalek
Prof. Wojciech Pisula

Responsible professor:
Prof. Steffen Strehle

A report submitted in partial fulfillment of the
requirements for the masters in micro and nanotechnologies

June 2022

Acknowledgment

I would like to express my sincere gratitude to Prof. Steffen Strehle, Dr. Tomasz Marszalek, Prof. Wojciech Pisula, and Prof. Paul Blom for the invaluable guidance and the prompt feedback throughout my master thesis. I would like to thank my colleague Shuanglong Wang for providing an introduction to perovskite device fabrication. I thankfully acknowledge the support and friendship that I received from my colleagues Zhitian Ling, Okan Yildiz, Abin Nas Nalakath, and Weichen Liu at Max Planck Institute for Polymer Research (MPIP) for the past eight months. I would also like to extend my thanks to Frank Keller, Verona Maus, Christian Bauer, Helma Burg, Sirma Koynova, and Petra Pausch of Max Planck Institute for Polymer Research for their outstanding technical and administrative support during my stay at MPIP. My special thanks to my family and friends for their constant support and love.

Zusammenfassung

Zweidimensionale (2D) organisch-anorganische Hybrid-Perowskite als eine spezielle Gruppe von Halbleitern mit abwechselnden organischen und anorganischen Schichten haben großes Interesse für Solarzellen und Leuchtdioden geweckt. Dies liegt an ihren natürlichen Vorteilen: den sperrigen hydrophoben organischen Kationen und dem dielektrischen Einschluss in der 2D-Schicht-Quantentopfstruktur, die im Vergleich zu ihren 3D-Gegenständen die Luftstabilität erheblich verbessern und die Ionenbewegung unterdrücken kann. Darüber hinaus wirkt sich die chemische Struktur der organischen Kationen stark auf die optoelektronischen Eigenschaften von 2D-Hybridhalogenid-Perowskiten und Bauelementen aus. Die Korrelation zwischen der chemischen Struktur des organischen Kations und dem Ladungsträgertransport in 2D-Perowskiten wird jedoch weniger beachtet. In dieser Studie untersuchen wir mit Hilfe eines Feldeffekttransistors (FET) den Ladungsträgertransport in Sn(II)-basierten 2D-Perowskit-Dünnschichten unter Verwendung von Zinnjodid-basierten 2D-Perowskiten mit organischen Spacern auf Alkylammoniumbasis. Es wird gezeigt, dass eine subtile Änderung der Molekularstruktur des organischen Kations die Kristallinität und Oberflächenmorphologie erheblich beeinflusst, was wiederum den Ladungsträgertransport in Perowskitfilmen in FETs bestimmt. Schließlich wird eine klare Korrelation zwischen der Anzahl der Kohlenstoffatome in der Alkylkette und der Mobilität der Bauelemente festgestellt.

Abstract

Two-dimensional (2D) organic-inorganic hybrid perovskites as a special group of semiconductors with alternating organic and inorganic layers have attracted extensive interest in solar cells and light-emitting diodes due to their natural advantages of bulky hydrophobic organic cations and dielectric confinement in 2D layered quantum well structure, which can significantly improve air stability and suppress ion movement compared to their 3D counterparts. In addition, the chemical structure of organic cations strongly impacts the optoelectronic properties of 2D hybrid halide perovskites and devices. However, less attention is being focused on understanding the correlation between the chemical structure of organic cation and in-plane charge carrier transport in 2D perovskites. In this study, we apply field-effect transistor (FET) to investigate the charge carrier transport in Sn(II) based 2D perovskites thin films by using tin-iodide-based 2D perovskites with alkyl ammonium-based organic spacers. It is demonstrated that a subtle change in the molecular structure of organic cation significantly impacts the crystallinity and surface morphology, which in turn, governs charge carrier transport in perovskite film in FETs. Finally, a clear correlation between the number of carbon atoms in the alkyl chain and device mobility is identified.

Contents

1	Introduction	1
1.1	Overview	1
1.2	Hybrid organic-inorganic perovskite	2
1.2.1	Three dimensional perovskites	2
1.2.2	Lower dimensional perovskites	4
1.3	Factors affecting the stability of hybrid perovskite	7
1.3.1	Moisture	8
1.3.2	Oxidation	8
1.3.3	Light illumination	9
1.3.4	Ion migration	10
1.4	Improving stability of hybrid perovskites	12
1.5	Advantages of 2D hybrid perovskite	13
1.6	Organic spacers for 2D hybrid perovskite	14
1.7	2D hybrid perovskite field-effect transistor	17
2	Experiments	20
2.1	The device preparations	20
2.1.1	The synthesis of 2D perovskite	20
2.1.2	Device fabrication	22
2.2	Characterization of 2D perovskite	23
2.2.1	Introduction	23
2.2.2	X-ray diffraction	24
2.2.3	Grazing incidence wide angle X-ray scattering	25
2.2.4	Ultra-violet visible spectroscopy	27
2.2.5	Optical microscopy	28

2.2.6	Atomic force microscopy	29
2.3	Device measurement	29
3	Results and discussion	30
3.1	Optoelectronic properties	30
3.2	Structural properties	35
3.3	Device performance	41
3.3.1	Charge carrier mobility	43
3.3.2	Hysteresis	48
3.3.3	Threshold voltage	48
4	Conclusion	50
5	Appendices	vii
A	Optical microscopy	vii
B	Atomic force microscopy	viii
C	Grazing incidence wide angle X-ray scattering	x
D	Device measurement	xii
	Declaration of originality	xvi

Motivation

Two-dimensional hybrid perovskite field-effect transistors are a promising alternative to organic transistors, which have been explored since 1999. Over the past two decades, remarkable progress has been made in improving the charge carrier mobility of 2D perovskite field-effect transistors. Even though the medium for the charge transfer is inorganic layers in the layered structure of 2D perovskites, the organic spacers are also known to influence the charge transport properties. However, the influence of the chemical structure of organic cations on charge carrier transport is not fully understood. More specifically, the correlation between molecular self-assembly properties and supramolecular structure of various cations and their influence on charge carrier transport has not been identified. Understanding the correlation between organic spacers and charge carrier mobility will provide a theoretical basis for selecting suitable novel organic cations for 2D hybrid perovskites. Also, understanding the influence of organic spacers on the micro and macro structure and surface morphology of thin perovskite film would help reduce charge carrier trapping at the grain boundaries and improve environmental stability. The simple chemical structure of alkyl ammonium cations made it an ideal candidate for studying the effects mentioned above. In this study, tin-iodide-based 2D perovskites with alkyl ammonium-based organic spacers starting from propylammonium ($\text{CH}_3(\text{CH}_2)_2\text{NH}_3^+$) to heptanammonium ($\text{CH}_3(\text{CH}_2)_6\text{NH}_3^+$) are used to understand the effect on intrinsic and extrinsic factors relevant to charge carrier transport.

Chapter 1

Introduction

1.1 Overview

The name perovskite was initially given to calcium titanium oxide (CaTiO_3) mineral, which was discovered in the Ural mountains in 1839 and named after mineralogist Lev Perovski.[1] In general, any material with a crystal structure of formula ABX_3 is referred to as a three-dimensional perovskite. These materials usually have a crystal structure of cubic or tetragonal. Here, A and B are cations, and X is an anion. Based on the crystal structure, perovskites can be future categorized into two-dimensional and quasi-two-dimensional structure.[2]

Traditional perovskite materials only consist of inorganic compounds, but the new class of perovskite materials with hybrid organic and inorganic cations with halide-based anions are also available. Organic-inorganic hybrid perovskite (OIHP) materials have received considerable attention in the field of photovoltaics due to their excellent solar power conversion efficiencies (PCE) $> 25\%$ on a research scale that is comparable to commercially available solar cells.[3] In addition, hybrid perovskites have been actively studied in various semiconductor devices such as light-emitting diodes,[4][5] photodetectors,[6][7] lasers,[8][9] and field-effect transistors.[10][11][12][13]

In hybrid perovskites, for the inorganic cations, metals such as (Pb^{2+} or Sn^{2+}) and for halides (Cl^- , Br^- or I^-) are used. The size of organic cation used in 3D perovskites is limited by the Goldschmidt tolerance factor, which is a guideline for the stability of the perovskite structure.[14] However, a wide range of organic cations can be incorporated into cages of quasi-2D perovskites since the requirement for tolerance factor is relaxed.[15]

There has been a rapid development of lead-based perovskites for applications in optoelectronics. However, due to the toxicity of lead, alternatives such as lead-free perovskites are currently being actively explored. Among these candidates, tin-based materials are considered as one of the promising alternatives. However, the challenges related to device performance and environmental stability must be overcome before commercialization.[16][17] Hybrid perovskite thin-film transistors are another potential application of organic-inorganic perovskite, which usually have superior carrier mobility than organic transistors and can be easily fabricated with lower cost, low-temperature solution-processing methods such as spin coating, dip coating, and

screen printing.[18][19] It can also be fabricated on a flexible substrate.[20]

1.2 Hybrid organic-inorganic perovskite

As it was mentioned in previous section, perovskites belong to a large group of materials that has the crystal structure of ABX_3 . However, hybrid organic-metal halide perovskite is popular due to its outstanding optoelectronic properties. Figure 1.1 describes a complete set of materials that come under the name of perovskite. It can be categorized into two main subgroups such as inorganic oxide perovskites and halide perovskites. The initial studies about oxide perovskites are dated back to 1839.[21] It is considered as an important functional material which is explored in ferroelectric, dielectric, piezoelectric, energy conversion and storage applications.[22]. The inorganic oxide perovskites are future categorized into intrinsic and doped perovskites. The other main subfamily under perovskites is halide perovskites. This is future categorized into alkali-halide and organo-metal halide perovskite. The main application for the halide perovskites is in optoelectronics fields. Both hybrid organic-inorganic halide perovskite and alkali halide perovskites are actively explored in semiconductor-based devices like photovoltaics and light emitting diodes.[23] This research mainly focuses on organo-metal halide perovskites and, more specifically, 2D hybrid tin-iodide perovskites with different alkyl ammonium-based cations, which will be discussed in detail in next sections.

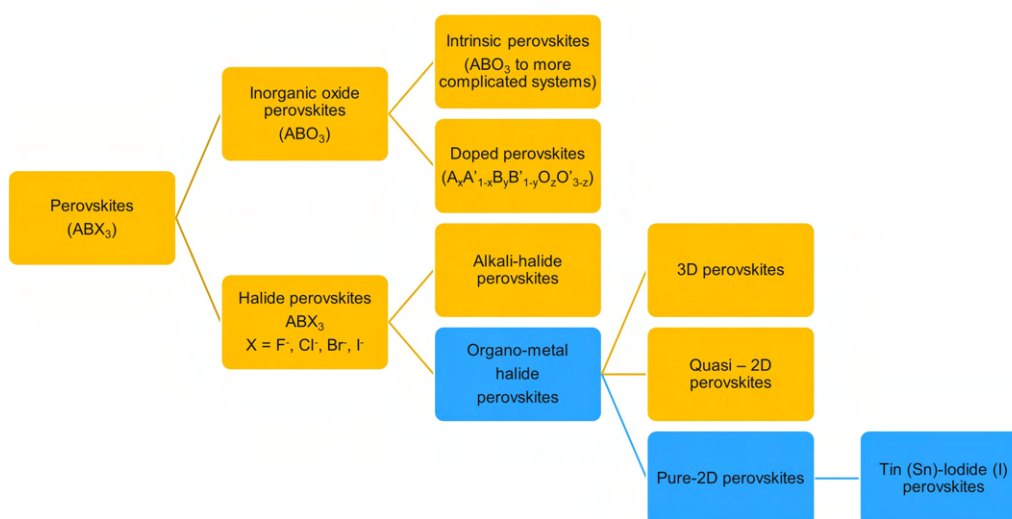


Figure 1.1: Classification of perovskite material.[24]

1.2.1 Three dimensional perovskites

3D hybrid perovskites under the family of organo-metal halides are known for their outstanding device performance, such as high power conversion efficiencies and charge carrier transport but lack of stability over environmental conditions is one of the main drawbacks.[25] Hybrid perovskite consists of crystal structure ABX_3 , here A usually refers to a small organic cation such as methylammonium ($CH_3NH_3^+$),

and formamidinium ($\text{CH}_3(\text{NH}_2)_2^+$), B is generally a divalent metal such as Pb^{2+} , Sn^{2+} , Ge^{2+} , Cu^{2+} , Mn^{2+} , Cd^{2+} , Cr^{2+} , and Zn^{2+} . X is an anion which is typically a halide such as I^- , Br^- , and Cl^- . In the presented configuration, cation B is octahedrally coordinated with anion X and forms a 3D corner-sharing $[\text{BX}_6]^{4-}$ octahedra. The cation A is embedded in the space formed between adjacent $[\text{BX}_6]^{4-}$ structures.

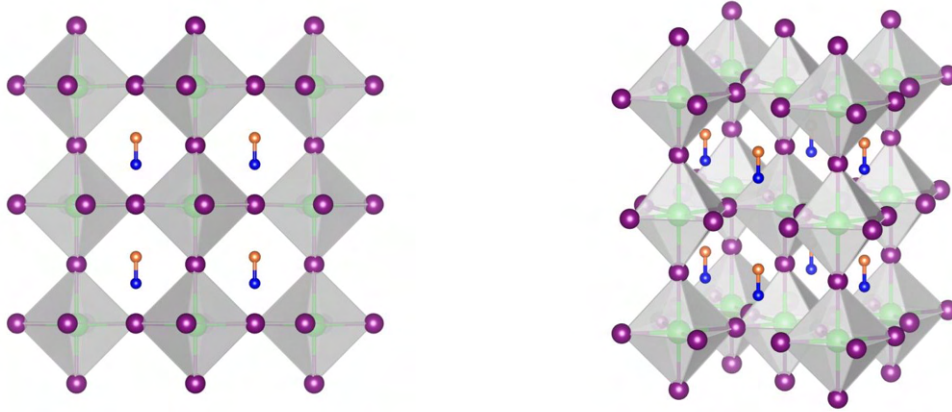


Figure 1.2: Crystal structure of 3D hybrid perovskite with the chemical formula of $\text{CH}_3\text{NH}_3\text{SnI}_3$, where methylammonium (CH_3NH_3^+) cations embedded in the space of corner-sharing $[\text{SnI}_6]^{4-}$ framework.

Tolerance factor

Evaluating and predicting the stability of crystal structure of 3D hybrid perovskites is essential for their application. This can be facilitated by various procedure. The geometrical tolerance factor (α) is one of the widely used tools to evaluate the stability of perovskites, which was introduced by Goldschmidt in 1926 is given by:

$$\alpha = (r_A + r_X) / \sqrt{2}(r_B + r_X) \quad (1.1)$$

where r_A , r_B , r_X are radii of ions in 3D perovskite ABX_3 . This parameter explains ionic size mismatches that perovskite can tolerate without forming different structure types.[14] Usually α between 0.9 and 1.0 gives cubic perovskites crystal structure. Distorted perovskites are found between 0.80 and 0.89. Below 0.8 other structures such as ilmenites (FeTiO_3) are determined. The α above 1.0 leads to hexagonal structures with face sharing octahedra.[26]

The main advantage of this tolerance factor in 3D hybrid perovskite is to understand the size of organic cations that can be introduced to gaps in the 3D inorganic framework. This is severely restricted to smaller organic cations such as methylammonium (CH_3NH_3^+ , MA) and formamidinium ($\text{CH}(\text{NH}_2)_2^+$, FA). This restriction in 3D perovskites motivates us to explore more flexible lower-dimensional perovskites where large cations can be introduced without any restriction.

1.2.2 Lower dimensional perovskites

Lower dimensional (LD) perovskites are developed to have higher environmental stability. In addition, LD perovskites can have more versatile structures than 3D perovskites, and this enables optimizing the optoelectronic properties through changing the structural compositions.[27] LD perovskites can be classified into three categories based on different crystallographic slicing along 3D perovskites such as (100), (110), and (111) oriented structures, according to Miller indices (Figure 1.3).

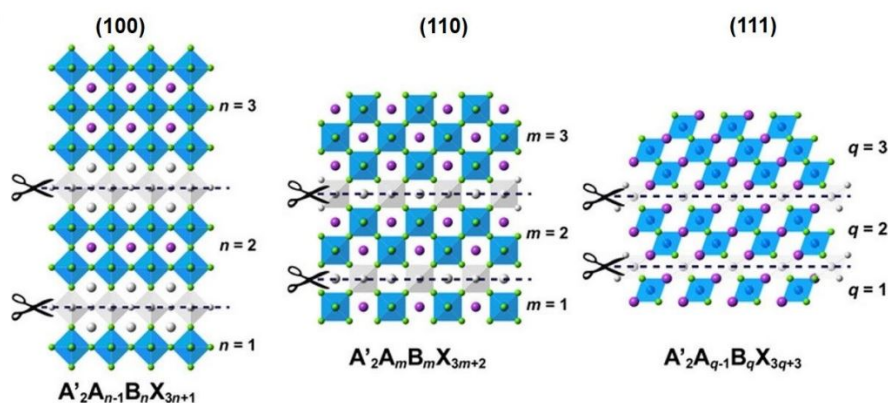


Figure 1.3: Three different types of LD hybrid perovskites based on crystallographic slicing of 3D perovskite through different crystal planes such as (100), (110), and (111).[28]

Among these, the most common (100) structures (layered structure) can be future categorized into different phases (Figure 1.4) based on interlayer spacer cations such as Ruddlesden–Popper (RP),[29] Dion–Jacobson (DJ),[30] Aurivillius,[31] and the alternating cation (ACI)[32] phases.

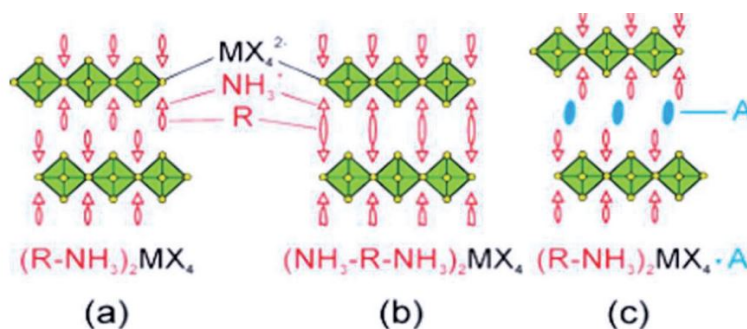


Figure 1.4: The most popular (100) type LD perovskites, these can be future categorized into (a) RP, (b) DJ and (c) ACI phases based on type of organic spacer cation. Where RP phase contain single monoammonium cation as organic spacer, DJ phase consist of diammonium cation as organic spacer and ACI phase is a mixture of monoammonium and diammonium cations.[33]

Ruddlesden–Popper perovskite

LD hybrid perovskites with RP phase are first reported back in around 33 years, where pure 2D layered structure made of lead iodide inorganic framework with

alkyl ammonium spacers $(C_{10}H_{21}NH_3)_2PbI_4$ were used.[34] This new type of LD hybrid perovskite was subsequently demonstrated with tin-iodide-based semiconductor devices.[35][18] The RP phase is considered as the most popular among DJ and ACI counterparts in perovskite solar cells because of its proven record of long-term stability.[29][36] Lower dimensional RP phase perovskites are layered system with general formula of $R_2A_{n-1}B_nX_{3n+1}$. [37][38] Pure 2D RP phase perovskites have a mono layered system with molecular structure R_2BX_4 , Here R is usually an extended non-conjugated organic cation $R-NH_3^+$ (see example in Figure 1.5).

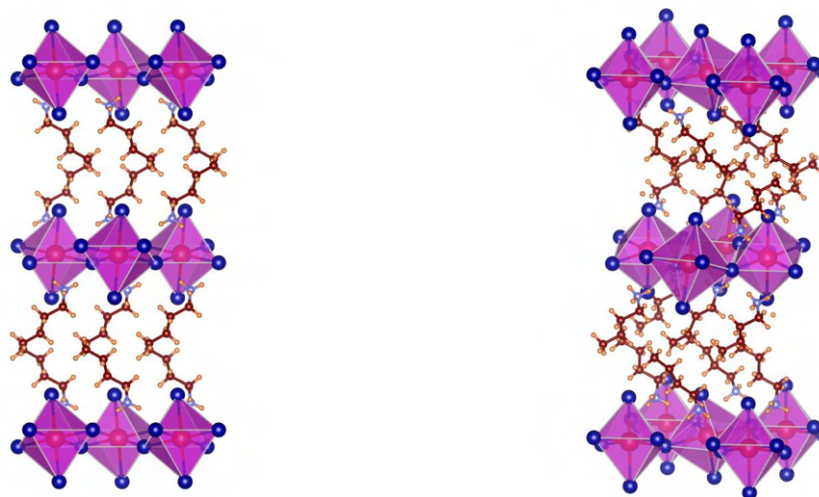


Figure 1.5: Crystal structure of 2D RP perovskite with chemical formula $[CH_3(CH_2)_3NH_3]_2SnI_4$. The butylammonium cations act as spacers between the layered inorganic framework.

Dion-Jacobson (DJ) phase perovskite

2D hybrid perovskite with Dion-Jacobson phase is considered as a promising alternative to RP phase perovskite since a single diammonium organic cation as interlayer eliminates the weak Van der Waals interaction between the mono ammonium organic cations. Also, the strong hydrogen interaction between organic spacers and inorganic layers at both ends of diammonium molecule attributes to high efficiency and outstanding stability in perovskite-based solar cells than those based on RP phase.[39] In contrast to the much mature RP phase, DJ phase 2D hybrid perovskite was first reported in 2018 by Kanatzidis et al., where lead iodide-based perovskite material with organic cations such as (aminomethyl)piperidinium (3AMP) or 4-(aminomethyl)piperidinium (4AMP) have been used as the interlayer.[30] The low dimensional lead-free DJ phase tin halide perovskites for photovoltaics was first reported in 2018. However, the power conversion efficiency (PCE) is just around 1%, which is much lower than the currently reported perovskite-based solar cell efficiency of 25.2 %.[3] However, the overall efficiency of DJ phase perovskite solar cells is improved dramatically over a short period of time, and a reported efficiency of around 16 % was achieved by a simple spin-coating method with additive engineering.[40] Also, around 18% efficiency was reported for DJ perovskite solar cells with optimized interface for perovskite and hole transport layer.[41]

Generic formula of DJ phase perovskite is $RA_{n-1}B_nX_{3n+1}$ (Figure 1.6), where R is a non conjugated organic cation $NH_3^+ - R - NH_3^+$.

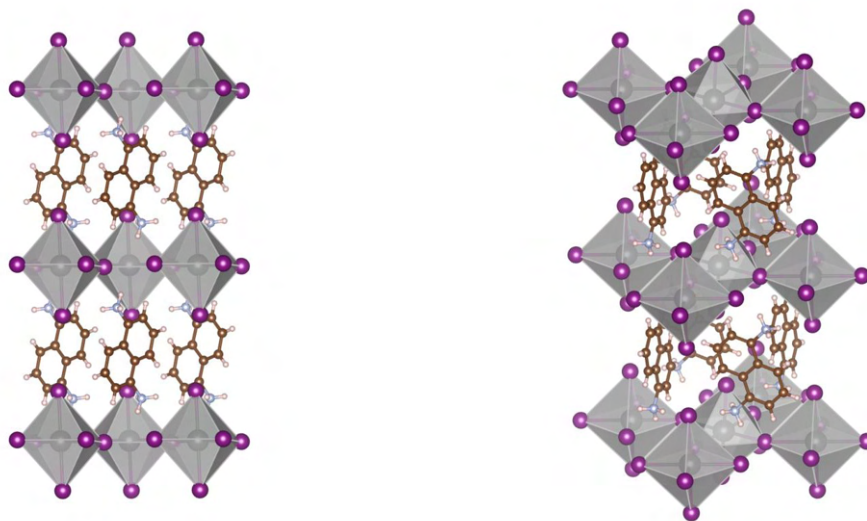


Figure 1.6: Crystal structure of 2D perovskite with DJ phase, which consists of chemical formula $[NH_3C_{10}H_6NH_3]PbI_4$, where Naphthalene-1,5-diammonium ($[NH_3C_{10}H_6NH_3]^{2+}$) cations are spaced between inorganic layers, In contrast to RP phase, Van der Waals gap between the spacer cations has been eliminated due to single diammonium organic cation which connects between inorganic layers.

Alternating cation interlayer (ACI) phase perovskite

The alternating cation interlayer phase is considered as another type of layered lower-dimensional perovskite. This unique phase of perovskite blends the chemical formula of RP perovskite with features of DJ perovskites (Figure 1.7). This leads to a shift of a $(1/2, 0)$ layer reminiscent of the DJ perovskites. Also, the charge balance restrictions that change the occupation of the interlayer sides lead to different centering of the unit cell.[32] Initial research in ACI perovskite solar cells shows higher power conversion efficiency and better environmental stability than lower-dimensional RP and DJ perovskites.[42][43]

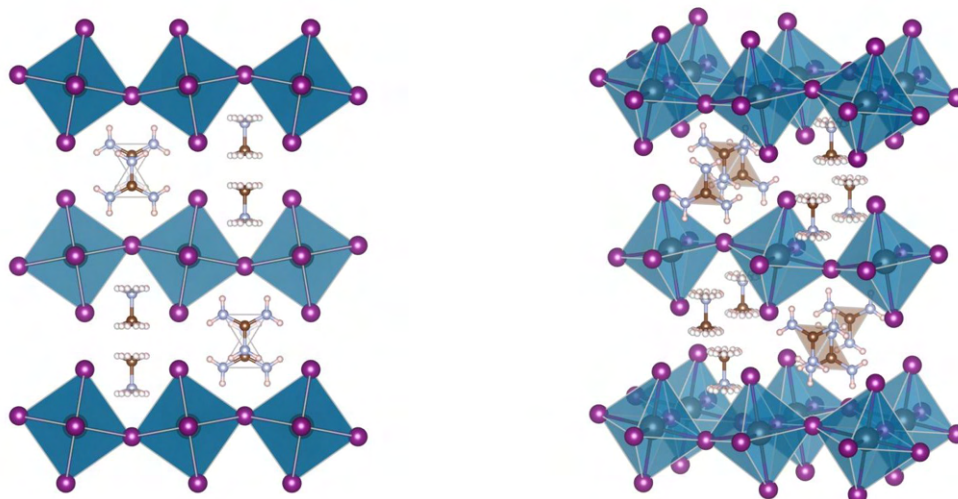


Figure 1.7: The crystal structure of 2D perovskite with ACI phase, which has a chemical formula of $[\text{C}(\text{NH}_2)_3][\text{CH}_3\text{NH}_3]\text{PbI}_4$, where mixed methylammonium (CH_3NH_3^+) and Guanidinium ($[\text{C}(\text{NH}_2)_3]^+$) cations are organized between the layers of inorganic cations.

1.3 Factors affecting the stability of hybrid perovskite

The hybrid perovskites have excellent charge carrier transport properties with higher efficiency in respect to the organic materials, but stability is the main challenge in perovskite-based semiconductor devices, especially when it is exposed to moisture, light, mechanical stress, and reverse bias contributes to degradation. Only a few methods are currently being studied, such as tuning the composition of perovskites, hydrophobic coatings, replacing the metal electrodes, and packaging techniques to improve environmental stability of perovskites.[44]

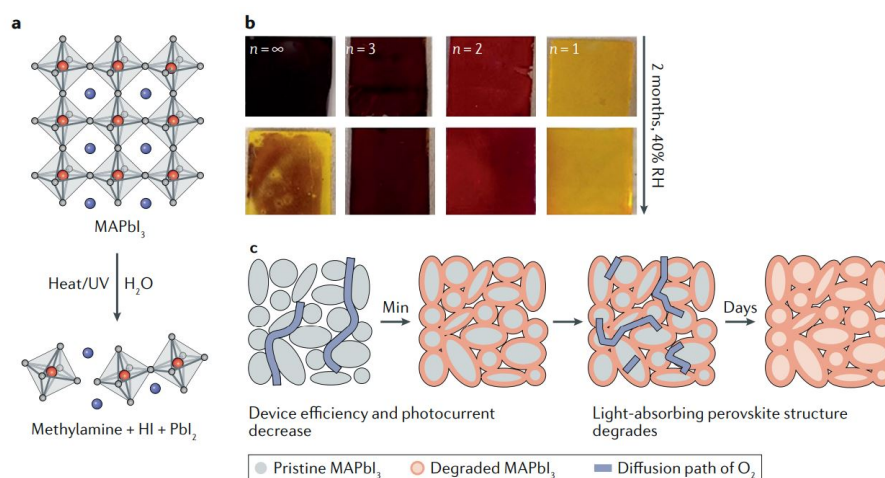


Figure 1.8: The perovskite material decomposes into a precursor or 0D hydrate phase when exposed to heat, moisture, or UV light. The degradation of perovskite material causes a reduction in device efficiency and light absorption properties.[27]

1.3.1 Moisture

Based on several studies, moisture contributes to reversible and irreversible degradation. The water molecules can easily penetrate into perovskite structures and produce an intermediate form of the monohydrate and dehydrate perovskites. However, this can be reversible back to its original form when it is exposed to dry air for more than 48 h.[45] The water molecules in perovskite form strong hydrogen bonds with the organic cations and weaken the bonds of PbI_6 in $\text{CH}_3\text{NH}_3\text{PbI}_3$ perovskites and allow faster deprotonation of organic cations. Water also protonates iodide, and as a result, it produces hydroiodic acid (HI), and finally, yellow-colored lead iodide remains as a decomposed product.[46][47]

3D in situ ToF-SIMS imaging of $\text{CH}_3\text{NH}_3\text{PbI}_3$ perovskites revealed irreversible vaporization of CH_3NH_2 from the perovskite when it exposed to humidity. Instead of H_2O deuterium oxide (D_2O) is used to humidify the chamber. The products which formed from the deuterium exchange reaction are $\text{CH}_3\text{NH}_2\text{D}$, CH_3NHD_2 , and CH_3ND_3 . After these initial reactions, D_2O eventually replaces the methylammonium cation in the perovskite, and this leads to the evaporation of CH_3NH_2 molecules and subsequent erosion of perovskite crystal structure and degradation of optoelectric properties.[48]

Perovskite solar cells were also observed to degrade within a few hours when exposed to air with a relative humidity of more than 50%. [49][46] The relative humidity is considered an important parameter that triggers the degradation process. It is shown that hybrid perovskite formamidinium lead iodide (FAPbI_3) that is exposed to below 30% of humidity demonstrates excellent phase stability over 90 days, but once it reaches 50% of humidity, formamidinium lead iodide degrades rapidly. The results of Kelvin probe microscopy reveal that the formation of non-perovskite phases begins at the grain boundary and propagates towards grain interiors. Also, ion migration near the grain boundaries is significantly enhanced after the degradation.[50] Another study also revealed that trapped charges in the grain boundaries are an essential parameter to enable moisture-induced degradation. This is verified experimentally by depositing charges of different polarities on the perovskite films in a humidity-controlled environment. The Kelvin probe force microscopy (KPFM) studies explained that charges are preferentially trapped along grain boundaries even with uniform charge deposition and illumination.[51]

1.3.2 Oxidation

Once perovskite material is exposed to the air, the oxygen molecules would diffuse through the halide vacancies on the surface and penetrate the bulk lattice within an hour. Metal halide-based perovskites are relatively stable in the dark. However, it will rapidly decompose in the presence of light and oxygen since, under light illumination, a high number of iodide vacancies would be generated, and a similar number of oxygen molecules would diffuse into a bulk perovskite crystal. These absorbed oxygen molecules would form superoxide (O_2^-) by electron transfer from the photoexcited perovskite phase, and the superoxide breaks the bonds of perovskites by deprotonating A-site organic cation (CH_3NH_3^+) and generates products of water, iodine, A-site organic cation gas (CH_3NH_2) and lead iodide (PbI_2). [52]

Tin-iodide perovskites are more susceptible to oxidization than lead-iodide perovskites. The tin cations, normally in the form of Sn^{2+} in perovskites, will be oxidized into Sn^{4+} . This degrades the performance of the device and erodes the perovskite crystal structure.[53]

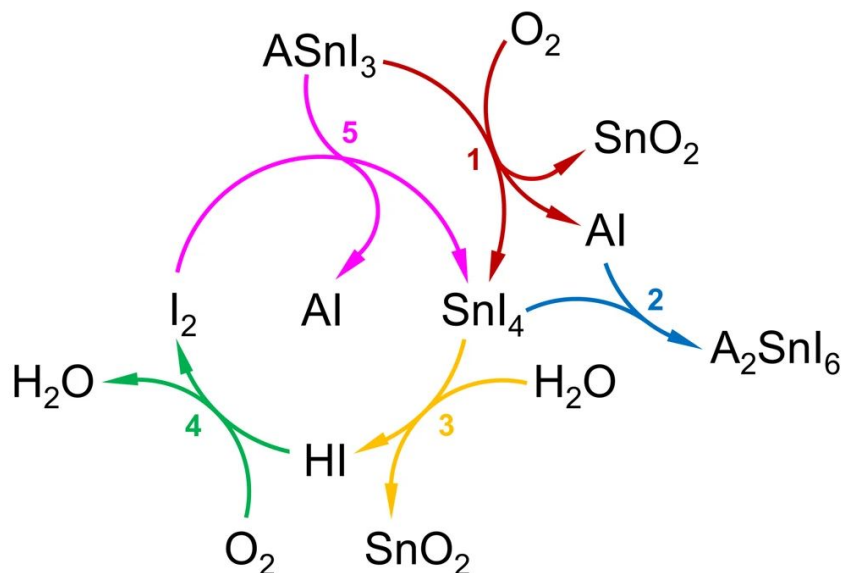


Figure 1.9: Degradation mechanism in hybrid tin-iodide perovskite when exposed to ambient air.[54]

The Figure 1.9 explains the degradation pathways in 3D tin iodide hybrid perovskite ASnI_3 (where "A" is organic cation such as formamidinium (FA) or methylammonium (MA)). Oxygen and moisture in the ambient air contribute to the erosion of perovskite. A cyclic chain of reactions explains the complete degradation process. (1) Formation of SnI_4 by a reaction between perovskite and O_2 . (2) Formation of the solid-state A_2SnI_6 from the reaction by-products Al and SnI_4 . (3) Hydrolysis of SnI_4 by H_2O and formation of HI and SnO_2 . (4) Oxidation of HI by O_2 and formation of I_2 and H_2O (5) Oxidation of perovskite by I_2 and formation of SnI_4 . [54]

1.3.3 Light illumination

Perovskite-based materials have an outstanding photoelectric properties, but light illumination also influence perovskite material. In 3D perovskite material such as MAPbI_3 , the holes generated under light illumination would protonate halide anions (iodide) and form neutral atoms (iodine) and halide vacancies. Neutral iodine is smaller in size than iodide, and it would fit into interstitial sites of the lattice. During illumination, a significant amount of iodine anions become interstitial atoms. This effect is reversible, but the exposure to light illumination also changes the thermodynamic properties of the material. This also increases the effective chemical potential of neutral iodide during illumination and causes iodine to leave the lattice permanently. This leads to permanent degradation of perovskite material and forms products of metallic lead and halogen gas.[55] This degradation is partially reversible according to X-ray photoemission spectroscopy (XPS) analysis in several studies, but

an overall deterioration in device performance has been observed, making it more susceptible to moisture.

1.3.4 Ion migration

Another critical issue in hybrid perovskites is ion migration, which contributes to many unusual phenomena observed, such as current-voltage hysteresis, higher dielectric constant, poor transistor characteristics at room temperature, switchable photovoltaic effect, photo-induced phase separation, and photo-induced self-poling doping effect in perovskites.[56] Also, it is important to understand the types of ions that are migrating in hybrid perovskites, based on the experimental and theoretical analysis of halide ions (X^-) in the inorganic octahedra are known to migrate nearest halide vacancies. This is similar to well-studied oxide-based perovskites (ABO_3), where O^{2-} were the migrating species.[57] In addition, small organic molecules such as methylammonium are also known to migrate in lead iodide hybrid perovskites at elevated temperatures around 330 K.[58]

The possibility of an ion migrating inside the solid is influenced by activation energy. The migration rate (r_m) depends on activation energy (E_A), Boltzmann constant (k_B) and temperature (T).

$$r_m \propto \exp\left(-\frac{E_A}{k_B T}\right) \quad (1.2)$$

Based on the first principle calculation on activation energy in methylammonium lead iodide perovskites, iodine vacancies and interstitials may easily migrate due to lower activation energy in the range of 0.1 eV with less than 1 μs migration time. When it comes to methylammonium and lead ions, they show energy barriers of around 0.5 and 0.8 eV, with calculated times in the range of 10 ms to minutes.[59]

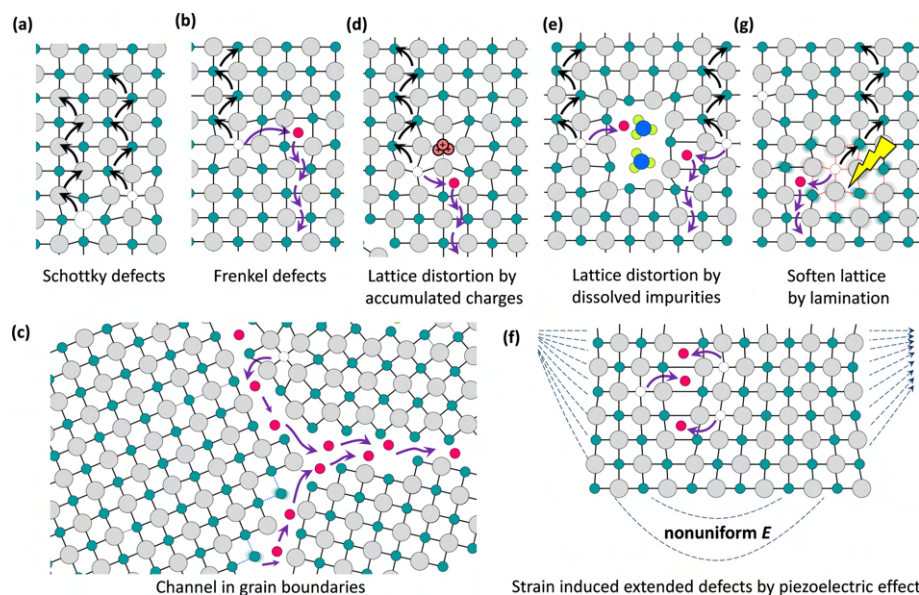


Figure 1.10: (a,b) Schottky and Frenkel defects, (c) channel in grain boundaries, (e) lattice dislocations, (g) softening of the lattice by lamination, and (f) strain-induced extended defects by piezoelectric effect are ion migration pathways in hybrid perovskites.[56]

The Schottky and Frenkel defects are the two main types of point defects that usually exist in the perovskite crystal lattice. The Schottky defects such as PbI_2 and $\text{CH}_3\text{NH}_3\text{I}$ and Frenkel elemental defects such as Pb, I, and CH_3NH_3 vacancies are the main types of point defects in methylammonium lead iodide ($\text{CH}_3\text{NH}_3\text{PbI}_3$) perovskite enables ion migration.[60] In addition to point defects in crystals, ion migration in perovskites is mainly dominated by grain boundaries in polycrystalline film. The grain boundaries facilitate channels for ion migration in hybrid perovskites. The atomic force microscopy measurements provided strong hysteresis for both photocurrent and dark-current at the grain boundaries. This enhancement in ion migration redistributes ions through the channel of grain boundaries after poling in contrast to the intact grain area. Also, single-crystal perovskite devices show negligible hysteresis.[61] The polymer grain passivation methods are known to drastically reduce the hysteresis by suppressing ion migration.[62]. Apart from grain boundaries, other types of defects such as lattice distortion by accumulated charges, strain induced in the crystal structure due to piezoelectric effects, undissolved impurities, and photo-induced softening of lattice also causes ion migration.[56]

Effect of ion migration	Outcome
Hysteresis	Unfavorable
Device degradation	Unfavorable
Phase segregation	Unfavorable
Giant capacitance at low frequency	Unfavorable in PV but favorable for photodetectors
Ionic conduction	Favorable in photodetector and resistance-switching memory devices
Light soaking	Favorable in PV performance but certain time required to stabilize
Interface passivation	Favorable in perovskite photoelectronic devices

Table 1.1: Effects of ion migration in hybrid perovskite are sometimes referred to as a "double-edged sword" because all the consequences of ion migration in semiconductor devices are not detrimental.[63]

Lower dimensional perovskites are believed to suppress ion migration which is severe in 3D perovskites. This is proved by the measurement of ionic conductivity in 3D $\text{CH}_3\text{NH}_3\text{PbI}_3$ and quasi-2D $(\text{BA})_2(\text{MA})_3\text{Pb}_4\text{I}_{13}$ perovskite films under dark and 0.25 sun illumination conditions. In 3D $\text{CH}_3\text{NH}_3\text{PbI}_3$ perovskite, when the temperature reaches 260 K, ion conductivity starts to dominate the conductivity, and the transition temperature for electronic to ion migration dominated conduction reduced from 260 K to 240 K under 0.25 sun illumination condition. However, such transition is not observed in quasi-2D $(\text{BA})_2(\text{MA})_3\text{Pb}_4\text{I}_{13}$ perovskite until it reaches 330 K under both dark and 0.25 sun illumination conditions. It is believed that organic spacers influence suppressed ion migration.[64]

The underlying mechanism for reduced ion migration in layered perovskite is explained by two key factors. The out-of-plane ion migration is reduced by longer chain organic molecules that act as spacers between inorganic layers. However, ion movement in the in-plane direction can not be blocked by organic spacers since these are unable to prevent the in-plane ion migration paths. Suppression of ion migration in layered perovskites along in-plane direction can be explained by an increase in formation energy for vacancies compared to 3D perovskites. The suppressed ion migration indicates better stability under electrical bias, and semiconductor devices made of layered perovskites have reduced ion-diffusion-induced degradation of contact electrodes and charge transport layers.[65]

1.4 Improving stability of hybrid perovskites

Several methods have been explored in the past to improve the stability of hybrid perovskites, such as changing the perovskite composition, encapsulating perovskite material, optimizing the electron/hole transport layer, surface passivation, and crystal structure optimization such as introducing 2D perovskite materials.[66]

The trap states at the grain boundaries in perovskite films are known to deterio-

rate optoelectric properties and stability. The introduction of Lewis acid or base functional group molecules is demonstrated to passivate grain boundaries and improve the device performance as well as long-term environmental stability (in 40 days, degradation of only 13% without encapsulation in a 50% relative humidity environment).[67] In addition, small organic molecules with cyano units as terminal groups are also known to passivate grain boundaries and surface defects, also known to improve environmental stability.[68] There is another interesting method used to manipulate the grain boundaries in polycrystalline films, such as the introduction of macrostructure molecules instead of small-molecule-based additives. This is motivated by the high volatility and diffusivity of small molecules in harsh environments. Introduction of macromolecules with special technique forms polymer-perovskite composite cross-linker, which will bridge the gaps in grain boundaries and provide excellent environmental stability against light, heat, and moisture.[69] There are also reports about self-sealing polymers to improve stability. The poly(ethylene-co-vinyl acetate) (EVA) polymer is introduced into anti-solvent during spin coating of formamidinium tin tri-iodide (FASnI₃), which helps to improve grain size, grain orientation, and surface defects reduction. This provides encapsulation to FASnI₃ and acts as a barrier to moisture and oxygen.[70]

The introduction of a 1D capping layer on top of the perovskite layer is considered an efficient method to passivate perovskite films to improve environmental stability.[71] However, insulated layers from low dimensional organic cations are known to decrease the device efficiency in solar cells, and in-situ cross-linking polymerizable propargylammonium at the surface and grain boundaries is used to form a heterostructure known to reduce the residual tensile strain, which helps to improve the overall device performance and stability.[72] Introduction of heterostructures to improve the stability also reported in other semiconductor devices such as LEDs, where surface 2D and bulk 3D heterophase perovskite approach has been used. This enables significantly reduced trap density, immune to ion migration on the surface, fast radiative recombination, and improved environmental stability.[73]

The ultraviolet photocatalytic effect of metal oxide layers also degrades perovskite-based solar cells. Modification in the electron transfer layer is known to improve long-term environmental stability.[74] In addition to the above-mentioned methods, an overlooked factor such as residual stress in perovskite films also contributes to mechanical and environmental instabilities. Carefully selecting lower-temperature processing methods and polymeric substrates with high thermal expansion coefficients might help to improve the intrinsic stability of the films.[75]

1.5 Advantages of 2D hybrid perovskite

Although 3D perovskites exhibit excellent optical and electrical properties, the commercialization of perovskite-based semiconductor devices is hampered by environmental stability. There is a growing number of research focusing on 2D perovskites to resolve this issue. This is verified by an exponential increase in the number of publications and citations over the past ten years (Figure 1.11). 2D perovskite materials contain large organic cations between inorganic layers. They are known to block degradation pathways such as air and moisture from entering inorganic layers due to the hydrophobic nature of organic spacers.[76]

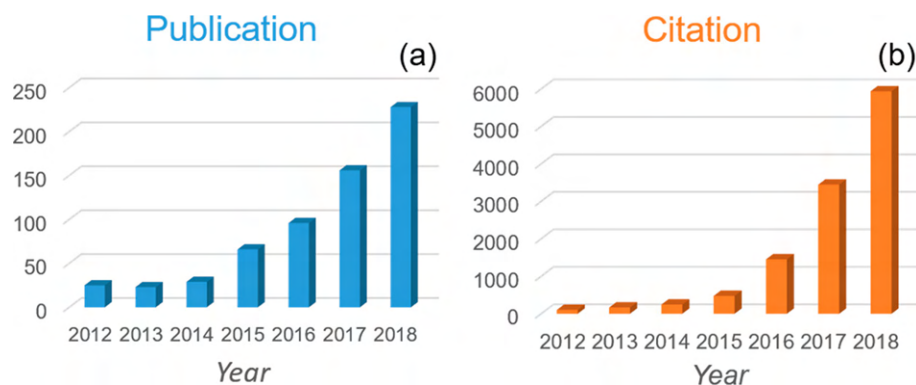


Figure 1.11: Over the past decade, there has been an exponential increase in the number of publications and citations on the topic of “2D halide perovskite materials”. Data collected from the web of science.[77]

Furthermore, the size of the organic cation that can be introduced into 3D perovskites is limited by the Goldschmidt tolerance factor. However, this limitation is relaxed in 2D perovskites. Different molecular size organic spacers can be used to change the interlayer spacing between inorganic layers, which helps to tune intrinsic parameters such as optical band gap, exciton binding energy, and dielectric constant in perovskites.[78]

The geometry of organic cations modulates the electronic properties of 2D perovskites via the strain introduced on inorganic layers, which is governed by the ability to fit between the interstitial space in inorganic octahedra. On the other hand, the image-charge effect between the inorganic high-dielectric constant quantum well layers and the organic low-dielectric constant spacer layers creates dielectric confinement and influences the electronic band gap and exciton binding energy.[77]

Traditionally 3D perovskite devices perform much better than their 2D counterparts due to poor carrier transport, large binding energy, and low conductivity in 2D hybrid perovskites but the introduction of new techniques in perovskite film processing such as vapor-fumigation,[79], self-assembled monolayer,[10] and solvent vapor annealing [80] significantly improved the device performance.

1.6 Organic spacers for 2D hybrid perovskite

There are many organic cations reported as spacers in layered perovskite structures. First, this can be grouped into diammonium and monoammonium cations. In general, monoammonium cations are used in RP phase, and diammonium cations are used in DJ phase (described in section 1.2.2). Based on molecular structure, organic cations future categorized into aromatic, cyclic, and linear molecules. It is demonstrated that variations in the length of alkyl ammonium spacers, the addition of π -conjugated segment, and insertion of ammonium dications are used to enhance electronic coupling between inorganic quantum well layers.[81]

The aromatic molecule phenethylammonium (PEA) is considered the most used organic spacer in 2D perovskites due to its excellent optoelectric properties. There is a large group of similar molecules with small changes in functional groups, that

have been explored in the past to obtain efficient and stable perovskite-based devices. For example, in PEA, substituting by fluorine atom on the para position forms 4-fluorophenethylammonium (F-PEA). This small change reduces the center-to-center distance of phenyl ring in organic spacer and produces well-aligned layers of perovskite. This enhances orbital interactions and charge carrier transport between the adjacent inorganic layers, and also it increases the charge carrier lifetime and reduces trap density.[82] It is observed that larger hydrophobic cations improve stability against moisture but at the same time adversely affect the device performance.[83] In addition, linear alkyl ammonium molecules such as butylammonium and hexylammonium have been explored in 2D perovskite structures used in solar cells and other semiconductor devices.[84][85] However, lead-free tin-iodide perovskites with alkyl ammonium cations as an active layer in field-effect transistors are still not reported.

Here are the consolidated summary of around 22 structures reported in pure 2D tin-iodide based perovskites devices. However, the relation between chemical structure and charge carrier transport is still not understood:

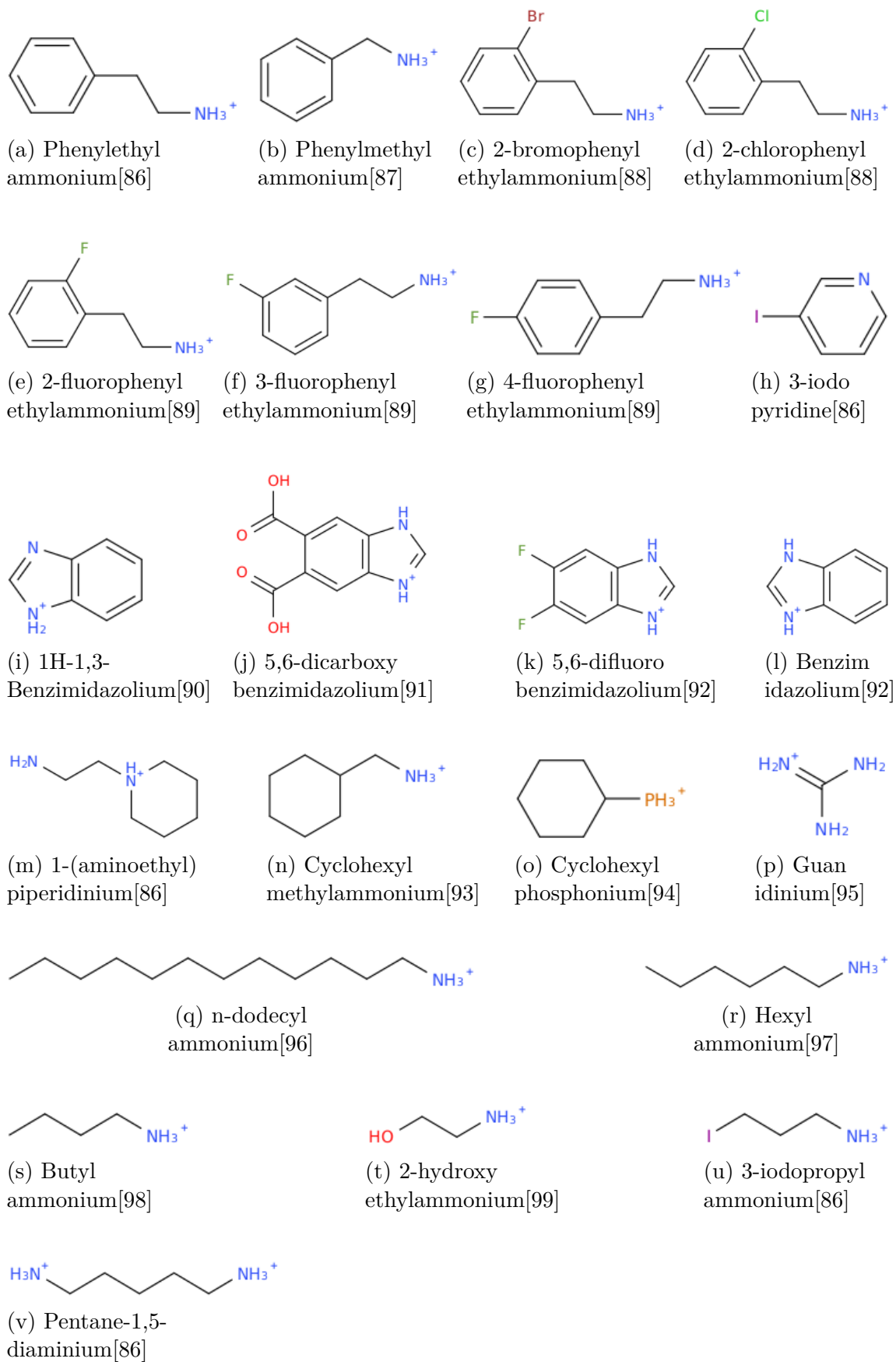


Figure 1.12: The organic cations have been reported in the literature as spacers in 2D tin-iodide hybrid perovskites.

1.7 2D hybrid perovskite field-effect transistor

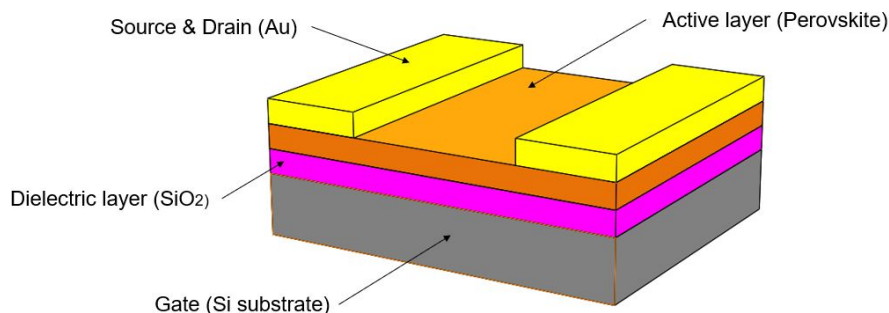


Figure 1.13: The device structure of the 2D perovskite field-effect transistor in this research.

The field-effect transistor is a device used to amplify or switch electrical signals by modulating the conductivity of a semiconductor layer with an electric field.[100] It is considered as a fundamental building block in microelectronics and widely used in computers and electronic devices. FET consists of three terminals such as source (S), drain (D), and gate (G). The source is where charge carriers enter the channel, the drain is where charge carriers leave the channel, and the gate is used to control the flow of charge carriers by applying gate voltage.

Currently, silicon and other inorganic III-V semiconductors are widely used as the active layer and SiO₂ as the dielectric layer in FETs due to their outstanding semiconducting and dielectric properties. However, there are challenges that exist with these semiconducting materials due to the complexity and cost interrelated with fabrication. Organic materials draw attention due to cost-effectiveness, convenience, and manufacturing scalability, but the low charge carrier mobility related to weak Van der Waals interactions in organic molecules limits the performance of organic FETs.

Semiconducting perovskite materials have drawn considerable attention only in the last few decades, even though oxide-based perovskites have been investigated as insulating layers for a long time. Since hybrid perovskites can combine the features of organic and inorganic counterparts on a molecular scale, they can be fabricated with a simple, less expensive, and low-temperature process. In addition, inorganic frameworks in hybrid perovskites interact through strong covalent or ionic bonds, which are responsible for higher charge carrier mobility.[101] Also, similar to organic materials, hybrid perovskites could be fabricated on flexible surfaces. These features make hybrid perovskite a suitable candidate for high-volume manufacturing and large-area flexible devices.[102] Perovskite-based FETs also follow similar architecture to traditional silicon-based transistors, but the main difference is the semiconducting active layer which is specifically made of perovskite. Different types of device structures have been reported in perovskite-based field-effect transistors. The device structures such as Bottom Contact/Bottom Gate (BC/BG), Top Contact/Bottom Gate (TC/BG), Bottom Contact/Top Gate (BC/TG), and Top Contact/Top Gate (TC/TG) are the most commonly used in researches.[10][13][11]

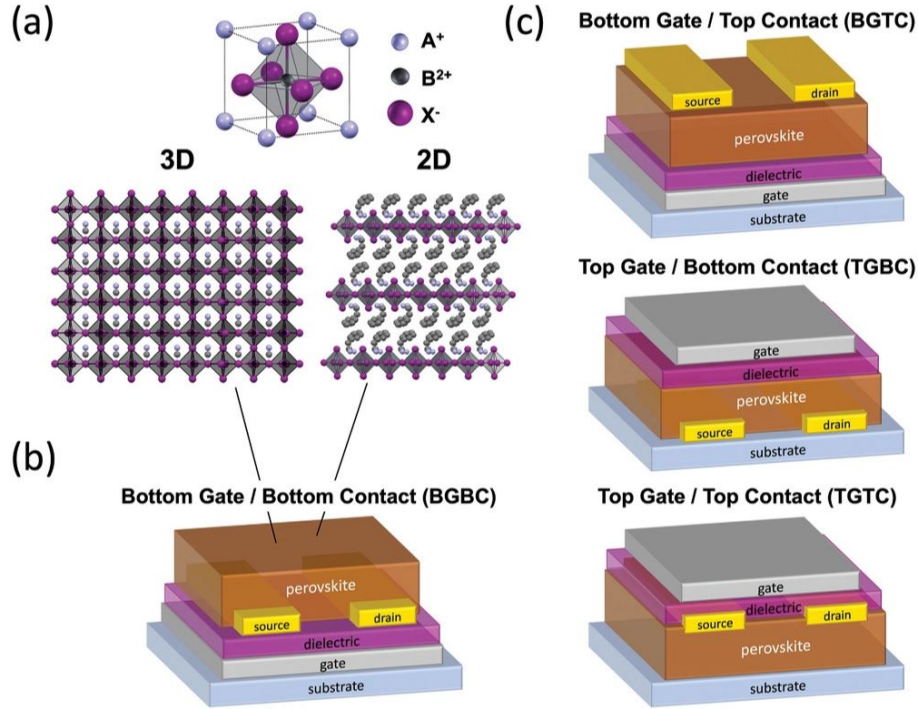


Figure 1.14: Illustration of the reported device structures in the hybrid perovskite field-effect transistor.[103]

The first perovskite field-effect transistor reported back in 1999 followed a pure 2D layered structure phenylethylammonium tin iodide ($(PEA)_2SnI_4$), which showed the behavior of a p-type transistor with charge carrier mobility of $\mu \approx 0.6 \text{ cm}^2V^{-1}s^{-1}$ and current modulation over 10^4 . [18] Back in 2016, $(PEA)_2SnI_4$ perovskite devices show an excellent charge carrier mobility of $15 \text{ cm}^2V^{-1}s^{-1}$ due to enhanced crystallinity, improved hole injection by introducing MoO_x hole injection layers and lower hole trap density near the perovskite-gate dielectric interface. The well-oriented perovskite crystals and reduced hysteresis are achieved with a self-assembled monolayer of NH_3I treatment on the substrate. [10] The same group was demonstrated record-high carrier mobilities of $40 \text{ cm}^2V^{-1}s^{-1}$ or higher in $(PEA)_2SnI_4$ layered perovskite. Instead of spin-coated polycrystalline thin film, which usually has a large amount of grain boundaries and structural disorder, they have prepared large single crystals of perovskite, but this method has a low fabrication yield of ($\leq 1\%$). [104]

In contrast to 2D perovskites, field-effect behavior in 3D perovskites has only been explored since 2013. [105] The initial 3D $(MA)PbI_3$ perovskite field-effect transistors suffered from serious ion migration at room temperature, and field-effect current modulation was only observed at low-temperature measurements. [106] However, with the optimization of thin-film microstructure and modification of source and drain contacts, the instability and hysteresis in $(MA)PbI_3$ perovskite are reduced significantly and showed an electron field-effect mobility of $0.5 \text{ cm}^2V^{-1}s^{-1}$ at room temperature in 2017. [107] The method of solvent vapor annealing is used to future improve carrier mobility via microstructure control, which exhibited hole and electron mobilities over $10 \text{ cm}^2V^{-1}s^{-1}$ in 2018. Recently hysteresis-free high-performance transistors with hole mobilities of $20 \text{ cm}^2V^{-1}s^{-1}$ and a current on/off ratio exceeding 10^7 realized through anion engineering. [108]

2D hybrid perovskite transistors have a unique advantage over 3D counterparts due to intrinsically suppressed ion migration results from layered structures.[109] Several techniques related to organic spacer tuning, additive engineering, and microstructure optimization have been explored to improve the electrical properties and stability of the devices.[110][111][112]

Chapter 2

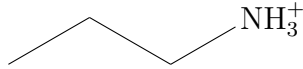
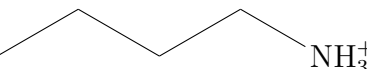
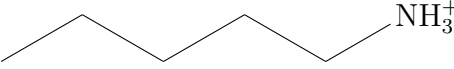
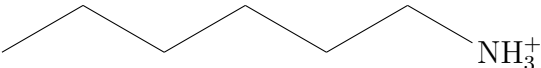
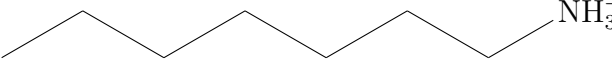
Experiments

2.1 The device preparations

2.1.1 The synthesis of 2D perovskite

Alkyl ammonium spacers

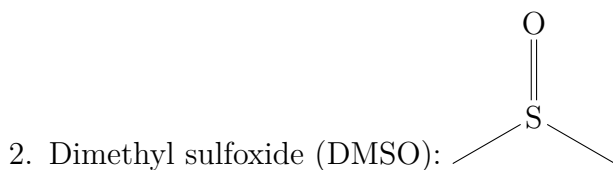
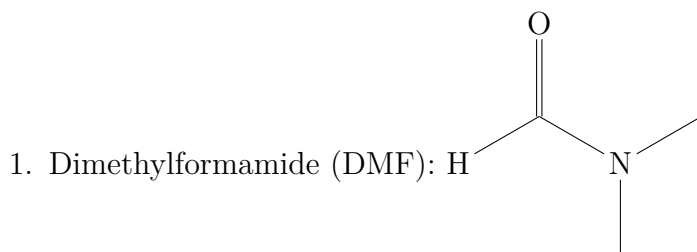
2D hybrid alkyl ammonium-based perovskites have been studied since the 1980s for structural phase transition behavior, ferromagnetism, and excitonic properties.[113][34] However, these organic spacers have received considerable attention due to their application in 2D-3D hybrid perovskite solar cells in the past decade, where it is used as organic spacers to reduce environmental degradation. These alkyl ammonium cations are the simplest molecular structures reported as organic spacers in hybrid perovskite-based devices.[84][114] Here we study a series of monoammonium cations with a gradual increase in the number of carbon atoms in the alkyl chain that could be used as spacers in RP-phase perovskite. The number of carbon atoms in the linear alkyl chain increases from 3 to 7.

1. Propylammonium (PA): 
2. Butylammonium (BA): 
3. Pentylammonium (PentA): 
4. Hexylammonium (HxA): 
5. Heptanammonium (HeptA): 

Solvents

The most popular solvents used in perovskites are dimethylformamide (DMF) and dimethyl sulfoxide (DMSO). DMF is a colorless polar aprotic solvent with a boiling point of $153\text{ }^{\circ}\text{C}$ and a melting point of $-60.4\text{ }^{\circ}\text{C}$. It is miscible with water and most of the organic solvents.[115] DMSO is a colorless polar aprotic solvent that has a boiling point of $189\text{ }^{\circ}\text{C}$ and a melting point of $18.5\text{ }^{\circ}\text{C}$. It is also miscible with water and most of the organic solvents.[116] Pure dimethylformamide (DMF), and a mixture of DMF and dimethyl sulfoxide (DMSO) in a 1:1 ratio have been used as the solvent for the synthesis of 2D perovskite solutions in this research.

DMF as a primary solvent and DMSO as a secondary solvent are used to control the grain sizes in the perovskite films. The grain size in the deposited film increases when the volume ratio of DMSO increases in the precursor solution.[117] DMF and DMSO favor step-by-step reaction from low to high I-iodoplumbate. DMF favors the formation of low-coordination complexes, but DMSO reduces the reaction of high-coordinated complexes. Therefore, reaction energies can be better balanced when using DMSO as an additive in DMF instead of using pure DMF.[118] This is also applicable in 2D perovskites where fast volatilization in DMF solvent creates homogeneous nuclei in perovskites that causes random orientation of crystals in perovskite films. That can be slowed by using the binary solvent mixture of DMF and DMSO as there is the formation of intermediate products.[119]



Tin iodide (SnI_2) (at purity of $\geq 99.99\%$) and solvents DMF and DMSO (at purity $\geq 99.9\%$) were purchased from Sigma-Aldrich, and organic cations (PA, BA, PentA, HxA, and HeptA) with $\geq 99.99\%$ purity were purchased from Greatcell Solar.

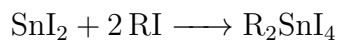
Three types of recipes have been used in the synthesis of 2D perovskites:

1. Precursor at 0.1 M concentration in pure DMF (Recipe A).
2. Precursor at 0.2 M concentration in pure DMF (Recipe B).
3. Precursor at 0.2 M concentration in DMF:DMSO (1:1) (Recipe C).

Firstly, tin iodide (SnI_2) is mixed with monoammonium iodide (RI) in a molar ratio of 1:2 in a glove box environment ($\text{H}_2\text{O} < 0.1\text{ ppm}$, $\text{O}_2 < 0.1\text{ ppm}$) at room temperature. Secondly, 500 μl of solvent is added to the recipe and the solution is

stirred at $60\text{ }^{\circ}\text{C}$ for about 3 hours. Finally, the solution is filtered with a $0.2\text{ }\mu\text{m}$ PTFE filter to remove any undissolved and agglomerated particles.

Chemical reaction



2.1.2 Device fabrication

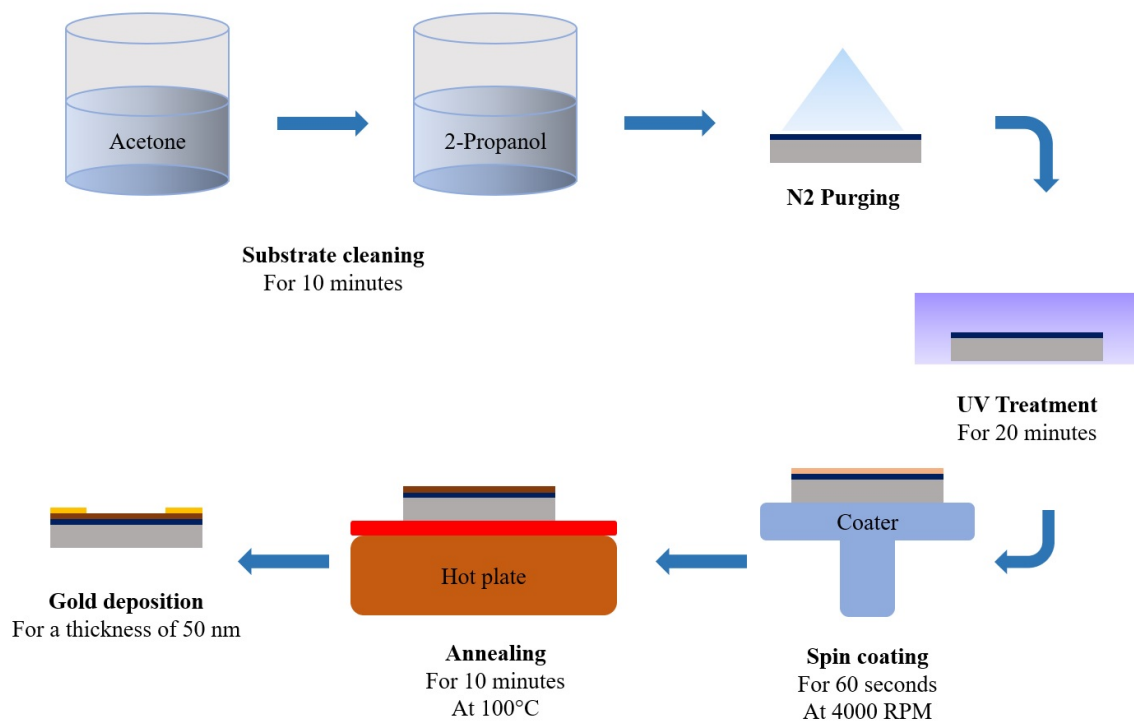


Figure 2.1: Overall process flow of device preparation.

Substrate cleaning

A silicon substrate ($1.5 \times 2\text{ cm}$) with an oxide layer of about 300 nm is used. At first, the substrate is thoroughly cleaned in an ultrasonic bath for 10 minutes with acetone followed by isopropanol. As a next step, it is dried with pure nitrogen gas for a few seconds. Finally, the substrates are treated with ultraviolet rays for about 20 minutes to remove all the residues.

Spin coating

The prepared substrates are then spin-coated in the glove box environment at 4000 rpm for 60 seconds. About $30\text{ }\mu\text{l}$ of precursor solution is used to coat a single substrate.

Annealing

The substrate is then annealed at $100\text{ }^{\circ}\text{C}$ for about 10 minutes to remove the solvent from the wet spin-coated film. The temperature is maintained at $100\text{ }^{\circ}\text{C}$ as it is the optimum temperature for the formation of a highly crystalline film.

Gold deposition

The source-drain electrode patterns are deposited on top of the perovskite layer with a thickness of 50 nm by gold thermal evaporation through a shadow mask. This used to construct transistor channels of $L \times 1000 \mu\text{m}$ (length \times width), where channel length is 10, 30, 50, and 80 μm . Gold is used as the electrode material to avoid contact problems. Since approximately eight devices can be fabricated in a substrate, each device must be first isolated by scribing the perovskite layer around each device. Thereafter, silver paste is used to make connections to the grounded silicon layer. Now, all the steps of device preparation are completed, and the device is finally made ready for measurement.

2.2 Characterization of 2D perovskite

2.2.1 Introduction

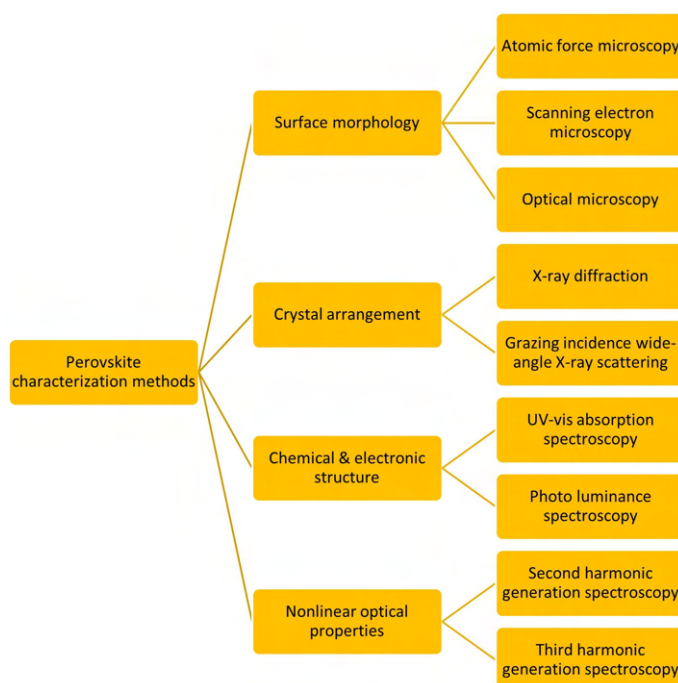


Figure 2.2: Commonly used characterization methods for perovskites.

Understanding the properties of perovskite material is essential to analyzing optoelectronic, structural and electrical transport properties. There are multiple techniques used in this research, where XRD and GIWAXS are helpful in understanding crystal arrangement and preferential growth orientation. The latter qualitatively describes the degree of order in the film. AFM and optical measurement are used to analyze surface morphology. On the other hand, absorption spectroscopy is used to characterize the energy band structure and optical properties of the material. This will provide a basis for understanding the properties of perovskite, and later this will be used to establish a correlation between the size of alkyl ammonium spacer and the charge transport properties with the help of the device measurement.

2.2.2 X-ray diffraction

X-ray diffraction is one of the well-known techniques used in materials science to analyze crystal structures. This non-destructive method has several advantages, such as easy operation, short measurement time, and convenient data collection and post-processing. In XRD, incident X-rays are radiated into the material at different angles, and the scattered intensities of the diffracted beam are plotted against the angle of incidence X-ray beam. These data provide valuable information about the crystal arrangement. XRD analysis on thin perovskite film is used to understand the formation of the 2D layered structure and preferable growth orientation reference to the substrate surface. Pure 2D perovskites usually form in the orientation parallel to the substrate and show reflection peaks of (001) in the XRD. However, when it comes to quasi-2D perovskites, which are partially formed perpendicular to the substrate, replace the (001) reflections in the XRD with (0k0). Also, the other reflections related to (111) and (202) planes are visible in the XRD analysis.[120]

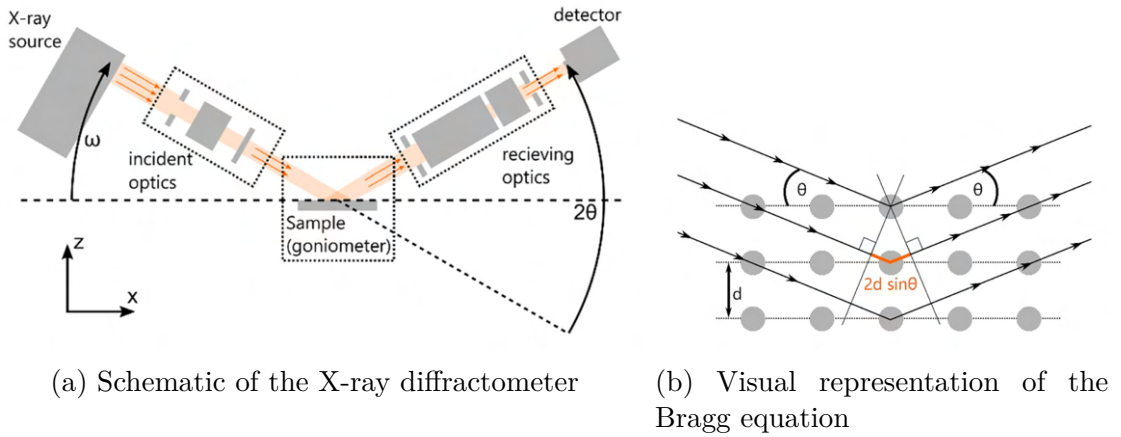


Figure 2.3: Sample analysis with an X-ray diffractometer.[121]

A scattered X-ray beam produces constructive interference occurs when the following conditions are met:

1. Incidence angle = Scattering angle.
2. The path length difference is equal to the integer multiplication of wavelengths.

This is known as Bragg's equation:[122]

$$n\lambda = 2d\sin\theta \quad (2.1)$$

Where,

- n: Diffraction order,
- λ : The wavelength of X-ray radiation,
- d: Distance between adjacent layers of atoms or molecules,
- θ : Glancing angle (Defined angle at which constructive interference occurs)

This equation is applied to analyze inter-layer distances in 2D hybrid perovskite. A silicon substrate (1.5 x 2 cm) with an oxide layer of 300 nm is used for thin film preparation of XRD measurements. The substrates are spin-coated with recipe C and annealed at 100°C for 10 minutes. The freshly prepared thin films are analyzed

with a Bruker diffractometer which is precalibrated using silicon substrate with a 300 nm oxide layer.

2.2.3 Grazing incidence wide angle X-ray scattering

X-ray techniques such as XRD and GIWAXS are widely used in hybrid perovskites and organic semiconductors to probe information related to internal morphology. Information specific to in-plane layers can not be observed by using XRD. When it comes to GIWAXS, it is capable of capturing in-plane and out-of-plane crystallographic information in polycrystalline perovskite films. Information regarding crystallinity, crystal orientation, crystal size, and layer spacing can be obtained. In contrast to grazing-incidence small-angle X-ray scattering (GISAXS), which is used to analyze length scales corresponding to nanophase separation, GIWAXS is used for scales corresponding to molecular packing.[123]

Compared with GISAXS, GIWAXS is more popular in analyzing perovskites, and there are several advantages of this technique, such as considerably high signal-to-noise ratio, non-destructive and non-contact probing, a large amount of structural information, depth resolution, and in-situ observation. Crystallographic information about perovskites affects optoelectronic and material properties. Diffraction patterns from 2D GIWAXS provide Debye-Scherrer rings for specific crystal planes. This helps to characterize the structural orientation of perovskite films.[124]

Geometry of GIWAXS diffraction

The incident X-ray (\vec{k}_i) penetrates the sample at a shallow angle (α_i) and generates a scattered beam (\vec{k}_f) with an exit angle (α_f) relative to the sample surface. The exit plane has an azimuth angle (φ) relative to the plane of the incident beam. The direct beam is projected onto the origin of reciprocal space. The projection of the scattering wave vector (\vec{q}) onto the ($q_r - q_z$) plane has a polar angle (X) with respect to the q_z axis. Here, the polar angle (θ_B) indicates the smallest detectable X.[125]

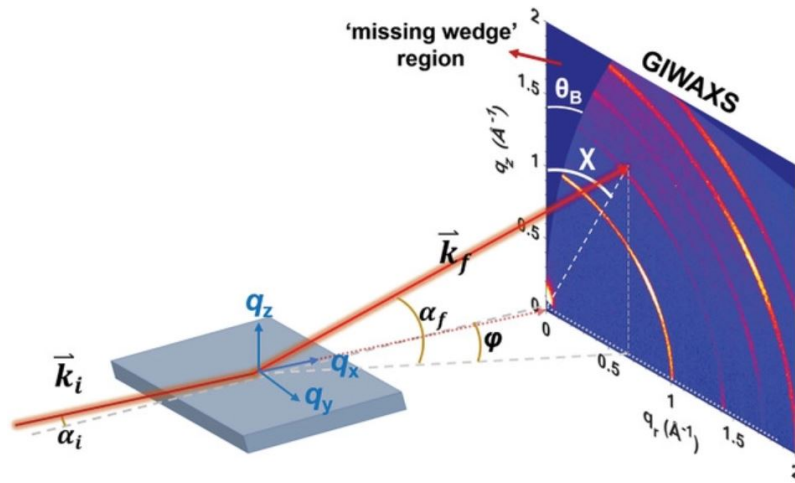


Figure 2.4: 2D GIWAXS pattern with scattering profile.[125]

X-ray beam \vec{k}_i projected onto the sample at grazing angle of α_i , The scattered beam

\vec{k}_f is recorded on the area detector. Scattering wave vector $\vec{q} = \vec{k}_f - \vec{k}_i$ is given by below components:

$$q_x = \frac{2\pi}{\lambda}(\cos\alpha_f \cos\varphi - \cos\alpha_i) \quad (2.2)$$

$$q_y = \frac{2\pi}{\lambda}(\cos\alpha_f \sin\varphi) \quad (2.3)$$

$$q_r = \sqrt{q_x^2 + q_y^2} \quad (2.4)$$

$$q_z = \frac{2\pi}{\lambda}(\sin\alpha_i + \sin\alpha_f) \quad (2.5)$$

The shape and intensity of GIWAXS patterns on the reciprocal ($q_{xy} - q_z$) plane can be used to interpret the orientation of the crystal. A thin film without any preferred crystal orientation shows uniform ring-shaped diffraction. A material with a preferred out-of-plane direction and random in-plane arrangement shows an arc-shaped diffraction pattern, and more uniformly arranged thin films show high-intensity spots as diffraction.

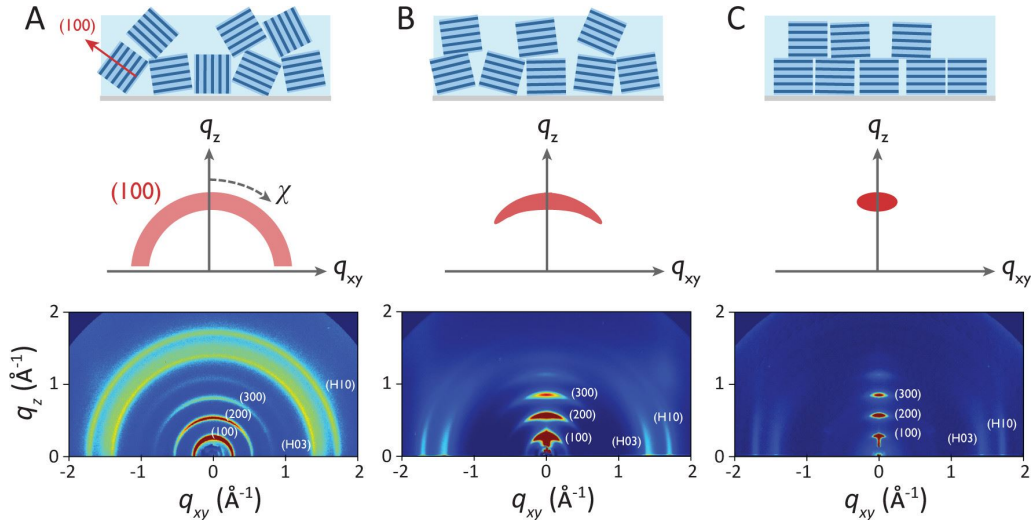


Figure 2.5: The shape of GIWAXS diffraction (a). Ring, (b). Arc, (c). Ellipse.[126]

A silicon substrate (1.5 x 2 cm) with an oxide layer of 300 nm is used for thin film preparation of GIWAXS measurements. The substrates are spin-coated at 4000 rpm with all the three types of solvent recipes (A, B & C) and annealed at 100 °C for 10 minutes. The prepared substrates are measured at the synchrotron facility (Delta, Beamline 9) in Technische Universität Dortmund. All the substrates are measured within 24 hours of preparation and transported in fully air-sealed containers to avoid environmental degradation.

2.2.4 Ultra-violet visible spectroscopy

The wavelength of light source from ultra-violet to visible is used in UV-visible spectroscopy. Usually, the samples are illuminated with light, and the absorption spectrum is recorded according to its wavelength. Since the absorption of light depends on the change of electronic state in the molecular structure of the sample, this spectrum is unique to the material. This can be used to distinguish materials with different molecular structures. Also, the electronic band-gap of the materials can be calculated.[127]

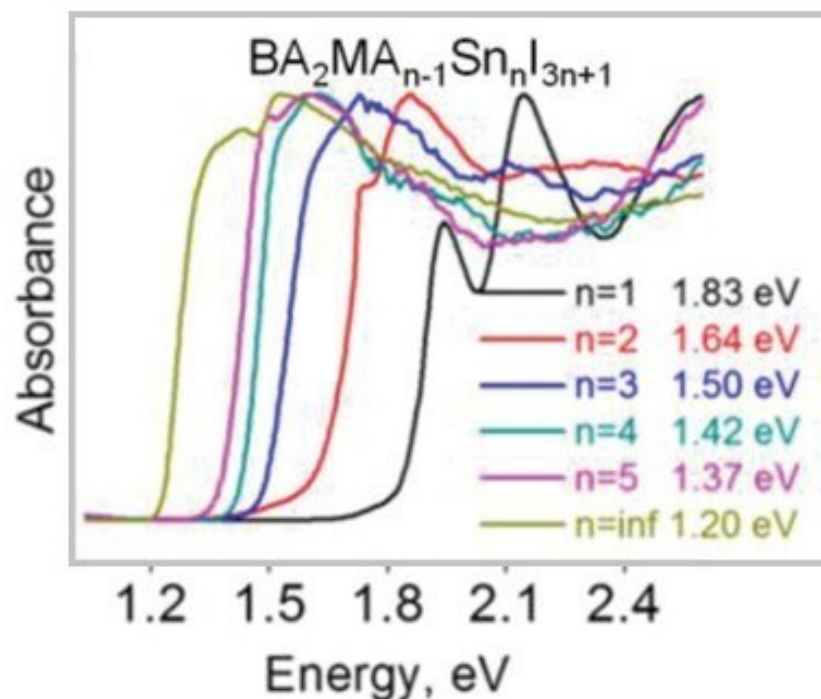
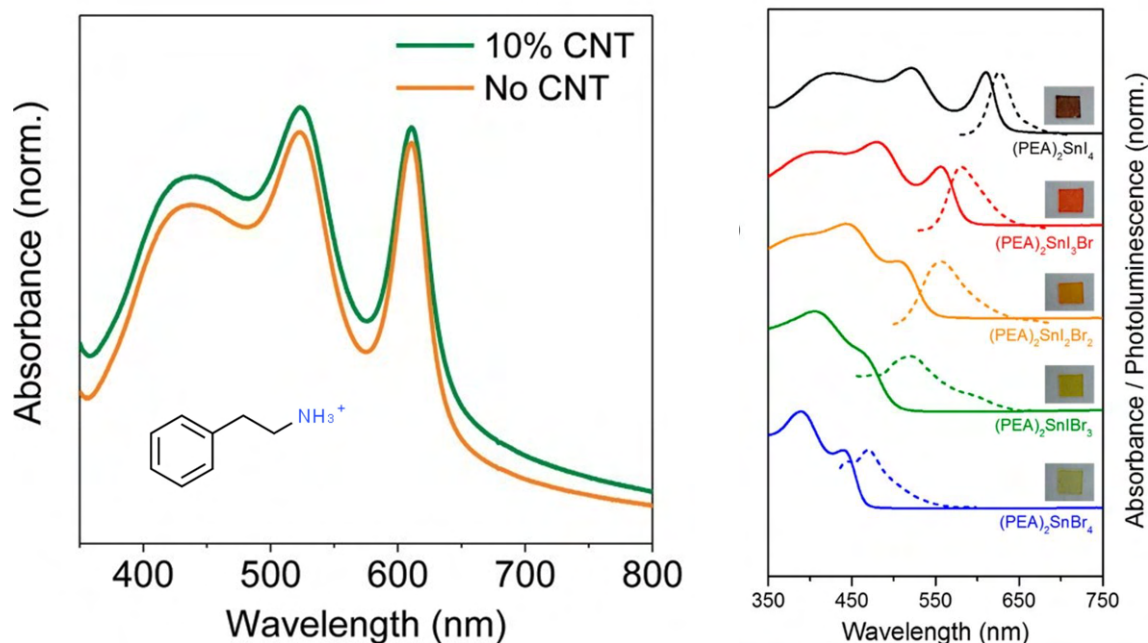


Figure 2.6: Absorption spectrum of $(\text{BA})_2(\text{MA})_{n-1}\text{Sn}_n\text{I}_{3n+1}$ when n becomes infinity it is considered as 3D perovskite. A shift in the optical bandgap of the material is observed, with 3D perovskites having a bandgap of 1.20 eV , while pure 2D perovskites have a higher bandgap of 1.83 eV . [128]

2D organic-inorganic hybrid perovskites are considered as natural quantum well structures with organic barriers.[34] Absorption spectrum of 2D perovskite shows blue-shift hundreds of nanometers than their 3D counterparts, which attributes to the strong quantum confinement effect. Excitons are more stable in layered structures than in bulk 3D perovskites and this is proven by the binding energy of 2D perovskites which is nearly ten times higher.[129]



(a) In comparison to absorption spectrum of most commonly used (PEA)₂SnI₄, [130] alkyl ammonium-based perovskite shows a narrow blue-shift in the peaks.

(b) Absorption spectrum of (PEA)₂SnX₄, [17] which shows the effect of halide anions.

Figure 2.7: The absorption spectrum of 2D hybrid Sn(II)-based perovskite with bench-marked organic cation PEA.

Since peaks in the absorption spectrum are known to originate from inorganic framework, it could be comparable to the other tin-iodide based pure 2D perovskites reported in the literature. [17] However, when it comes to 3D and quasi 2D tin-iodide perovskites, it shows a red-shift due to reduced quantum and dielectric confinement effects. Also, tin-based 2D perovskites with different types of halide anions show changes in absorption spectrum due to structural differences in the inorganic framework.

A glass substrate (1.5 x 2 cm) is used for thin film preparation of UV-visible spectroscopy measurements. The substrates are spin-coated with recipe C and annealed at 100 °C for 10 minutes. The freshly prepared thin films are analyzed with a UV-visible absorbance spectrometer which is precalibrated using a glass substrate.

2.2.5 Optical microscopy

Understanding the overall quality of the spin-coated film is important when analyzing the extrinsic factors involved in mobility. By using optical microscopy, structures as small as hundreds of micrometers can be analyzed. Large impurities and cracks can also be observed.

A silicon substrate (1.5 x 2 cm) with an oxide layer of 300 nm is used for thin film preparation of optical microscopy. The substrates are spin-coated with all the three solvent recipes (A, B & C) and annealed at 100 °C for 10 minutes. The

freshly prepared thin films are analyzed with a Leica DM optical microscope at three different magnifications such as 5X, 10X, and 50X.

2.2.6 Atomic force microscopy

AFM is used to understand the morphology of perovskite films on a micrometer scale. In contrast to scanning electron microscopy, AFM could be able to produce a 3D surface profile. This technique is useful for investigating the size of crystal grains and boundaries. In addition, other parameters such as surface roughness of thin film can be measured. This is used to investigate extrinsic effects which influence the charge transport of perovskites.

A silicon substrate (1.5 x 2 cm) with an oxide layer of 300 nm is used for thin film preparation of AFM. The substrates are spin-coated with all the three solvent recipes (A, B & C) and annealed at 100 °C for 10 minutes. The freshly prepared thin films are analyzed with a Bruker dimension ICON scanner in non-contact mode. The samples are analyzed in scan sizes of 50 μm and 10 μm .

2.3 Device measurement

The device measurements are performed using Keithley 4200-SCS semiconductor parameter analyzer. 2D perovskite FETs are measured at three different temperatures such as 100 K, 200 K, and room temperature (295 K). At first, fabricated devices are loaded into an ultrahigh vacuum and low-temperature probe station and kept for around 20 minutes to reach the vacuum pressure of 50 *mTorr*. Following this, the cooling system is turned on for the devices to reach the temperature of 100 K, which takes around 5 hours in approximation. Thereafter, the cooling system is turned off to stabilize the temperature. At first, the devices are measured at 100 K, then kept for around 24 hours for the temperature to reach 200 K gradually. Again device performance is measured at this temperature, then waited 48 hours for the probe station to reach room temperature. Again at this level, device performance is measured. It is vital to kept at ultra-high vacuum conditions to avoid any environmental deterioration of the perovskite transistor and to reduce the external noise.

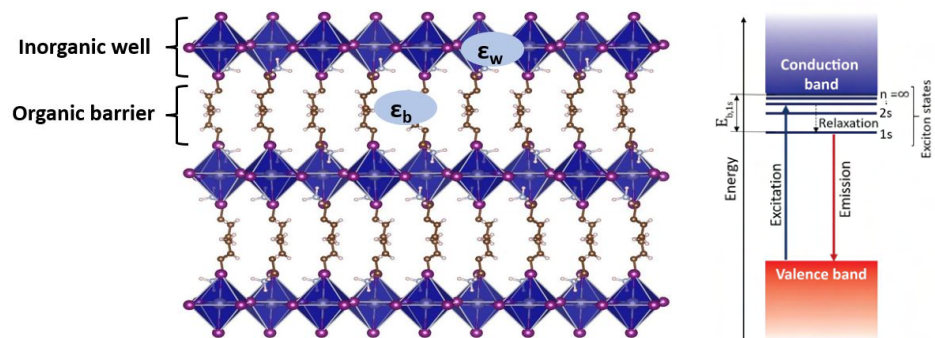
The transfer characteristics are measured in pulse mode and output characteristics are measured in continuous mode. In pulse mode, short impulses of gate voltage V_g are applied for a 1 s duration. Transfer curves are plotted for drain-source current I_{ds} against varying the gate voltage V_g from +60 V to -60 V while keeping $V_{ds} = -60$ V constant and the output curves plotted I_{ds} against varying drain-source voltage V_{ds} from 0V to -60V at different gate voltages V_g of 0V, -20V, -40V and -60V.

Chapter 3

Results and discussion

3.1 Optoelectronic properties

Excitons are responsible for optoelectronic processes in semiconductors, which are the basis for the operation of optoelectronic devices such as LEDs, OLEDs, solar cells, and others.[131] The term exciton is defined as pair of electron and holes which is attracted to each by Coulomb interaction, this occurs when the desired amount of photon energy absorbed by a material, electrons in the valence band get excited and moves to the conduction band, the energy absorbed during this process are referred to as exciton binding energy.[132] In order to understand the optoelectronic properties of 2D hybrid perovskites, an understanding of excitonic binding energy is essential. 2D perovskite structures are significantly different from their 3D counterparts, which have unique quantum-confined thin inorganic layers and insulating organic spacers. Also, the dielectric properties between inorganic framework and organic spacers are considerably different.[34] It would be interesting to understand the correlation between the exciton binding energy of 2D tin-iodide perovskite with different alkyl ammonium cations using theoretical and experimental tools.



(a) Quantum well structure of 2D perovskite, where the mismatch between the dielectric constants of the inorganic layer (ϵ_w) and organic spacers (ϵ_b) creates a dielectric confinement effect.

(b) Exciton band structure of a material.[133]

Figure 3.1: Illustration of 2D quantum well structure and exciton binding energy band diagram.

The model for excitons in semiconductors is known as Wannier–Mott exciton. In this model, the lowest energy state of the exciton is known as 1s exciton, and binding energy relevant to this is given as $E_{b,1s}$. Higher exciton energy value related to conduction band minimum is referred to as a more stable excitonic state and this defines the stability of an exciton. The material with higher binding energy is suitable for light-emitting diodes (LED) and lower binding energy is desirable for photovoltaics.

The attractive force between the electron and hole in the exciton is given by:

$$F = -\frac{1}{4\pi\epsilon} \frac{e^2}{r^2} \quad (3.1)$$

Where (r) distance between electron and hole, (ϵ) dielectric constant of lattice and (e) elementary charge.

Energy expressed in following form for excitonic states:[134][135] $n = 1, 2, 3, \dots$,

$$E_b^{2D} = \frac{n^2 E_b^{3D}}{\left(n - \frac{1}{2}\right)^2} \quad (3.2)$$

Where E_b^{2D} and E_b^{3D} are the binding energy of the n^{th} excitonic states of 2D and 3D structures.

Exciton binding energy calculated for 1s excitons is given by $E_b^{2D} = 4E_b^{3D}$. However, for this to be true, both system conditions should be identical. In the case of 2D hybrid organic-inorganic perovskite, the dielectric constant (ϵ) of the barrier layer (ϵ_b) is smaller than the quantum well layer (ϵ_w). The difference in dielectric constants between layers is suggested to enhance binding energies.[136] This effect is called as dielectric confinement and it was reported by Rytova[137] and Keldysh[138]. If binding energy is influenced only by quantum confinement, 2D perovskite structures should only have around four times the exciton binding energy of 3D perovskites. However, the excitonic binding energy is $490 \pm 30 \text{ meV}$ for pure 2D $(\text{C}_4\text{H}_9\text{NH}_3)_2\text{PbI}_4$ perovskite based on the experimental results.[139] This binding energy is much higher than corresponding quasi-2D (370 meV) and 3D systems (37 meV).[140][141] Therefore both quantum and dielectric confinement influence exciton binding energy.

In the 2D limit, if we assume zero well width and infinite barrier potential for a single QW, the increase of exciton binding energy in 2D relative to their 3D counterpart is given by:[138]

$$E_b^{2D+\epsilon} = 4 \left(\frac{\epsilon_w}{\epsilon_b}\right)^2 E_b^{3D} \quad (3.3)$$

It is visible that equation (3.3) is advancement from equation (3.2) by taking consideration of difference in dielectric constants by multiplying $\left(\frac{\epsilon_w}{\epsilon_b}\right)^2$.

The reduction of dielectric confinement in 2D hybrid perovskites and corresponding exciton binding energy has been reported with large polar organic spacers. This was

demonstrated in $(\text{HOCH}_2\text{CH}_2\text{NH}_3)_2\text{PbI}_4$ where the organic material has a significantly higher dielectric constant ($\epsilon \approx 37$) compared to conventional organic spacer PEA ($\epsilon \approx 4$). The dielectric confinement is greatly reduced, and the exciton binding energy is 20 times smaller than conventional 2D perovskites.[142] A similar trend can be predicted for alkyl ammonium cations. Since the dielectric constant of the organic spacer layer is directly proportional to the number of carbon atoms in the linear chain, according to the above-mentioned equation (3.3), it can be predicted that the exciton binding energy will gradually increase with the length of alkyl ammonium spacers.

Organic spacers	Dielectric constant (ϵ)
Propylamine	5.35
Butylamine	4.90
Pentylamine	4.27
Hexylamine	3.94
Heptylamine	3.81

Table 3.1: Dielectric constant values of alkyl ammonium cations, as the number of carbon atoms in the chain increases, the dielectric constant decreases proportionally.[143]

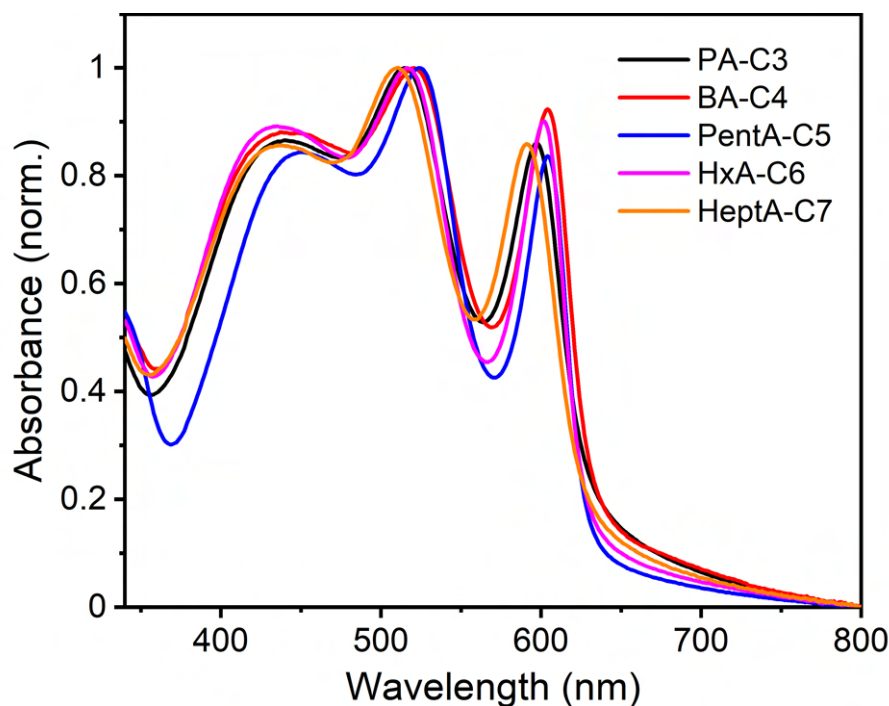


Figure 3.2: The absorption spectrum of 2D alkyl ammonium perovskites films, prepared at a concentration of 0.2 M in DMF:DMSO (1:1), spin coated at 4000 *rpm* and annealed at 100 °C for 10 minutes.

Properties of 2D perovskite films are investigated using UV-visible absorption spectroscopy. All the films with different alkyl ammonium spacers exhibit similar behavior. The first peak which is around 430 nm corresponds to high-energy exciton

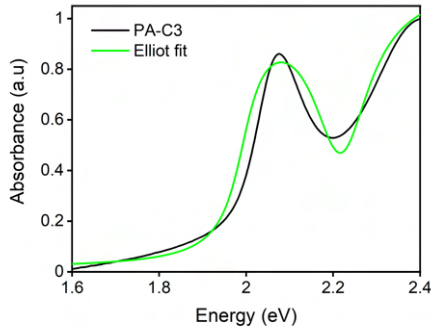
transition energy levels. The second peak around 520 nm is related to the inter-band transition process in perovskite and the third sharp peak around 600 nm is related to the recombination of intrinsic excitons.[144][34][130]

Exciton binding energy approximation

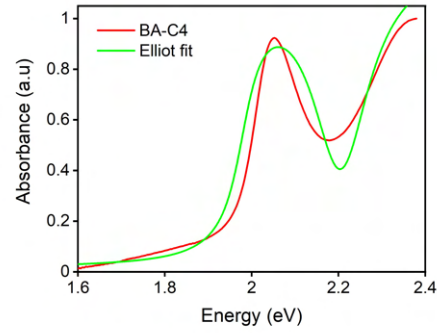
Wannier exciton binding energy (E_b) of direct semiconductors can be calculated effectively by fitting the band-edge absorption spectrum using Elliot formula.[145] According to the Elliot theorem, absorbance coefficient can be given as:[146][147]

$$\alpha(h\nu) = \alpha_0 \sum_n \left(1/n^3\right) (\Gamma_n/2)^2 / \left[(\Gamma_n/2)^2 + (h\nu - E_g + R_x/n)^2 \right] + \alpha_1 \left\{ \pi/2 + \arctan \left[(h\nu - E_g) / (\Gamma_c/2) \right] \right\} \quad (3.4)$$

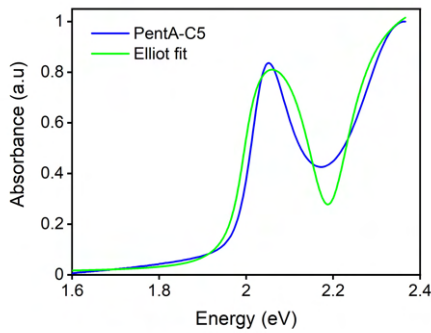
UV-visible absorption spectrum of samples recorded at room temperature is fitted in the above-mentioned equation. Where (α_0) absorption peak of exciton ground state, (α_1) is absorption peak at band gap, (E_g) optical band gap, (R_x) exciton binding energy, (Γ_n) and (Γ_c) are full width at half-maximum of Lorentzian and full width of continuum excitons.



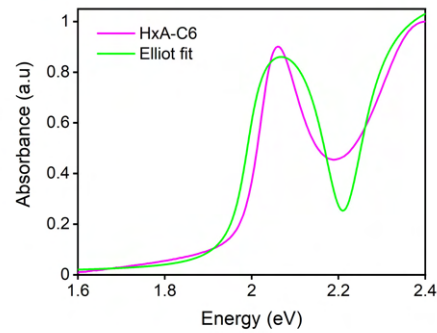
(a) $(\text{PA})_2\text{SnI}_4$; $E_b = 224 \text{ meV}$ and $E_g = 1.992 \pm 2 \text{ eV}$



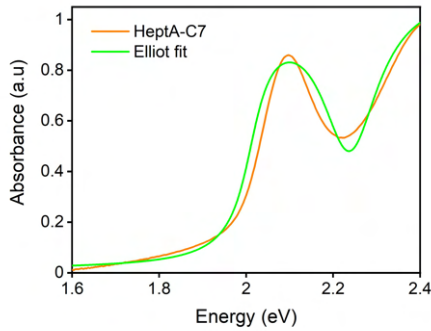
(b) $(\text{BA})_2\text{SnI}_4$; $E_b = 225 \text{ meV}$ and $E_g = 1.979 \pm 2 \text{ eV}$



(c) $(\text{PentA})_2\text{SnI}_4$; $E_b = 193 \text{ meV}$ and $E_g = 1.995 \pm 2 \text{ eV}$



(d) $(\text{HxA})_2\text{SnI}_4$; $E_b = 220 \text{ meV}$ and $E_g = 1.990 \pm 2 \text{ eV}$



(e) $(\text{HeptA})_2\text{SnI}_4$; $E_b = 226 \text{ meV}$ and $E_g = 2.011 \pm 2 \text{ eV}$

Figure 3.3: Absorbance spectrum and corresponding Elliot fit curves are used to calculate the optical band gap (E_g) and exciton binding energy (E_b) of 2D perovskite.

The fitted values for exciton binding energies are in the range of $193 - 223 \text{ meV}$ for alkyl ammonium cations. However, based on the theoretical equations, there should be a gradual increase in binding energy in reference to the number of carbon atoms in the alkyl chain. This kind of trend is not observed in the calculated values based on experimental UV-visible absorbance spectrum. Probably this is due to an error

in non-linear curve fitting of mathematical model. Even though Elliot fitting is a proven method to analyze exciton binding energy, values obtained from this method are accurate in the range of tens of meV.

3.2 Structural properties

The structural properties of hybrid perovskite thin film govern optoelectronic and electrical transport properties of the material. The change in organic spacers, solvent type and concentration in precursors directly influence various microstructure properties from molecular level to device scale. Four main techniques have been used to probe the information from thin film such as optical microscopy, atomic force microscopy (AFM), X-ray diffraction (XRD) and grazing incidence wide angle spectroscopy (GIWAXS). The optical microscopy is only capable of obtaining device scale microstructural information, AFM is used for 3D morphological information at sub-micron level, XRD & GIWAXS are useful for information related to crystal structure.

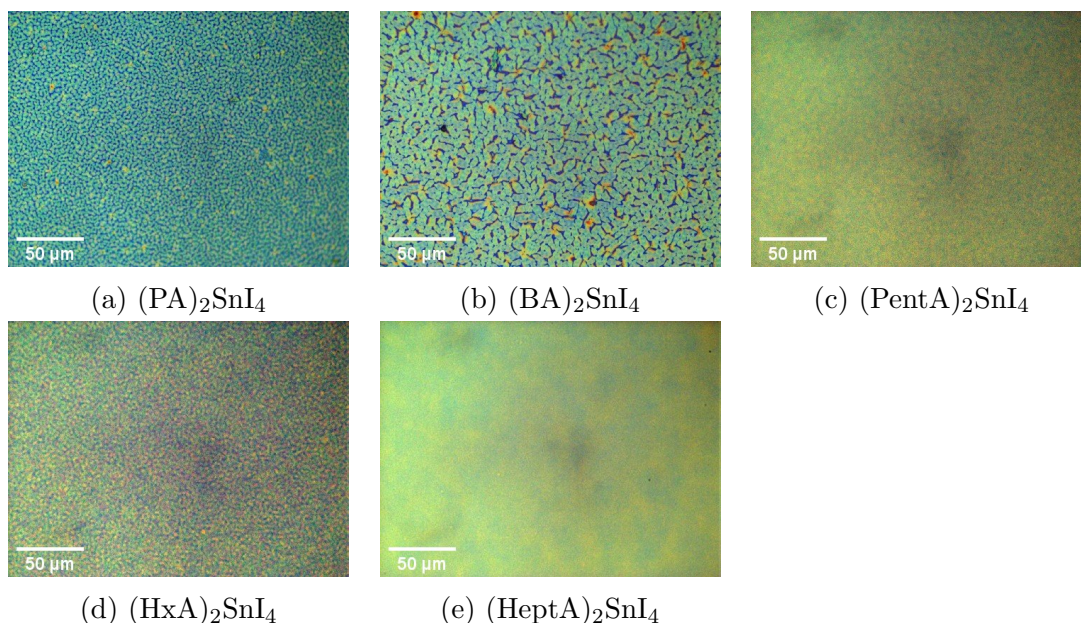


Figure 3.4: Optical microscopy images of perovskite films, prepared at a concentration of 0.1 M in DMF, spin-coated at 4000 *rpm* and annealed at 100 °C for 10 minutes. The optical microscopy images of alkyl ammonium perovskites prepared with different recipes are attached in appendix A.

Based on optical microscopy images, shorter carbon chain alkyl ammonium perovskites usually shows distinguished domain separation (Figure 3.6 a and b). The higher carbon number alkyl ammonium perovskites usually forms more smoother films without any visible domain boundaries (Figure 3.6 d and e). This can directly affects the charge transport properties of perovskite since these domain boundaries act as charge traps and ion migration pathways. When it comes to longer carbon chain alkyl ammonium perovskites separation between domain boundaries visibly disappeared.

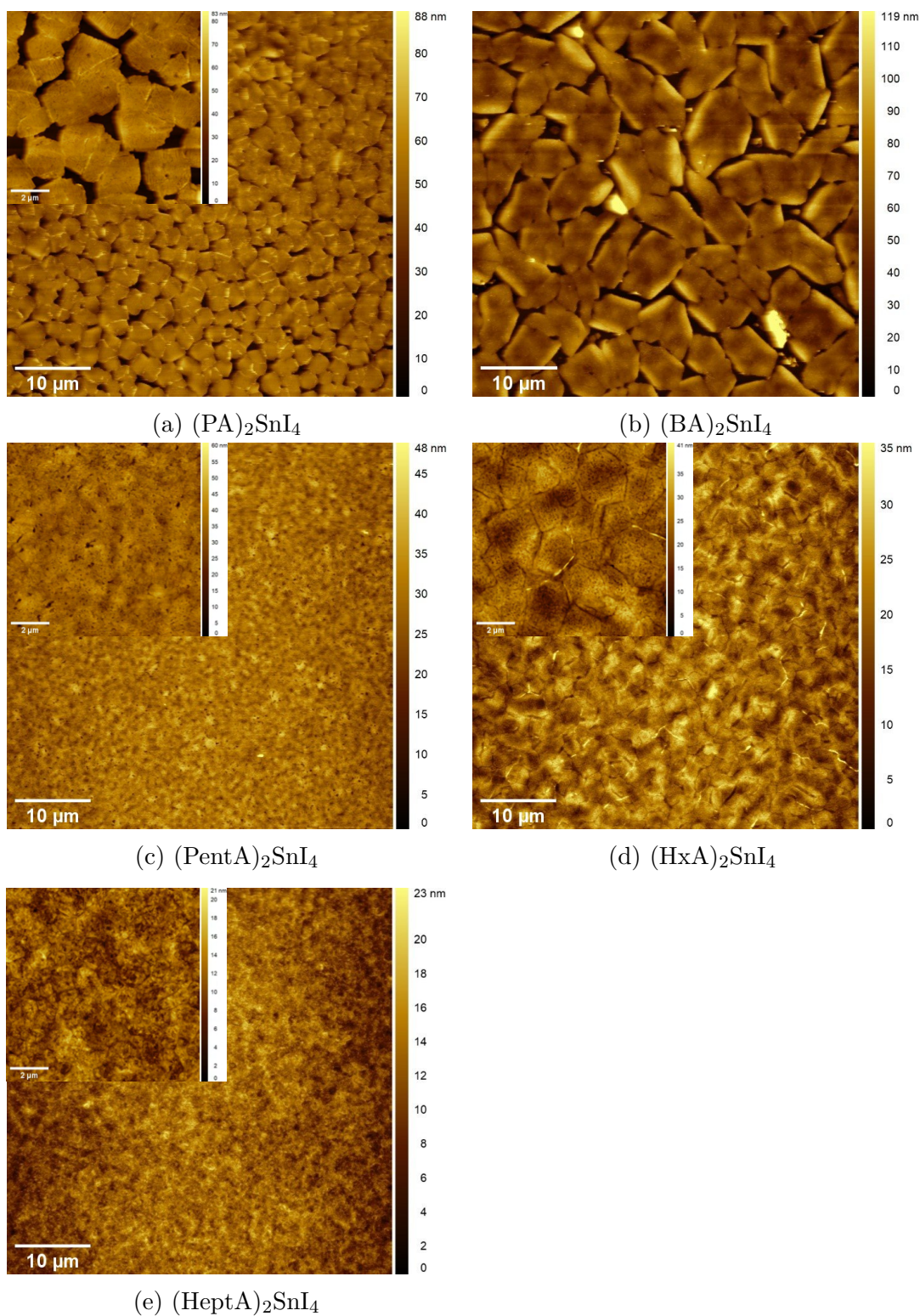


Figure 3.5: Atomic force microscopy images of different perovskite films, prepared at a concentration of 0.1 M in DMF, spin coated at 4000 *rpm* and annealed at 100 °C for 10 minutes. The AFM images of alkyl ammonium perovskites prepared with different recipes are attached in appendix B.

Based on the AFM images, clear separation between grains/domains and pinholes can be observed in perovskite film with lower carbon number alkyl ammonium spac-

Organic spacers	Surface roughness (nm)	Width of grain boundary (μm)
(PA) ₂ SnI ₄	8.7	1.89
(BA) ₂ SnI ₄	17.4	5.72
(PentA) ₂ SnI ₄	3.8	0.68
(HxA) ₂ SnI ₄	4.5	1.69
(HeptA) ₂ SnI ₄	2.7	0.71

Table 3.2: Surface roughness and the average size of grain boundaries of perovskite films.

ers. However, this grain boundary separation disappears with a higher carbon number, which was mentioned in optical microscopy data. This can be considered as one of the critical factors influencing charge carrier mobility. Trap states at grain boundaries in polycrystalline perovskites are known to deteriorate optoelectronic performance. Several additive engineering techniques such as the introduction of semiconducting molecules with Lewis acid or base functional groups are used to passivate the grain boundaries have been reported in several studies.[148][67] A clear correlation could not be observed between the grain size and charge carrier transport; the most critical factor affecting the charge carrier transport is a separation between the grains/domains rather than the grain size. The surface roughness dominated scattering is also known to influence the charge carrier mobility, this is mainly applicable to two-dimensional layered charge carrier transport interfaces; as we can see from the calculated surface roughness of shorter alkyl chain perovskites, the numerical value is relatively higher than longer alkyl chain perovskites, this is also seen to effect charge carrier transport in perovskites.[149]

XRD measurements of alkyl ammonium perovskite provide useful information related to crystal structure. The length of organic spacers are proportionally affecting the inter-layer distance between inorganic layers. This is proven by XRD measurements of thin perovskite film and calculated inter-layer distance from XRD peaks using Bragg's equation.

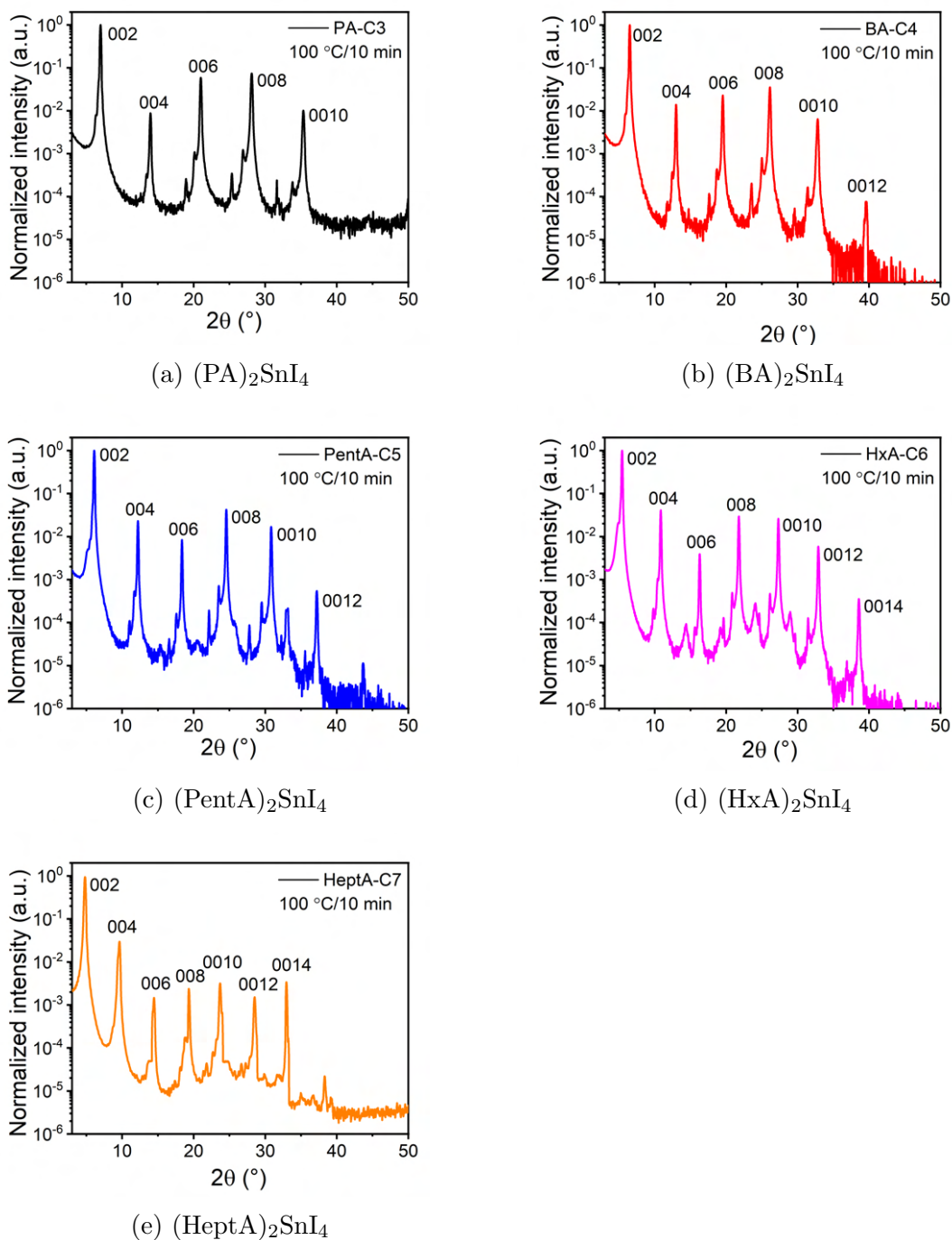
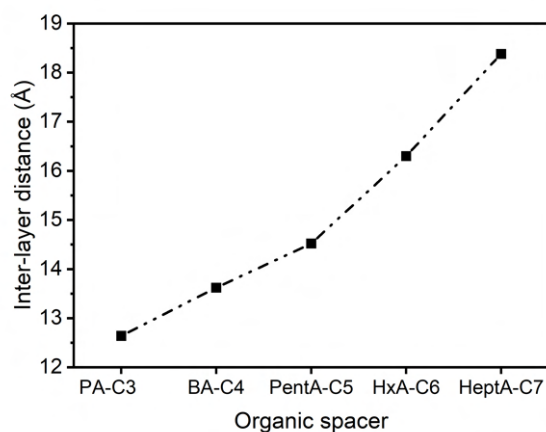


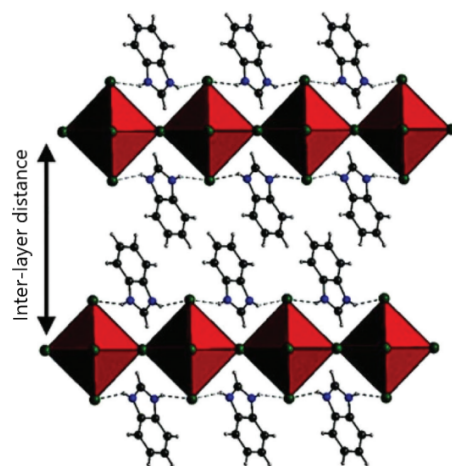
Figure 3.6: X-ray diffraction patterns of perovskite films with different alkyl ammonium cations, prepared at a concentration of 0.2 M in DMF:DMSO (1:1), spin coated at 4000 *rpm* and annealed at 100 °C for 10 minutes.

Organic spacers	Glancing angle	Inter-layer distance (Å)
(PA) ₂ SnI ₄	7.00°	12.64
(HA) ₂ SnI ₄	6.49°	13.62
(PentA) ₂ SnI ₄	6.09°	14.52
(HxA) ₂ SnI ₄	5.42°	16.30
(HeptA) ₂ SnI ₄	4.81°	18.38

Table 3.3: Calculated inter-layer spacing of perovskite with different alkyl ammonium cations.



(a) Interlayer distance vs. alkyl ammonium organic spacers



(b) Illustration of inter-layer distance in 2D perovskite.[150]

Figure 3.7: The calculated inter-layer distances of alkyl ammonium-based perovskites.

XRD analysis of alkyl ammonium-based perovskite shows peaks at periodic intervals relevant to (00l) crystal orientation. Based on this analysis, it can be verified that layered structures are forming parallel to the substrate. By measuring the angles related to high-intensity peaks, the inter-layer distance between adjacent inorganic layers can be calculated using Bragg's law.

GIWAXS pattern of hybrid perovskite

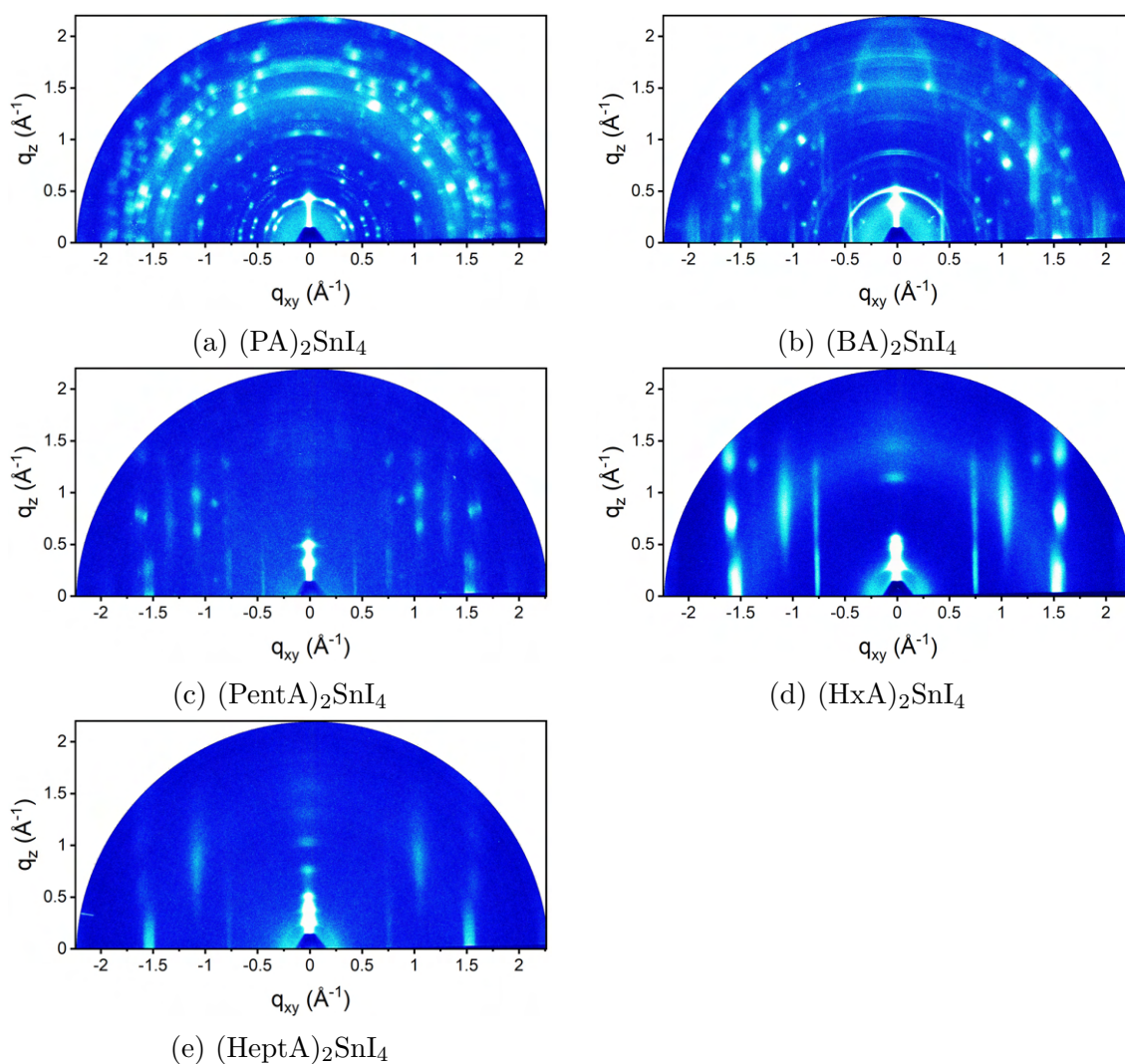


Figure 3.8: GIWAXS images of perovskite films, prepared at a concentration of 0.2 M in DMF, spin-coated at 4000 *rpm* and annealed at 100 °C for 10 minutes. The GIWAXS images of alkyl ammonium perovskites prepared with different recipes are attached in appendix C.

GIWAXS patterns of butylammonium ($(\text{BA})_2\text{SnI}_4$) and hexylammonium ($(\text{HxA})_2\text{SnI}_4$) based perovskite thin films have been simulated using single-crystal unit cell data from the literature.

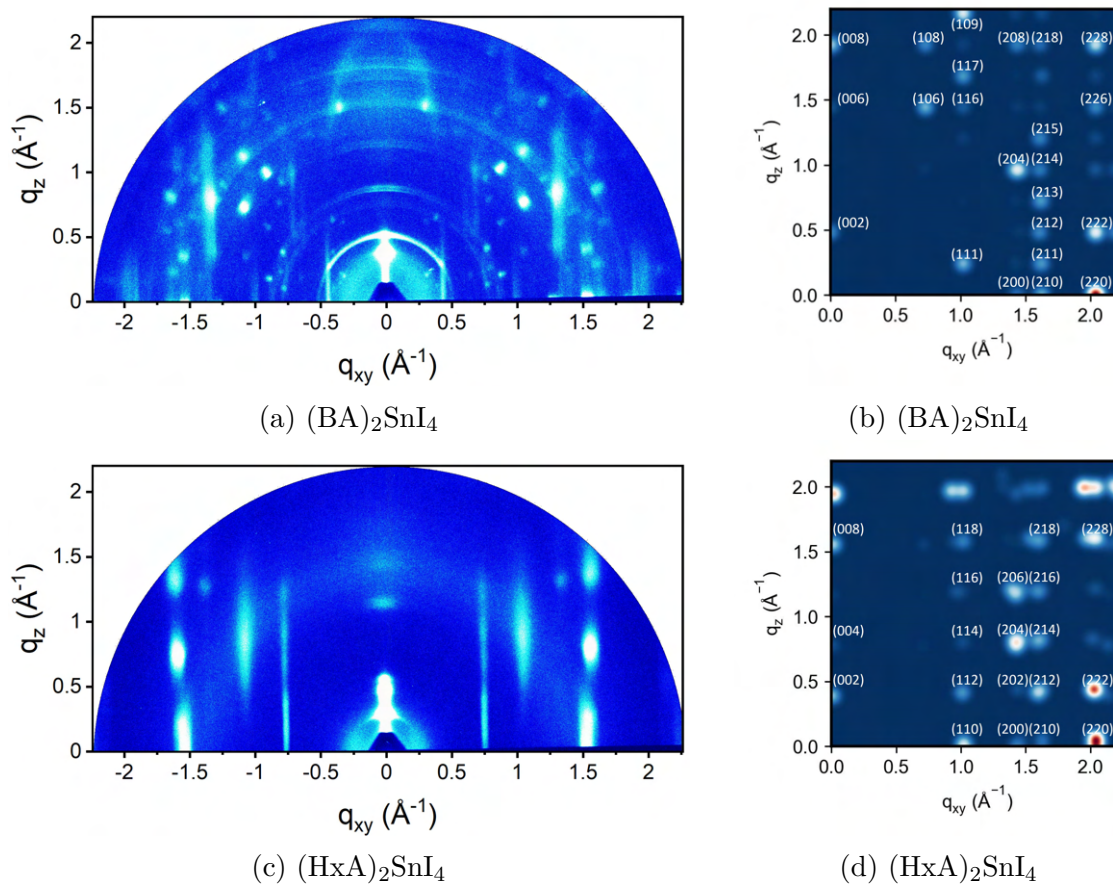


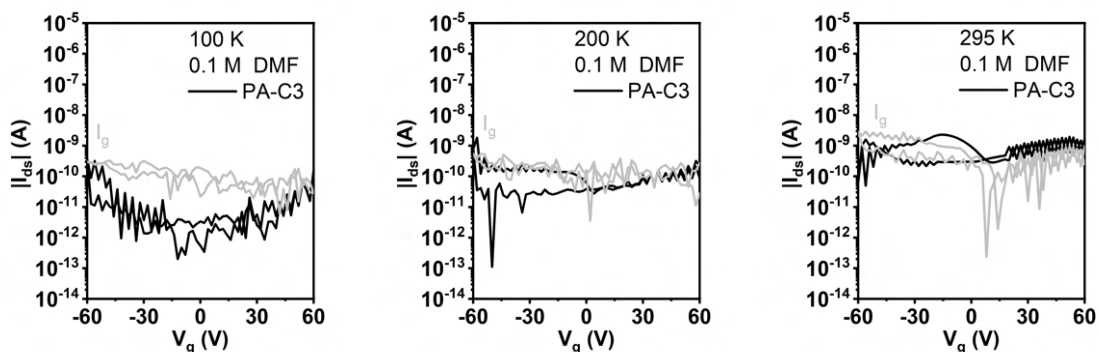
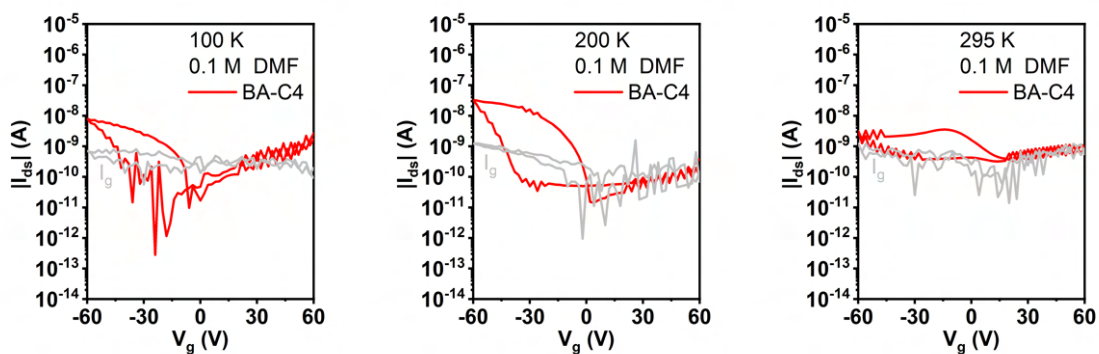
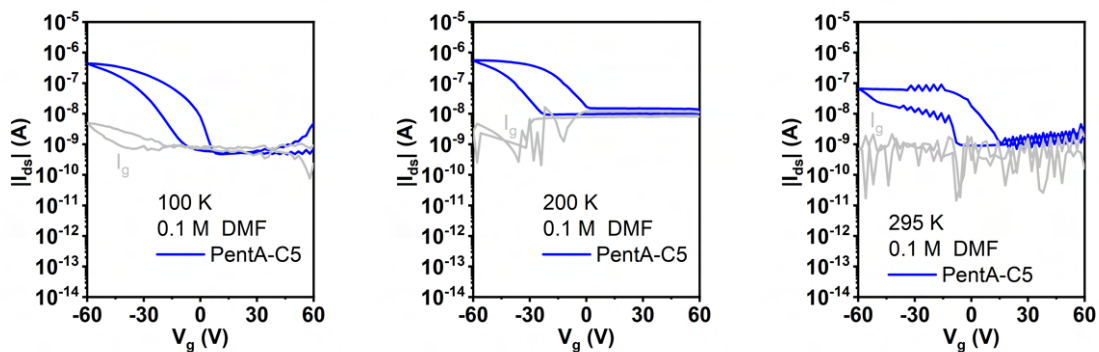
Figure 3.9: Experimental GIWAXS diffraction images and corresponding simulated pattern with miller indices.

The crystal orientation of the alkyl ammonium-based polycrystalline perovskite film can be visualized using the GIWAXS diffraction pattern. When it comes to low-carbon alkyl ammonium-based perovskites, ring-shaped diffraction patterns can easily be observed in addition to sharp elliptical patterns, This clearly shows some level of randomly oriented hybrid perovskite 2D layers that are not parallel to the silicon substrate. This phenomenon disappears with longer alkyl chain spacers. This can be interpreted as well-organized perovskite layers parallel to the substrate in a longer alkyl chain. However, there is another interesting observation that the pattern intensity also decreases with longer carbon spacer. That means although perovskite layers are well-organized, crystallinity drops with a longer carbon chain. There should be a balance between the orientation of the perovskite layer and the crystallinity to achieve better electrical transport and optoelectronic properties.

3.3 Device performance

Devices exhibit the behavior of a p-type transistor. Perovskites synthesized with lower carbon alkyl ammonium cations did not show on-off behavior of the transistors. Higher carbon devices show on-off behavior with large hysteresis. The ion migration accumulated at perovskite and dielectric interface will screen the applied electric field. This results in poor and unreliable current modulation at room temperature

and significantly large hysteresis in forward and reverse sweep of current-voltage output curves.[151][107] This observed behavior in polycrystalline films generally dominates via grain boundaries.[152]

(a) $(PA)_2SnI_4$ (b) $(BA)_2SnI_4$ (c) $(PentA)_2SnI_4$

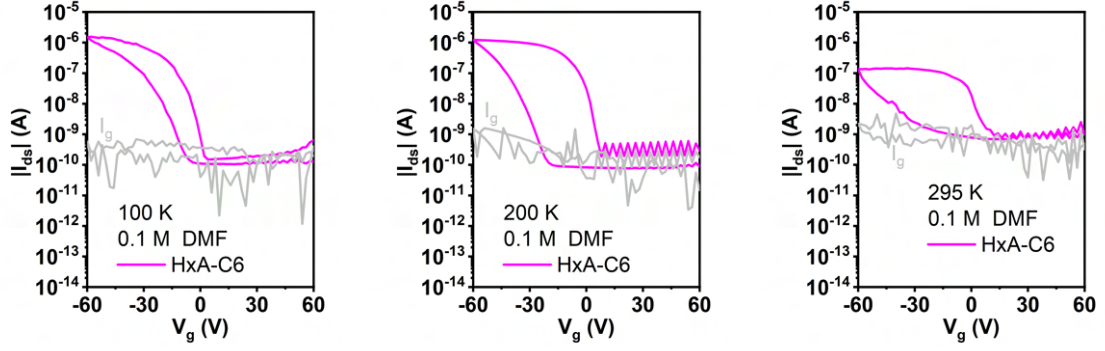
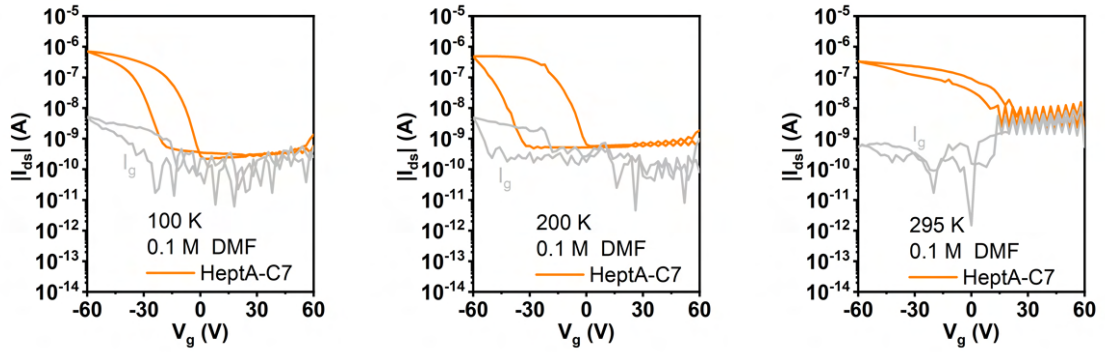
(d) $(\text{HxA})_2\text{SnI}_4$ (e) $(\text{HeptA})_2\text{SnI}_4$

Figure 3.10: Transfer characteristics of 2D alkyl ammonium based perovskite FETs measured at (a) 100 K, (b) 200 K, and (c) 295 K. The channel length and width are $L = 80 \mu\text{m}$, $W = 1000 \mu\text{m}$. The gray curve (I_g) shows the leakage current of the device prepared at 0.1 M in DMF, spin coated at 4000 rpm, and annealed at 100 °C for 10 minutes. The transfer characteristics of alkyl ammonium perovskite transistors prepared with different recipes are attached in appendix D.

3.3.1 Charge carrier mobility

Charge carrier mobility defines the ease of charge carriers to drift through a material when an electric field is applied to attract those charges.

This can be explained by below equation:

$$v_d = \mu E \quad (3.5)$$

Where E is the applied electric field across the material and v_d is the drift velocity which is the average velocity of charge carriers moving for the applied electric field, typically measured in $\text{cm}^2\text{V}^{-1}\text{s}^{-1}$).

Also the charge carrier mobility μ can be written as:

$$\mu = \frac{e\tau_c}{m^*} \quad (3.6)$$

Where, τ_c is mean free time and m^* is effective mass of charge carrier.

Based on the above definition, the mobility depends on the drift velocity, which is affected by the mean free time between scattering.

Charge carrier mobility in perovskite is controlled by intrinsic and extrinsic factors. Intrinsic parameters are derived from the interaction of charge carriers with the lattice, but extrinsic parameters are related to material imperfections such as grain boundaries, dislocations, impurities, and voids.

Based on the evidence from theoretical and experimental studies at room temperature, it is shown mobility of hybrid perovskites is limited by Fröhlich interactions between ionic lattice in LO phonon modes and charge carriers in the electric field. This type of interaction is known to dominate in ionic-inorganic semiconductors such as gallium arsenide (GaAs) in high-temperature regions. LO phonon mode usually involves oscillating metal atom in the perovskite, it is suggested to have a relatively smaller atom like Sn than Pb to improve the mobility. However, the potential for enhancement in mobility is limited by the oxidization of Sn^{2+} to Sn^{4+} which causes self-doping.[153]

Intrinsic parameter phonon scattering/coupling reduce mobility due to charge carrier trap and polaron formation. The charge traps are more significant in 2D material than in 3D counterparts and they are concentrated at surfaces and interfaces where the probability for deformation is higher in perovskites.[154]

The charge carrier mobility of 2D alkylammonium-based hybrid perovskites in saturation mode is calculated using the following formula:

$$\mu = \frac{2L}{WC_i} \left(\frac{\partial \sqrt{I_{ds}}}{\partial V_g} \right)^2 \quad (3.7)$$

where L , W and C_i are transistor channel length, width and unit capacitance of the oxide dielectric layer. The slope $\left(\frac{\partial \sqrt{I_{ds}}}{\partial V_g} \right)^2$ is obtained by plotting the square root of the drain-source current (I_{ds}) versus the gate voltage (V_g).

Cation	Solvent	Concentration (M)	Mobility ($cm^2V^{-1}s^{-1}$)		
			100 K	200 K	295 K
(PA) ₂ SnI ₄	DMF	0.1	-	-	-
(BA) ₂ SnI ₄	DMF	0.1	-	-	-
(PentA) ₂ SnI ₄	DMF	0.1	2.07E-03	4.87E-03	9.13E-04
(HxA) ₂ SnI ₄	DMF	0.1	1.2E-02	1.77E-02	4.51E-03
(HeptA) ₂ SnI ₄	DMF	0.1	6.55E-03	1.01E-02	1.15E-03
(PA) ₂ SnI ₄	DMF	0.2	-	-	-
(BA) ₂ SnI ₄	DMF	0.2	1.61E-04	5.88E-04	1.25E-04
(PentA) ₂ SnI ₄	DMF	0.2	3.34E-03	5.18E-03	1.9E-03
(HxA) ₂ SnI ₄	DMF	0.2	2.84E-02	4.36E-02	6.43E-03
(HeptA) ₂ SnI ₄	DMF	0.2	3.29E-02	5.21E-02	2.74E-03
(PA) ₂ SnI ₄	DMF:DMSO (1:1)	0.2	1.25E-04	4.09E-04	3.74E-05
(BA) ₂ SnI ₄	DMF:DMSO (1:1)	0.2	2.81E-03	8.01E-03	9.07E-04
(PentA) ₂ SnI ₄	DMF:DMSO (1:1)	0.2	3.75E-02	6.82E-02	2.61E-03
(HxA) ₂ SnI ₄	DMF:DMSO (1:1)	0.2	8.01E-03	1.7E-02	2.93E-03
(HeptA) ₂ SnI ₄	DMF:DMSO (1:1)	0.2	-	-	-

Table 3.4: Consolidated summary of charge carrier mobility for alkyl ammonium-based perovskite field-effect transistors fabricated with different precursor recipes (A, B & C).

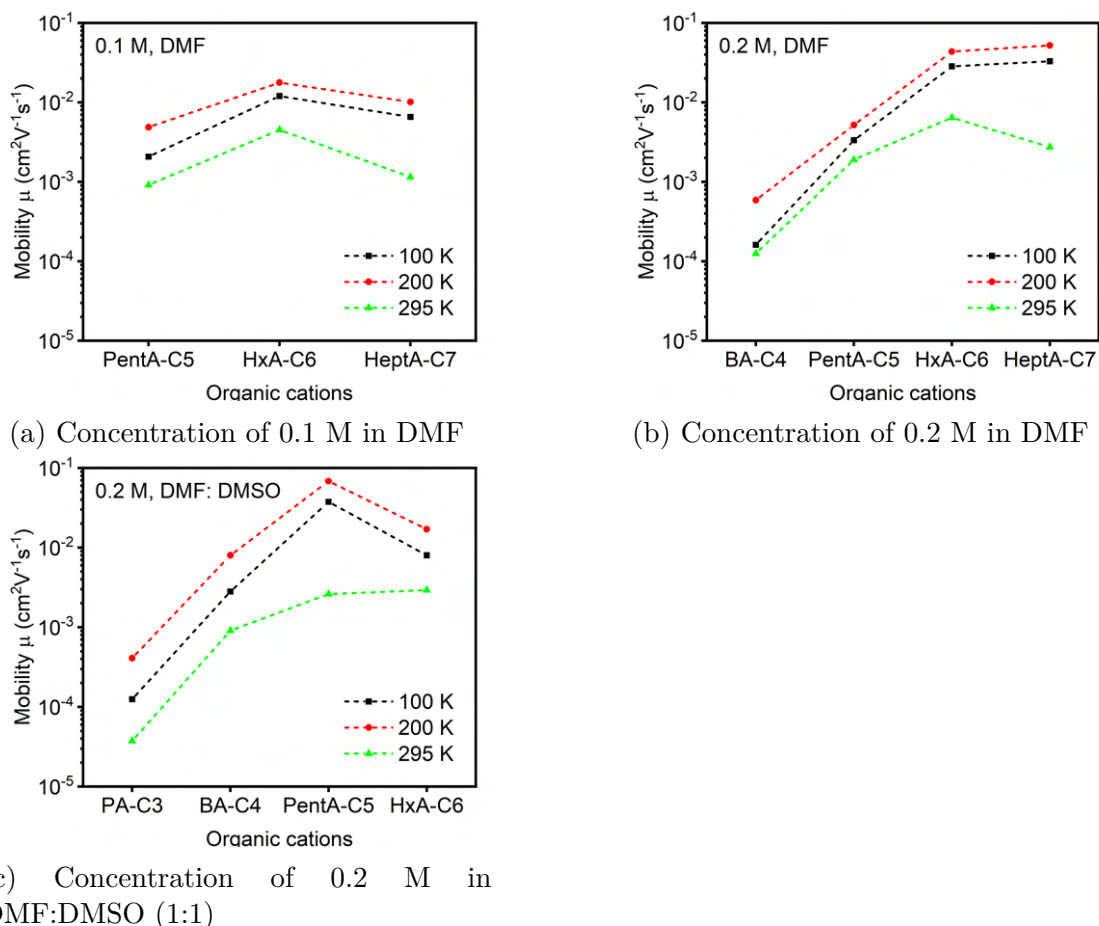


Figure 3.11: The charge-carrier mobility of tin-iodide-based 2D hybrid perovskite FETs with a different number of carbon atoms in alkyl ammonium spacers.

In the measured alkyl ammonium perovskites, device performance gradually increases with the number of carbon atoms in organic spacer. However, this pattern begins to drop starting from hexylammonium. But all the five alkylammonium-based perovskites share the same inorganic layer (Sn-I framework). The charge transport layer in perovskites is known to be inorganic framework, therefore discrepancy in overall charge carrier mobility should originate from organic spacers. The intrinsic factor such as molecular packing at atomic scale between inorganic layers and organic spacers can be used to explain this observation. In higher carbon number spacers, the presence of local gauche defects and distortion in the organic chain form potential well, enabling charge carrier localization and self-trapping. This conformational disorder of organic cations is observed in $[\text{CH}_3(\text{CH}_2)_{n-1}\text{NH}_3]_2\text{PbI}_4$ where the future increase in number of carbon ($n \geq 6$) in alkyl ammonium chain deteriorates the in-plane and out-of-plane charge carrier mobility.[155]

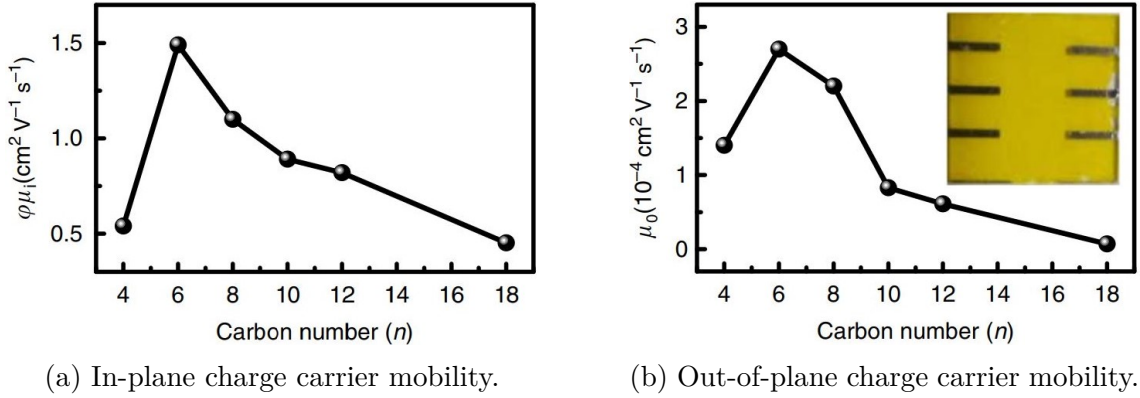


Figure 3.12: Intrinsic mobility of lead-iodide-based 2D hybrid perovskites with a different number of carbon atoms in alkyl ammonium spacers.[155]

In addition, alkyl ammonium-based 2D perovskites show maximum hole mobility at 200 K instead of lowest measured temperature at 100 K. This is a usual behavior in small grain transistors. This can be explained by thermally activated transport mechanism. On the other hand, when temperature gradually increases beyond 200 K, a decrease in mobility with temperature is attributed to an intrinsic transport mechanism dominated by lattice scattering.[156]

Transistors fabricated using precursors synthesized in binary solvents (DMF/DMSO) appear to improve the performance of devices. This is clearly visible in lower carbon cations devices such as (PA)₂SnI₄ and (BA)₂SnI₄. Where these devices did not show transistor behavior in pure DMF as solvent even at different molar concentrations. DMSO is considered a Lewis base and it is known to passivate the grain boundaries.[67] Therefore addition of DMSO can modify the crystallization and reduces anti-site defects. This will result in better film quality and leads to better transistor performance.[157] However, solubility of large carbon chain alkyl ammonium cations in binary (DMF/DMSO) is lower. Due to this longer carbon chain perovskite (Hept)₂SnI₄ is not feasible to synthesize with binary solvent.

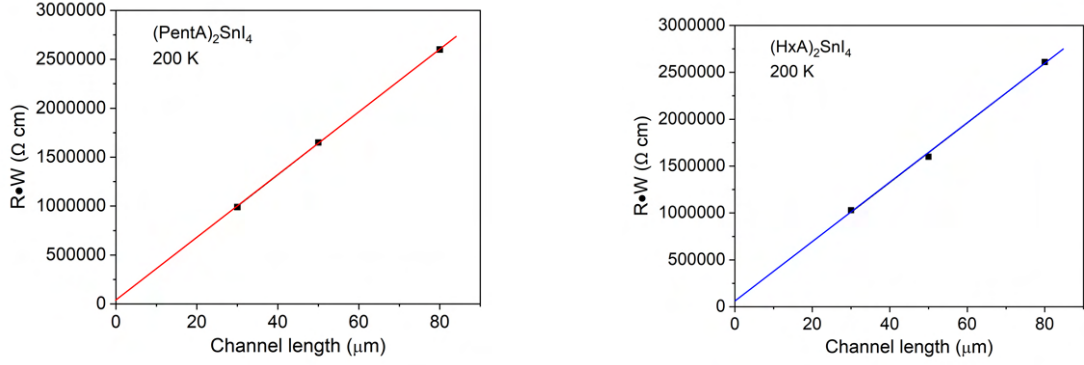
Contact resistance

The metallic contacts are essential parts of field-effect transistors. Understanding the contact resistance between the metal contacts and the active semiconductor layer provides us with useful information to determine the effect on device performance. This can be analyzed using a simple transmission line measurement (TLM) method. Hybrid perovskite field-effect transistors with different gate lengths (80, 50 and 30 μm) are constructed, then output curve is plotted I_{ds} against varying drain-source voltage V_{ds} from 0 V to -60 V at fixed gate voltage $V_g = -60$ V. Only best-performing devices ((PentA)₂SnI₄ and (HxA)₂SnI₄) prepared used recipe C is chosen for the TLM measurements since the lower carbon alkyl chain devices are not functioning properly. Devices are measured at 200 K to obtain better device performance and reduce hysteresis.

Total resistance between any two contacts is given by:[158]

$$R_T = \frac{R_S}{W}L + 2R_C \quad (3.8)$$

Where R_T is total resistance, R_S sheet resistance, L and W are channel width and length respectively.



(a) Contact resistance of (Pent)₂SnI₄, $R_c \cdot W = 22077.5 \Omega \cdot cm$ of (b) Contact resistance of (HxA)₂SnI₄, $R_c \cdot W = 32267 \Omega \cdot cm$

Figure 3.13: The calculated contact resistance of the alkyl ammonium spacers.

When compared to the total resistance of the device the contact resistance is negligible, therefore even though there are differences in contact resistance between (Pent)₂SnI₄ and (HxA)₂SnI₄ perovskite devices, it will not play any significant role in overall effect in the charge carrier mobility.

3.3.2 Hysteresis

Large hysteresis in hybrid perovskites are frequently observed phenomena. Ion migration near grain boundaries, charge carrier trapping at deep energy sites, and surface defects are considered root causes for this behavior.[159] The 2D alkyl ammonium perovskites show small hysteresis in lower temperatures of 100 K. However, when the temperature increases to 200 K, the overall hysteresis becomes considerably large and this remains when future increase to room temperature. The devices prepared using precursor in binary solvent of DMF:DMSO (1:1) show considerably better performance than precursor in pure DMF solvent. This is due to slow crystallization of precursor in binary solvent, which is proven to produce large grain sizes, that makes them less susceptible to ion migration and charge trapping at grain boundaries.

3.3.3 Threshold voltage

Threshold voltage (V_{Th}) refers to the gate voltage where the significant amount of current start to flow between source and drain. Since 2D hybrid tin-iodide based perovskite shows p-channel enhancement mode, usually there would be a significant current flow without any voltage bias in the gate electrode. Here listed the consolidated summary of threshold voltages in alkyl ammonium-based perovskite.

Cation	Solvent	Concentration (M)	Threshold voltage (V)		
			100 K	200 K	295 K
(PA) ₂ SnI ₄	DMF	0.1	-	-	-
(BA) ₂ SnI ₄	DMF	0.1	-	-	-
(PentA) ₂ SnI ₄	DMF	0.1	11.3	2.5	17.3
(HxA) ₂ SnI ₄	DMF	0.1	2.1	7.9	8.7
(HeptA) ₂ SnI ₄	DMF	0.1	1.0	-2.8	38.6
(PA) ₂ SnI ₄	DMF	0.2	-	-	-
(BA) ₂ SnI ₄	DMF	0.2	4.6	1.0	17.3
(PentA) ₂ SnI ₄	DMF	0.2	4.7	11.7	20.6
(HxA) ₂ SnI ₄	DMF	0.2	5.2	9.2	13.5
(HeptA) ₂ SnI ₄	DMF	0.2	12.5	4.8	14.2
(PA) ₂ SnI ₄	DMF:DMSO (1:1)	0.2	7.7	4.0	24.3
(BA) ₂ SnI ₄	DMF:DMSO (1:1)	0.2	7.1	8.4	21.1
(PentA) ₂ SnI ₄	DMF:DMSO (1:1)	0.2	1.0	3.9	24.8
(HxA) ₂ SnI ₄	DMF:DMSO (1:1)	0.2	-13.0	-18.5	26.1
(HxA) ₂ SnI ₄	DMF:DMSO (1:1)	0.2	-	-	-

Table 3.5: Consolidated summary of threshold voltage for alkyl ammonium-based perovskite FETs fabricated with different precursor recipes (A, B & C).

Threshold voltage in alkyl ammonium-based perovskites apparently have temperature dependent relationship. The devices measured at room temperature (295 K) shows higher positive threshold voltages, this can be interrelated to temperature dependent activation energy of charge carriers. However, when it comes to lower temperature regions, could not able to observe a clear trend.

Chapter 4

Conclusion

2D hybrid tin-iodide perovskites with different alkyl ammonium cations as spacers have been successfully formed on a silicon substrate and field-effect transistors with hybrid perovskite thin-film as an active layer were fabricated. A clear correlation between size of the organic cations and optoelectronic, structural, and electrical transport properties was observed. For this, simple linear alkyl ammonium-based cations, starting with 3-carbon chains (propylammonium) to 7-carbon chains (heptan ammonium) were used as the organic spacer. Characterization methods such as XRD and GIWAXS were used to understand the preferred crystal growth orientation. AFM and optical microscopy were used to observe surface morphology and UV-visible spectroscopic analysis for chemical and electronic structure.

Optoelectronic properties and correlation between the size of alkyl ammonium cations in perovskite were evaluated with theoretical and experimental tools. Theoretical studies prove that an increase of exciton binding energy with a longer carbon chain is due to enhancement in dielectric confinement effects. However, this trend could not be observed using analysis of the absorbance spectrum due to the narrow difference in exciton binding energy.

The structural properties of alkyl ammonium perovskites indicate small grain structures in shorter alkyl ammonium perovskites and large grain boundaries in longer alkyl ammonium perovskites. Since grain boundaries act as charge traps in perovskites, this structural change directly affects electrical transport properties. The XRD analysis helps to understand the correlation between the interlayer distance of inorganic layers and the size of organic cations. A gradual increase in interlayer distance is observed as the number of carbon atoms in the alkyl chain increases. Interestingly, GIWAXS analysis provides more information about the correlation between the length of alkyl ammonium chains and the organization of alkyl ammonium molecules in perovskites. The perovskites with shorter alkyl chains are randomly organized, and the longer chains are unidirectionally organized. However, when the length of the alkyl chain further increases, the intensity of diffraction peaks reduces.

The electrical transport properties of 2D hybrid perovskite with different alkyl ammonium cations were studied with the field-effect transistor. The devices prepared using 2D hybrid perovskite active layers were measured at 100 K, 200 K, and room

temperature. Transfer and output curves were plotted to calculate field-effect mobility. Devices measured at 200 K show better carrier mobility than the lower temperature of 100 K. This is similar to the behavior of organic semiconductors, which is explained by the lower activation energy available at 100 K. However, at room temperature, the carrier mobility is much lower than at 100 K. This is related to charge carrier scattering at high temperatures.

In addition, the devices fabricated with precursors prepared using binary solvent DMF: DMSO in a 1: 1 volume ratio show better device performance due to a slower crystallization mechanism that forms larger grains and domains in a polycrystalline film. Devices with lower carbon alkylammonium cations (propylammonium and butylammonium) show extremely poor device performance with less than an order of magnitude of the on-off current ratio. It can be concluded from the surface morphology of these films that large gaps between domains and grains act as charge traps causing poor charge carrier mobility. When it comes to higher carbon number cations, the overall performance of the devices increases significantly with an on-off current ratio of 10^4 . This may also be related to the surface morphology due to tightly assembled grains and domains with no visible voids.

However, devices with the longest carbon chain (Heptanammonium) perovskites show a slight drop in on-off current ratio and carrier mobility. This effect cannot be explained morphologically due to closely packed grains and domains. However, intrinsic factors such as molecular packing influence the mobility in higher carbon number spacers, the presence of gauche defects, and a distortion in the organic chain form potential well, allowing for self-trapping and localization of charge carriers. This observed effect has been demonstrated in 2D lead iodide perovskite. In 2D tin iodide alkyl ammonium perovskites, this can be explained with GIWAXS results of higher carbon number perovskites where we can observe diminishing diffraction peaks. This can be correlated with the molecular level disorder in higher carbon alkyl ammonium perovskites. This effect can be studied with molecular-level simulation to understand the interaction between inorganic and organic layers. This could be a way forward to visualize these effects more clearly.

Bibliography

- [1] Eugene A Katz. Perovskite: name puzzle and german-russian odyssey of discovery. *Helvetica Chimica Acta*, 103(6):e2000061, 2020.
- [2] Giulia Grancini and Mohammad Khaja Nazeeruddin. Dimensional tailoring of hybrid perovskites for photovoltaics. *Nature Reviews Materials*, 4(1):4–22, 2019.
- [3] Jason J Yoo, Gabkyung Seo, Matthew R Chua, Tae Gwan Park, Yongli Lu, Fabian Rotermund, Young-Ki Kim, Chan Su Moon, Nam Joong Jeon, and Juan-Pablo Correa-Baena. Efficient perovskite solar cells via improved carrier management. *Nature*, 590(7847):587–593, 2021.
- [4] Kang Wang, Linrui Jin, Yao Gao, Aihui Liang, Blake P Finkenauer, Wenchao Zhao, Zitang Wei, Chenhui Zhu, Tzung-Fang Guo, and Libai Huang. Lead-free organic-perovskite hybrid quantum wells for highly stable light-emitting diodes. *ACS nano*, 15(4):6316–6325, 2021.
- [5] Kebin Lin, Jun Xing, Li Na Quan, F Pelayo Garcia de Arquer, Xiwen Gong, Jianxun Lu, Liqiang Xie, Weijie Zhao, Di Zhang, and Chuanzhong Yan. Perovskite light-emitting diodes with external quantum efficiency exceeding 20 percent. *Nature*, 562(7726):245–248, 2018.
- [6] Letian Dou, Yang Micheal Yang, Jingbi You, Ziruo Hong, Wei-Hsuan Chang, Gang Li, and Yang Yang. Solution-processed hybrid perovskite photodetectors with high detectivity. *Nature communications*, 5(1):1–6, 2014.
- [7] Wei Tian, Huanping Zhou, and Liang Li. Hybrid organic-inorganic perovskite photodetectors. *Small*, 13(41):1702107, 2017.
- [8] Sjoerd A Veldhuis, Pablo P Boix, Natalia Yantara, Mingjie Li, Tze Chien Sum, Nripan Mathews, and Subodh G Mhaisalkar. Perovskite materials for light-emitting diodes and lasers. *Advanced materials*, 28(32):6804–6834, 2016.
- [9] Haiming Zhu, Yongping Fu, Fei Meng, Xiaoxi Wu, Zizhou Gong, Qi Ding, Martin V Gustafsson, M Tuan Trinh, Song Jin, and XY Zhu. Lead halide perovskite nanowire lasers with low lasing thresholds and high quality factors. *Nature materials*, 14(6):636–642, 2015.
- [10] Toshinori Matsushima, Sunbin Hwang, Atula S. D. Sandanayaka, Chuanjiang Qin, Shinobu Terakawa, Takashi Fujihara, Masayuki Yahiro, and Chihaya Adachi. Solution-processed organic-inorganic perovskite field-effect transistors with high hole mobilities. *Advanced Materials*, 28(46):10275–10281, 2016.

- [11] Huihui Zhu, Ao Liu, Kyu In Shim, Jisu Hong, Jeong Woo Han, and Yong-Young Noh. High-performance and reliable lead-free layered-perovskite transistors. *Advanced Materials*, 32(31):2002717, 2020.
- [12] Aihui Liang, Yao Gao, Reza Asadpour, Zitang Wei, Blake P Finkenauer, Linrui Jin, Jiaqi Yang, Kang Wang, Ke Chen, and Peilin Liao. Ligand-driven grain engineering of high mobility two-dimensional perovskite thin-film transistors. *Journal of the American Chemical Society*, 143(37):15215–15223, 2021.
- [13] Yao Gao, Zitang Wei, Pilsun Yoo, Enzheng Shi, Matthias Zeller, Chenhui Zhu, Peilin Liao, and Letian Dou. Highly stable lead-free perovskite field-effect transistors incorporating linear pi-conjugated organic ligands. *Journal of the American Chemical Society*, 141(39):15577–15585, 2019.
- [14] Victor Moritz Goldschmidt. Die gesetze der krystallochemie. *Naturwissenschaften*, 14(21):477–485, 1926.
- [15] Yongping Fu, Matthew P Hautzinger, Ziyu Luo, Feifan Wang, Dongxu Pan, Michael M Aristov, Ilia A Guzei, Anlian Pan, Xiaoyang Zhu, and Song Jin. Incorporating large a cations into lead iodide perovskite cages: Relaxed goldschmidt tolerance factor and impact on exciton-phonon interaction. *ACS central science*, 5(8):1377–1386, 2019.
- [16] Shuyan Shao, Jian Liu, Giuseppe Portale, Hong-Hua Fang, Graeme R Blake, Gert H ten Brink, L Jan Anton Koster, and Maria Antonietta Loi. Highly reproducible sn-based hybrid perovskite solar cells with 9% efficiency. *Advanced Energy Materials*, 8(4):1702019, 2018.
- [17] Luis Lanzetta, Jose Manuel Marin-Beloqui, Irene Sanchez-Molina, Dong Ding, and Saif A Haque. Two-dimensional organic tin halide perovskites with tunable visible emission and their use in light-emitting devices. *ACS Energy Letters*, 2(7):1662–1668, 2017.
- [18] Cherie R Kagan, David B Mitzi, and Christos D Dimitrakopoulos. Organic-inorganic hybrid materials as semiconducting channels in thin-film field-effect transistors. *Science*, 286(5441):945–947, 1999.
- [19] Yaoguang Rong, Yue Ming, Wenxian Ji, Da Li, Anyi Mei, Yue Hu, and Hongwei Han. Toward industrial-scale production of perovskite solar cells: screen printing, slot-die coating, and emerging techniques. *The Journal of Physical Chemistry Letters*, 9(10):2707–2713, 2018.
- [20] Cristina Roldán-Carmona, Olga Malinkiewicz, Alejandra Soriano, Guillermo Mínguez Espallargas, Ana Garcia, Patrick Reinecke, Thomas Kroyer, M Ibrahim Dar, Mohammad Khaja Nazeeruddin, and Henk J Bolink. Flexible high efficiency perovskite solar cells. *Energy & Environmental Science*, 7(3):994–997, 2014.
- [21] Gustav Rose. Beschreibung einiger neuen mineralien des urals. *Annalen der Physik*, 124(12):551–573, 1839.

- [22] AS Bhalla, Ruyan Guo, and Rustum Roy. The perovskite structure—a review of its role in ceramic science and technology. *Materials research innovations*, 4(1):3–26, 2000.
- [23] Ajay Kumar Jena, Ashish Kulkarni, and Tsutomu Miyasaka. Halide perovskite photovoltaics: background, status, and future prospects. *Chemical reviews*, 119(5):3036–3103, 2019.
- [24] Sarat Kumar Sahoo, Balamurugan Manoharan, and Narendiran Sivakumar. Introduction: Why perovskite and perovskite solar cells? In *Perovskite Photovoltaics*, pages 1–24. Elsevier, 2018.
- [25] Anurag Krishna, Sébastien Gottis, Mohammad Khaja Nazeeruddin, and Frédéric Sauvage. Mixed dimensional 2d/3d hybrid perovskite absorbers: the future of perovskite solar cells? *Advanced Functional Materials*, 29(8):1806482, 2019.
- [26] Gregor Kieslich, Shijing Sun, and Anthony K Cheetham. Solid-state principles applied to organic–inorganic perovskites: new tricks for an old dog. *Chemical Science*, 5(12):4712–4715, 2014.
- [27] Giulia Grancini and Mohammad Khaja Nazeeruddin. Dimensional tailoring of hybrid perovskites for photovoltaics. *Nature Reviews Materials*, 4(1):4–22, 2019.
- [28] Carmen Ortiz-Cervantes, Paulina Carmona-Monroy, and Diego Solis-Ibarra. Two-dimensional halide perovskites in solar cells: 2d or not 2d? *ChemSusChem*, 12(8):1560–1575, 2019.
- [29] Hsinhan Tsai, Wanyi Nie, Jean-Christophe Blancon, Constantinos C Stoumpos, Reza Asadpour, Boris Harutyunyan, Amanda J Neukirch, Rafael Verduzco, Jared J Crochet, and Sergei Tretiak. High-efficiency two-dimensional ruddlesden-popper perovskite solar cells. *Nature*, 536(7616):312–316, 2016.
- [30] Lingling Mao, Weijun Ke, Laurent Pedesseau, Yilei Wu, Claudine Katan, Jacky Even, Michael R Wasielewski, Constantinos C Stoumpos, and Mercouri G Kanatzidis. Hybrid dion-jacobson 2d lead iodide perovskites. *Journal of the American Chemical Society*, 140(10):3775–3783, 2018.
- [31] Shuai Zhao, Chunfeng Lan, Huanhuan Li, Chu Zhang, and Tingli Ma. Aurivillius halide perovskite: a new family of two-dimensional materials for optoelectronic applications. *The Journal of Physical Chemistry C*, 124(3):1788–1793, 2019.
- [32] Chan Myae Myae Soe, Constantinos C Stoumpos, Mikael Kepenekian, Boubacar Traore, Hsinhan Tsai, Wanyi Nie, Binghao Wang, Claudine Katan, Ram Seshadri, and Aditya D Mohite. New type of 2d perovskites with alternating cations in the interlayer space, $(c(\text{nh}_2)_3)(\text{ch}_3\text{nh}_3)_n\text{pb}_n\text{i}_{3n+1}$: Structure, properties, and photovoltaic performance. *Journal of the American Chemical Society*, 139(45):16297–16309, 2017.

- [33] Meng Wang, Qunliang Song, and Sam Zhang. 2d organic-inorganic hybrid perovskite light-absorbing layer in solar cells. *Solar Cells: Theory, Materials and Recent Advances*, page 253, 2021.
- [34] Teruya Ishihara, Jun Takahashi, and Takenari Goto. Exciton state in two-dimensional perovskite semiconductor (c10h21nh3) 2pbI4. *Solid state communications*, 69(9):933–936, 1989.
- [35] DB Mitzi, S Wang, CA Feild, CA Chess, and AM Guloy. Conducting layered organic-inorganic halides containing < 110 >-oriented perovskite sheets. *Science*, 267(5203):1473–1476, 1995.
- [36] Constantinos C Stoumpos, Duyen H Cao, Daniel J Clark, Joshua Young, James M Rondinelli, Joon I Jang, Joseph T Hupp, and Mercuri G Kanatzidis. Ruddlesden-popper hybrid lead iodide perovskite 2d homologous semiconductors. *Chemistry of Materials*, 28(8):2852–2867, 2016.
- [37] BV Beznosikov and KS Aleksandrov. Perovskite-like crystals of the ruddlesden-popper series. *Crystallography Reports*, 45(5):792–798, 2000.
- [38] J Calabrese, NL Jones, RL Harlow, N Herron, DL Thorn, and Y Wang. Preparation and characterization of layered lead halide compounds. *Journal of the American Chemical Society*, 113(6):2328–2330, 1991.
- [39] Sajjad Ahmad, Ping Fu, Shuwen Yu, Qing Yang, Xuan Liu, Xuchao Wang, Xiuli Wang, Xin Guo, and Can Li. Dion-jacobson phase 2d layered perovskites for solar cells with ultrahigh stability. *Joule*, 3(3):794–806, 2019.
- [40] Haotian Wu, Xiaomei Lian, Shuoxun Tian, Yingzhu Zhang, Minchao Qin, Yanyan Zhang, Fuyi Wang, Xinhui Lu, Gang Wu, and Hongzheng Chen. Additive-assisted hot-casting free fabrication of dion-jacobson 2d perovskite solar cell with efficiency beyond 16%. *Solar RRL*, 4(7):2000087, 2020.
- [41] Haotian Wu, Xiaomei Lian, Jun Li, Yingzhu Zhang, Guanqing Zhou, Xinbo Wen, Zengqi Xie, Haiming Zhu, Gang Wu, and Hongzheng Chen. Merged interface construction toward ultra-low v oc loss in inverted two-dimensional dion-jacobson perovskite solar cells with efficiency over 18%. *Journal of Materials Chemistry A*, 9(21):12566–12573, 2021.
- [42] Pengwei Li, Chao Liang, Xiao-Long Liu, Fengyu Li, Yiqiang Zhang, Xiao-Tao Liu, Hao Gu, Xiaotian Hu, Guichuan Xing, and Xutang Tao. Low-dimensional perovskites with diammonium and monoammonium alternant cations for high-performance photovoltaics. *Advanced Materials*, 31(35):1901966, 2019.
- [43] Yalan Zhang, Peijun Wang, Ming-Chun Tang, Dounya Barrit, Weijun Ke, Junxue Liu, Tao Luo, Yucheng Liu, Tianqi Niu, and Detlef-M Smilgies. Dynamical transformation of two-dimensional perovskites with alternating cations in the interlayer space for high-performance photovoltaics. *Journal of the American Chemical Society*, 141(6):2684–2694, 2019.
- [44] Caleb C Boyd, Rongrong Cheacharoen, Tomas Leijtens, and Michael D McGehee. Understanding degradation mechanisms and improving stability of perovskite photovoltaics. *Chemical reviews*, 119(5):3418–3451, 2018.

- [45] Aurelien MA Leguy, Yinghong Hu, Mariano Campoy-Quiles, M Isabel Alonso, Oliver J Weber, Pooya Azarhoosh, Mark Van Schilfgaarde, Mark T Weller, Thomas Bein, and Jenny Nelson. Reversible hydration of $\text{CH}_3\text{NH}_3\text{PbI}_3$ in films, single crystals, and solar cells. *Chemistry of Materials*, 27(9):3397–3407, 2015.
- [46] Jeffrey A Christians, Pierre A Miranda Herrera, and Prashant V Kamat. Transformation of the excited state and photovoltaic efficiency of $\text{CH}_3\text{NH}_3\text{PbI}_3$ perovskite upon controlled exposure to humidified air. *Journal of the American Chemical Society*, 137(4):1530–1538, 2015.
- [47] Jarvist M Frost, Keith T Butler, Federico Brivio, Christopher H Hendon, Mark Van Schilfgaarde, and Aron Walsh. Atomistic origins of high-performance in hybrid halide perovskite solar cells. *Nano letters*, 14(5):2584–2590, 2014.
- [48] Wei-Chun Lin, Hsun-Yun Chang, Kevin Abbasi, Jing-Jong Shyue, and Clemens Burda. 3d in situ tof-sims imaging of perovskite films under controlled humidity environmental conditions. *Advanced Materials Interfaces*, 4(2):1600673, 2017.
- [49] Jinli Yang, Braden D Siempelkamp, Dianyi Liu, and Timothy L Kelly. Investigation of $\text{CH}_3\text{NH}_3\text{PbI}_3$ degradation rates and mechanisms in controlled humidity environments using in situ techniques. *ACS nano*, 9(2):1955–1963, 2015.
- [50] Jae Sung Yun, Jincheol Kim, Trevor Young, Robert J Patterson, Dohyung Kim, Jan Seidel, Sean Lim, Martin A Green, Shujuan Huang, and Anita Hobbaillie. Humidity-induced degradation via grain boundaries of $\text{HC}(\text{NH}_2)_2\text{PbI}_3$ planar perovskite solar cells. *Advanced Functional Materials*, 28(11):1705363, 2018.
- [51] Namyoun Ahn, Kwisung Kwak, Min Seok Jang, Heetae Yoon, Byung Yang Lee, Jong-Kwon Lee, Peter V Pikhitsa, Junseop Byun, and Mansoo Choi. Trapped charge-driven degradation of perovskite solar cells. *Nature communications*, 7(1):1–9, 2016.
- [52] Nicholas Aristidou, Irene Sanchez-Molina, Thana Chotchuangchutchaval, Michael Brown, Luis Martinez, Thomas Rath, and Saif A Haque. The role of oxygen in the degradation of methylammonium lead trihalide perovskite photoactive layers. *Angewandte Chemie*, 127(28):8326–8330, 2015.
- [53] David B Mitzi, CA Feild, WTA Harrison, and AM Guloy. Conducting tin halides with a layered organic-based perovskite structure. *Nature*, 369(6480):467–469, 1994.
- [54] Luis Lanzetta, Thomas Webb, Nouridine Zibouche, Xinxing Liang, Dong Ding, Ganghong Min, Robert JE Westbrook, Benedetta Gaggio, Thomas J Macdonald, M Saiful Islam, et al. Degradation mechanism of hybrid tin-based perovskite solar cells and the critical role of tin (iv) iodide. *Nature communications*, 12(1):1–11, 2021.
- [55] Gee Yeong Kim, Alessandro Senocrate, Tae-Youl Yang, Giuliano Gregori, Michael Gratzel, and Joachim Maier. Large tunable photoeffect on ion conduction in halide perovskites and implications for photodecomposition. *Nature materials*, 17(5):445–449, 2018.

- [56] Yongbo Yuan and Jinsong Huang. Ion migration in organometal trihalide perovskite and its impact on photovoltaic efficiency and stability. *Accounts of chemical research*, 49(2):286–293, 2016.
- [57] Junichiro Mizusaki, Kimiyasu Arai, and Kazuo Fueki. Ionic conduction of the perovskite-type halides. *Solid State Ionics*, 11(3):203–211, 1983.
- [58] Yongbo Yuan, Qi Wang, Yuchuan Shao, Haidong Lu, Tao Li, Alexei Gruverman, and Jinsong Huang. Electric-field-driven reversible conversion between methylammonium lead triiodide perovskites and lead iodide at elevated temperatures. *Advanced Energy Materials*, 6(2):1501803, 2016.
- [59] Jon M Azpiroz, Edoardo Mosconi, Juan Bisquert, and Filippo De Angelis. Defect migration in methylammonium lead iodide and its role in perovskite solar cell operation. *Energy & Environmental Science*, 8(7):2118–2127, 2015.
- [60] Jongseob Kim, Sung-Hoon Lee, Jung Hoon Lee, and Ki-Ha Hong. The role of intrinsic defects in methylammonium lead iodide perovskite. *The journal of physical chemistry letters*, 5(8):1312–1317, 2014.
- [61] Yuchuan Shao, Yanjun Fang, Tao Li, Qi Wang, Qingfeng Dong, Yehao Deng, Yongbo Yuan, Haotong Wei, Meiyu Wang, Alexei Gruverman, et al. Grain boundary dominated ion migration in polycrystalline organic–inorganic halide perovskite films. *Energy & Environmental Science*, 9(5):1752–1759, 2016.
- [62] Yuchen Zhou, Nikhil Tiwale, Yifan Yin, Ashwanth Subramanian, Miriam H Rafailovich, and Chang-Yong Nam. Effects of polymer grain boundary passivation on organic–inorganic hybrid perovskite field-effect transistors. *Applied Physics Letters*, 119(18):183303, 2021.
- [63] Teng Zhang, Chen Hu, and Shihe Yang. Ion migration: A “double-edged sword” for halide-perovskite-based electronic devices. *Small Methods*, 4(5):1900552, 2020.
- [64] Yun Lin, Yang Bai, Yanjun Fang, Qi Wang, Yehao Deng, and Jinsong Huang. Suppressed ion migration in low-dimensional perovskites. *ACS Energy Letters*, 2(7):1571–1572, 2017.
- [65] Xun Xiao, Jun Dai, Yanjun Fang, Jingjing Zhao, Xiaopeng Zheng, Shi Tang, Peter Neil Rudd, Xiao Cheng Zeng, and Jinsong Huang. Suppressed ion migration along the in-plane direction in layered perovskites. *ACS Energy Letters*, 3(3):684–688, 2018.
- [66] Qingxia Fu, Xianglan Tang, Bin Huang, Ting Hu, Licheng Tan, Lie Chen, and Yiwang Chen. Recent progress on the long-term stability of perovskite solar cells. *Advanced Science*, 5(5):1700387, 2018.
- [67] Tianqi Niu, Jing Lu, Rahim Munir, Jianbo Li, Dounya Barrit, Xu Zhang, Hanlin Hu, Zhou Yang, Aram Amassian, Kui Zhao, et al. Stable high-performance perovskite solar cells via grain boundary passivation. *Advanced Materials*, 30(16):1706576, 2018.

- [68] Kai Wang, Jiang Liu, Jun Yin, Erkan Aydin, George T Harrison, Wenzhu Liu, Shanyong Chen, Omar F Mohammed, and Stefaan De Wolf. Defect passivation in perovskite solar cells by cyano-based π -conjugated molecules for improved performance and stability. *Advanced Functional Materials*, 30(35):2002861, 2020.
- [69] Tae-Hee Han, Jin-Wook Lee, Chungseok Choi, Shaun Tan, Changsoo Lee, Yepin Zhao, Zhenghong Dai, Nicholas De Marco, Sung-Joon Lee, Sang-Hoon Bae, et al. Perovskite-polymer composite cross-linker approach for highly-stable and efficient perovskite solar cells. *Nature communications*, 10(1):1–10, 2019.
- [70] Gengling Liu, Cong Liu, Zhuojia Lin, Jia Yang, Zengqi Huang, Licheng Tan, and Yiwang Chen. Regulated crystallization of efficient and stable tin-based perovskite solar cells via a self-sealing polymer. *ACS Applied Materials & Interfaces*, 12(12):14049–14056, 2020.
- [71] Lili Gao, Ioannis Spanopoulos, Weijun Ke, Sheng Huang, Ido Hadar, Lin Chen, Xiaolei Li, Guanjun Yang, and Mercouri G Kanatzidis. Improved environmental stability and solar cell efficiency of (ma, fa) pbi3 perovskite using a wide-band-gap 1d thiazolium lead iodide capping layer strategy. *ACS Energy Letters*, 4(7):1763–1769, 2019.
- [72] Ning Yang, Cheng Zhu, Yihua Chen, Huachao Zai, Chenyue Wang, Xi Wang, Hao Wang, Sai Ma, Ziyang Gao, Xueyun Wang, et al. An in situ cross-linked 1d/3d perovskite heterostructure improves the stability of hybrid perovskite solar cells for over 3000 h operation. *Energy & Environmental Science*, 13(11):4344–4352, 2020.
- [73] Tae-Hee Han, Jin-Wook Lee, Yung Ji Choi, Chungseok Choi, Shaun Tan, Sung-Joon Lee, Yepin Zhao, Yu Huang, Dongho Kim, and Yang Yang. Surface-2d/bulk-3d heterophased perovskite nanograins for long-term-stable light-emitting diodes. *Advanced Materials*, 32(1):1905674, 2020.
- [74] Peng Zhang, Jiang Wu, Yafei Wang, Hojjatollah Sarvari, Detao Liu, Zhi David Chen, and Shibin Li. Enhanced efficiency and environmental stability of planar perovskite solar cells by suppressing photocatalytic decomposition. *Journal of Materials Chemistry A*, 5(33):17368–17378, 2017.
- [75] Nicholas Rolston, Kevin A Bush, Adam D Printz, Aryeh Gold-Parker, Yichuan Ding, Michael F Toney, Michael D McGehee, and Reinhold H Dauskardt. Engineering stress in perovskite solar cells to improve stability. *Advanced Energy Materials*, 8(29):1802139, 2018.
- [76] Hongtao Lai, Bin Kan, Tingting Liu, Nan Zheng, Zengqi Xie, Tong Zhou, Xiangjian Wan, Xiaodan Zhang, Yongsheng Liu, and Yongsheng Chen. Two-dimensional ruddlesden–popper perovskite with nanorod-like morphology for solar cells with efficiency exceeding 15%. *Journal of the American Chemical Society*, 140(37):11639–11646, 2018.
- [77] Kaibo Zheng and Tonu Pullerits. Two dimensions are better for perovskites, 2019.

- [78] J-C Blancon, Hsinhan Tsai, Wanyi Nie, Costas C Stoumpos, Laurent Pedesseau, Claudine Katan, Mikael Kepenekian, Chan Myae Myae Soe, Kanatassen Appavoo, Matthew Y Sfeir, et al. Extremely efficient internal exciton dissociation through edge states in layered 2d perovskites. *Science*, 355(6331):1288–1292, 2017.
- [79] Xuejie Zhu, Zhuo Xu, Shengnan Zuo, Jiangshan Feng, Ziyu Wang, Xiaorong Zhang, Kui Zhao, Jian Zhang, Hairui Liu, Shashank Priya, et al. Vapor-fumigation for record efficiency two-dimensional perovskite solar cells with superior stability. *Energy & Environmental Science*, 11(12):3349–3357, 2018.
- [80] Xiaoming Zhao, Tianran Liu, Alan B Kaplan, Chao Yao, and Yueh-Lin Loo. Accessing highly oriented two-dimensional perovskite films via solvent-vapor annealing for efficient and stable solar cells. *Nano Letters*, 20(12):8880–8889, 2020.
- [81] Yani Chen, Yong Sun, Jiajun Peng, Junhui Tang, Kaibo Zheng, and Ziqi Liang. 2d ruddlesden–popper perovskites for optoelectronics. *Advanced Materials*, 30(2):1703487, 2018.
- [82] Fei Zhang, Dong Hoe Kim, Haipeng Lu, Ji-Sang Park, Bryon W Larson, Jun Hu, Liguao Gao, Chuanxiao Xiao, Obadiah G Reid, Xihan Chen, et al. Enhanced charge transport in 2d perovskites via fluorination of organic cation. *Journal of the American Chemical Society*, 141(14):5972–5979, 2019.
- [83] Weifei Fu, Hongbin Liu, Xueliang Shi, Lijian Zuo, Xiaosong Li, and Alex K-Y Jen. Tailoring the functionality of organic spacer cations for efficient and stable quasi-2d perovskite solar cells. *Advanced Functional Materials*, 29(25):1900221, 2019.
- [84] Zhiping Wang, Qianqian Lin, Francis P Chmiel, Nobuya Sakai, Laura M Herz, and Henry J Snaith. Efficient ambient-air-stable solar cells with 2d–3d heterostructured butylammonium-caesium-formamidinium lead halide perovskites. *Nature Energy*, 2(9):1–10, 2017.
- [85] Yanping Lv, Xuedan Song, Yanfeng Yin, Yulin Feng, Hongru Ma, Ce Hao, Shengye Jin, and Yantao Shi. Hexylammonium iodide derived two-dimensional perovskite as interfacial passivation layer in efficient two-dimensional/three-dimensional perovskite solar cells. *ACS Applied Materials & Interfaces*, 12(1):698–705, 2019.
- [86] Yukari Takahashi, Rena Obara, Kohei Nakagawa, Masayuki Nakano, Jun-ya Tokita, and Tamotsu Inabe. Tunable charge transport in soluble organic–inorganic hybrid semiconductors. *Chemistry of Materials*, 19(25):6312–6316, 2007.
- [87] Lingling Mao, Hsinhan Tsai, Wanyi Nie, Lin Ma, Jino Im, Constantinos C Stoumpos, Christos D Malliakas, Feng Hao, Michael R Wasielewski, Aditya D Mohite, et al. Role of organic counterion in lead-and tin-based two-dimensional semiconducting iodide perovskites and application in planar solar cells. *Chemistry of Materials*, 28(21):7781–7792, 2016.

- [88] Zhengtao Xu, David B Mitzi, Christos D Dimitrakopoulos, and Karen R Maxcy. Semiconducting perovskites $(2\text{-xc}_6\text{h}_4\text{c}_2\text{h}_4\text{nh}_3)_2\text{sn}_2\text{i}_4$ ($x = \text{f, cl, br}$): steric interaction between the organic and inorganic layers. *Inorganic chemistry*, 42(6):2031–2039, 2003.
- [89] David B Mitzi, Christos D Dimitrakopoulos, and Laura L Kosbar. Structurally tailored organic-inorganic perovskites: optical properties and solution-processed channel materials for thin-film transistors. *Chemistry of materials*, 13(10):3728–3740, 2001.
- [90] Iwan Zimmermann, Sadig Aghazada, and Mohammad Khaja Nazeeruddin. Lead and htm free stable two-dimensional tin perovskites with suitable band gap for solar cell applications. *Angewandte Chemie*, 131(4):1084–1088, 2019.
- [91] Xunshan Liu, Songjie Chen, Jürg Hauser, Vladimir Laukhin, Silvio Decurtins, Ulrich Aschauer, and Shi-Xia Liu. Low-dimensional tin (ii) iodide perovskite structures templated by an aromatic heterocyclic cation. *Crystal growth & design*, 16(9):5230–5237, 2016.
- [92] Iwan Zimmermann, Tony D Keene, Jürg Hauser, Silvio Decurtins, and S-X Liu. Crystal structures of isotypic poly [bis (benzimidazolium)[tetra- μ -iodido-stannate (ii)] and poly [bis (5, 6-difluorobenzimidazolium)[tetra- μ -iodido-stannate (ii)]]. *Acta Crystallographica Section E: Structure Reports Online*, 70(10):178–182, 2014.
- [93] Xue-Nan Li, Peng-Fei Li, Zhong-Xia Wang, Ping-Ping Shi, Yuan-Yuan Tang, and Heng-Yun Ye. The structural phase transition in a hybrid layered perovskite: $[\text{c}_7\text{h}_{16}\text{n}]_2[\text{sn}_2\text{i}_4]$. *Polyhedron*, 129:92–96, 2017.
- [94] Leonardo Apostolico, Gabriele Kociok-Köhn, Kieran C Molloy, Christopher S Blackman, Claire J Carmalt, and Ivan P Parkin. The reaction of tin (iv) iodide with phosphines: formation of new halotin anions. *Dalton Transactions*, (47):10486–10494, 2009.
- [95] Michael Daub, Christoph Haber, and Harald Hillebrecht. Synthesis, crystal structures, optical properties, and phase transitions of the layered guanidinium-based hybrid perovskites $[\text{c}(\text{nh}_2)_3]_2\text{m}_2\text{i}_4$; $m = \text{sn, pb}$. *European Journal of Inorganic Chemistry*, 2017(7):1120–1126, 2017.
- [96] Zhengtao Xu and David B Mitzi. $[\text{ch}_3(\text{ch}_2)_{11}\text{nh}_3]_2\text{sn}_2\text{i}_4$: A hybrid semiconductor with moo_3 -type tin (ii) iodide layers. *Inorganic chemistry*, 42(21):6589–6591, 2003.
- [97] Vaibhav V Nawale, Tariq Sheikh, and Angshuman Nag. Dual excitonic emission in hybrid 2d layered tin iodide perovskites. *The Journal of Physical Chemistry C*, 124(38):21129–21136, 2020.
- [98] Robin J Francis, P Shiv Halasyamani, and Dermot O’Hare. The first organically templated layered uranium (iv) fluorides: $(\text{h}_3\text{n}(\text{ch}_2)_3\text{nh}_3)_2\text{u}_2\text{f}_{10} \cdot 2\text{h}_2\text{o}$, $(\text{h}_3\text{n}(\text{ch}_2)_4\text{nh}_3)_2\text{u}_2\text{f}_{10} \cdot 3\text{h}_2\text{o}$, and $(\text{h}_3\text{n}(\text{ch}_2)_6\text{nh}_3)_2\text{u}_2\text{f}_{10} \cdot 2\text{h}_2\text{o}$. *Angewandte Chemie International Edition*, 37(16):2214–2217, 1998.

- [99] Cheng-Min Tsai, Yu-Pei Lin, Murali Krishna Pola, Sudhakar Narra, Efat Jokar, Yaw-Wen Yang, and Eric Wei-Guang Diao. Control of crystal structures and optical properties with hybrid formamidinium and 2-hydroxyethylammonium cations for mesoscopic carbon-electrode tin-based perovskite solar cells. *ACS Energy Letters*, 3(9):2077–2085, 2018.
- [100] William Shockley. A unipolar" field-effect" transistor. *Proceedings of the IRE*, 40(11):1365–1376, 1952.
- [101] Tingjun Wu, Wojciech Pisula, Mohd Yusoff Abd Rashid, and Peng Gao. Application of perovskite-structured materials in field-effect transistors. *Advanced Electronic Materials*, 5(12):1900444, 2019.
- [102] Po-Wei Liang, Chien-Yi Liao, Chu-Chen Chueh, Fan Zuo, Spencer T Williams, Xu-Kai Xin, Jiangjen Lin, and Alex K-Y Jen. Additive enhanced crystallization of solution-processed perovskite for highly efficient planar-heterojunction solar cells. *Advanced materials*, 26(22):3748–3754, 2014.
- [103] Fabian Paulus, Colin Tyznik, Oana D Jurchescu, and Yana Vaynzof. Switched-on: Progress, challenges, and opportunities in metal halide perovskite transistors. *Advanced Functional Materials*, 31(29):2101029, 2021.
- [104] Toshinori Matsushima, Matthew R Leyden, Takashi Fujihara, Chuanjiang Qin, Atula SD Sandanayaka, and Chihaya Adachi. Large metal halide perovskite crystals for field-effect transistor applications. *Applied Physics Letters*, 115(12):120601, 2019.
- [105] Jin Hyuck Heo, Sang Hyuk Im, Jun Hong Noh, Tarak N Mandal, Choong-Sun Lim, Jeong Ah Chang, Yong Hui Lee, Hi-jung Kim, Arpita Sarkar, Md K Nazeeruddin, et al. Efficient inorganic–organic hybrid heterojunction solar cells containing perovskite compound and polymeric hole conductors. *Nature photonics*, 7(6):486–491, 2013.
- [106] John G Labram, Douglas H Fabini, Erin E Perry, Anna J Lehner, Hengbin Wang, Anne M Glaudell, Guang Wu, Hayden Evans, David Buck, Robert Cotta, et al. Temperature-dependent polarization in field-effect transport and photovoltaic measurements of methylammonium lead iodide. *The Journal of Physical Chemistry Letters*, 6(18):3565–3571, 2015.
- [107] Satyaprasad P Senanayak, Bingyan Yang, Tudor H Thomas, Nadja Giesbrecht, Wenchao Huang, Eliot Gann, Bhaskaran Nair, Karl Goedel, Suchi Guha, Xavier Moya, et al. Understanding charge transport in lead iodide perovskite thin-film field-effect transistors. *Science advances*, 3(1):e1601935, 2017.
- [108] Huihui Zhu, Ao Liu, Kyu In Shim, Haksoo Jung, Taoyu Zou, Youjin Reo, Hyunjun Kim, Jeong Woo Han, Yimu Chen, Hye Yong Chu, et al. High-performance hysteresis-free perovskite transistors through anion engineering. *Nature communications*, 13(1):1–8, 2022.

- [109] Satyaprasad P Senanayak, Mojtaba Abdi-Jalebi, Varun S Kamboj, Remington Carey, Ravichandran Shivanna, Tian Tian, Guillaume Schweicher, Junzhan Wang, Nadja Giesbrecht, Daniele Di Nuzzo, et al. A general approach for hysteresis-free, operationally stable metal halide perovskite field-effect transistors. *Science advances*, 6(15):eaaz4948, 2020.
- [110] Yao Gao, Zitang Wei, Pilsun Yoo, Enzheng Shi, Matthias Zeller, Chenhui Zhu, Peilin Liao, and Letian Dou. Highly stable lead-free perovskite field-effect transistors incorporating linear π -conjugated organic ligands. *Journal of the American Chemical Society*, 141(39):15577–15585, 2019.
- [111] Xiao-Jian She, Chen Chen, Giorgio Divitini, Baodan Zhao, Yang Li, Junzhan Wang, Jordi Ferrer Orri, Linsong Cui, Weidong Xu, Jun Peng, et al. A solvent-based surface cleaning and passivation technique for suppressing ionic defects in high-mobility perovskite field-effect transistors. *Nature Electronics*, 3(11):694–703, 2020.
- [112] Weili Yu, Feng Li, Liyang Yu, Muhammad R Niazi, Yuting Zou, Daniel Corzo, Aniruddha Basu, Chun Ma, Sukumar Dey, Max L Tietze, et al. Single crystal hybrid perovskite field-effect transistors. *Nature communications*, 9(1):1–10, 2018.
- [113] R Kind. Structural phase transitions in perovskite layer structures. *Ferroelectrics*, 24(1):81–88, 1980.
- [114] Yuhang Liu, Seckin Akin, Alexander Hinderhofer, Felix T Eickemeyer, Hongwei Zhu, Ji-Youn Seo, Jiahuan Zhang, Frank Schreiber, Hong Zhang, Shaik M Zakeeruddin, et al. Stabilization of highly efficient and stable phase-pure fapbi3 perovskite solar cells by molecularly tailored 2d-overlayers. *Angewandte Chemie International Edition*, 59(36):15688–15694, 2020.
- [115] N,n-dimethylformamide.
- [116] Dimethyl sulfoxide.
- [117] Youngjun Park and Jang-Sik Lee. Controlling the grain size of dion–jacobson-phase two-dimensional layered perovskite for memory application. *ACS Applied Materials & Interfaces*, 2022.
- [118] Junke Jiang, José Manuel Vicent-Luna, and Shuxia Tao. The role of solvents in the formation of methylammonium lead triiodide perovskite. *Journal of Energy Chemistry*, 68:393–400, 2022.
- [119] Jianjun Zhang, Liuyang Zhang, Xiaohe Li, Xinyi Zhu, Jiaguo Yu, and Ke Fan. Binary solvent engineering for high-performance two-dimensional perovskite solar cells. *ACS Sustainable Chemistry & Engineering*, 7(3):3487–3495, 2019.
- [120] Kai Wang, Congcong Wu, Dong Yang, Yuanyuan Jiang, and Shashank Priya. Quasi-two-dimensional halide perovskite single crystal photodetector. *ACS nano*, 12(5):4919–4929, 2018.
- [121] George F Harrington and José Santiso. Back-to-basics tutorial: X-ray diffraction of thin films. *Journal of Electroceramics*, pages 1–23, 2021.

- [122] William Henry Bragg and William Lawrence Bragg. The reflection of x-rays by crystals. *Proceedings of the Royal Society of London. Series A, Containing Papers of a Mathematical and Physical Character*, 88(605):428–438, 1913.
- [123] Asif Mahmood and Jin-Liang Wang. A review of grazing incidence small-and wide-angle x-ray scattering techniques for exploring the film morphology of organic solar cells. *Solar RRL*, 4(10):2000337, 2020.
- [124] Chenyue Wang, Chuantian Zuo, Qi Chen, Liming Ding, et al. Giwaxs: A powerful tool for perovskite photovoltaics. *Journal of Semiconductors*, 42(6):060201, 2021.
- [125] Minchao Qin, Pok Fung Chan, and Xinhui Lu. A systematic review of metal halide perovskite crystallization and film formation mechanism unveiled by in situ giwaxs. *Advanced Materials*, 33(51):2105290, 2021.
- [126] Jonathan Rivnay, Stefan CB Mannsfeld, Chad E Miller, Alberto Salleo, and Michael F Toney. Quantitative determination of organic semiconductor microstructure from the molecular to device scale. *Chemical reviews*, 112(10):5488–5519, 2012.
- [127] Heinz-Helmut Perkampus. *UV-VIS Spectroscopy and its Applications*. Springer Science & Business Media, 2013.
- [128] Weiyin Gao, Changshun Chen, Chenxin Ran, Hao Zheng, He Dong, Yingdong Xia, Yonghua Chen, and Wei Huang. A-site cation engineering of metal halide perovskites: Version 3.0 of efficient tin-based lead-free perovskite solar cells. *Advanced Functional Materials*, 30(34):2000794, 2020.
- [129] Qiang Wang, Xiao-Dan Liu, Yun-Hang Qiu, Kai Chen, Li Zhou, and Qu-Quan Wang. Quantum confinement effect and exciton binding energy of layered perovskite nanoplatelets. *AIP Advances*, 8(2):025108, 2018.
- [130] Tianju Zhang, Chaocheng Zhou, Xuezhen Feng, Ningning Dong, Hong Chen, Xianfeng Chen, Long Zhang, Jia Lin, and Jun Wang. Regulation of the luminescence mechanism of two-dimensional tin halide perovskites. *Nature Communications*, 13(1):1–11, 2022.
- [131] Jai Singh and Richard T Williams. *Excitonic and photonic processes in materials*. Springer, 2015.
- [132] Robert Seiple Knox. Theory of excitons. *Solid State Phys.*, 5, 1963.
- [133] Rayan Chakraborty and Angshuman Nag. Dielectric confinement for designing compositions and optoelectronic properties of 2d layered hybrid perovskites. *Physical Chemistry Chemical Physics*, 23(1):82–93, 2021.
- [134] Mark Fox. *Optical properties of solids*, 2002.
- [135] XL Yang, SH Guo, FT Chan, KW Wong, and WY Ching. Analytic solution of a two-dimensional hydrogen atom. i. nonrelativistic theory. *Physical Review A*, 43(3):1186, 1991.

- [136] Egor A Muljarov, SG Tikhodeev, NA Gippius, and Teruya Ishihara. Excitons in self-organized semiconductor/insulator superlattices: Pbi-based perovskite compounds. *Physical Review B*, 51(20):14370, 1995.
- [137] Natalia S Rytova. Screened potential of a point charge in a thin film. *Moscow University Physics Bulletin* 3, 30, 1967.
- [138] LV Keldysh. Coulomb interaction in thin semiconductor and semimetal films. *Soviet Journal of Experimental and Theoretical Physics Letters*, 29:658, 1979.
- [139] Omer Yaffe, Alexey Chernikov, Zachariah M Norman, Yu Zhong, Ajanthkrishna Velauthapillai, Arend Van Der Zande, Jonathan S Owen, and Tony F Heinz. Excitons in ultrathin organic-inorganic perovskite crystals. *Physical Review B*, 92(4):045414, 2015.
- [140] Kenichiro Tanaka, Takayuki Takahashi, Takashi Kondo, Tsutomu Umebayashi, Keisuke Asai, and Kazuhiro Ema. Image charge effect on two-dimensional excitons in an inorganic-organic quantum-well crystal. *Physical Review B*, 71(4):045312, 2005.
- [141] M Hirasawa, Teruya Ishihara, T Goto, K3 Uchida, and N Miura. Magnetoabsorption of the lowest exciton in perovskite-type compound (ch₃nh₃) pbi₃. *Physica B: Condensed Matter*, 201:427–430, 1994.
- [142] Bin Cheng, Ting-You Li, Partha Maity, Pai-Chun Wei, Dennis Nordlund, Kang-Ting Ho, Der-Hsien Lien, Chun-Ho Lin, Ru-Ze Liang, Xiaohe Miao, et al. Extremely reduced dielectric confinement in two-dimensional hybrid perovskites with large polar organics. *Communications Physics*, 1(1):1–8, 2018.
- [143] Ch. Wohlfahrt. 2 pure liquids: Data: Datasheet from landolt-börnstein - group iv physical chemistry · volume 6: “static dielectric constants of pure liquids and binary liquid mixtures” in springermaterials (https://doi.org/10.1007/10047452_2). Copyright 1991 Springer-Verlag Berlin Heidelberg.
- [144] Teruya Ishihara, Jun Takahashi, and Takenari Goto. Optical properties due to electronic transitions in two-dimensional semiconductors (c n h 2 n+ 1 nh 3) 2 pbi 4. *Physical review B*, 42(17):11099, 1990.
- [145] RJ Elliott. Intensity of optical absorption by excitons. *Physical Review*, 108(6):1384, 1957.
- [146] G Marin, C Rincon, SM Wasim, Ch Power, and G Sanchez Perez. Temperature dependence of the fundamental absorption edge in cuinte 2. *Journal of applied physics*, 81(11):7580–7583, 1997.
- [147] Fouad El-Diasty, FA Abdel Wahab, Manal Abdel-Baki, and Safeya Ibrahim. Elliott model for optical absorption by exciton and two-photon absorption in zinc borophosphate glasses. *American Journal of Condensed Matter Physics*, 4(4):71–77, 2014.

- [148] Jin-Wook Lee, Sang-Hoon Bae, Yao-Tsung Hsieh, Nicholas De Marco, Mingkui Wang, Pengyu Sun, and Yang Yang. A bifunctional lewis base additive for microscopic homogeneity in perovskite solar cells. *Chem*, 3(2):290–302, 2017.
- [149] David K Ferry. *Semiconductor transport*. CRC Press, 2016.
- [150] Xiao Han, Yongshen Zheng, Siqian Chai, Songhua Chen, and Jialiang Xu. 2d organic-inorganic hybrid perovskite materials for nonlinear optics. *Nanophotonics*, 9(7):1787–1810, 2020.
- [151] Yen-Hung Lin, Pichaya Pattanasattayavong, and Thomas D Anthopoulos. Metal-halide perovskite transistors for printed electronics: challenges and opportunities. *Advanced Materials*, 29(46):1702838, 2017.
- [152] Daehee Seol, Ahreum Jeong, Man Hyung Han, Seongrok Seo, Tae Sup Yoo, Woo Seok Choi, Hyun Suk Jung, Hyunjung Shin, and Yunseok Kim. Origin of hysteresis in $\text{CH}_3\text{NH}_3\text{PbI}_3$ perovskite thin films. *Advanced Functional Materials*, 27(37):1701924, 2017.
- [153] Laura M Herz. Charge-carrier mobilities in metal halide perovskites: fundamental mechanisms and limits. *ACS Energy Letters*, 2(7):1539–1548, 2017.
- [154] Xiaoxi Wu, M Tuan Trinh, Daniel Niesner, Haiming Zhu, Zachariah Norman, Jonathan S Owen, Omer Yaffe, Bryan J Kudisch, and X-Y Zhu. Trap states in lead iodide perovskites. *Journal of the American Chemical Society*, 137(5):2089–2096, 2015.
- [155] Chuanzhao Li, Jin Yang, Fuhai Su, Junjun Tan, Yi Luo, and Shuji Ye. Conformational disorder of organic cations tunes the charge carrier mobility in two-dimensional organic-inorganic perovskites. *Nature communications*, 11(1):1–8, 2020.
- [156] Aihui Liang, Yao Gao, Reza Asadpour, Zitang Wei, Blake P Finkenauer, Linrui Jin, Jiaqi Yang, Kang Wang, Ke Chen, Peilin Liao, et al. Ligand-driven grain engineering of high mobility two-dimensional perovskite thin-film transistors. *Journal of the American Chemical Society*, 143(37):15215–15223, 2021.
- [157] Huihui Zhu, Ao Liu, Kyu In Shim, Jisu Hong, Jeong Woo Han, and Yong-Young Noh. High-performance and reliable lead-free layered-perovskite transistors. *Advanced Materials*, 32(31):2002717, 2020.
- [158] GK Reeves and HB Harrison. Obtaining the specific contact resistance from transmission line model measurements. *IEEE Electron device letters*, 3(5):111–113, 1982.
- [159] Hyeong Pil Kim, Maria Vasilopoulou, Habib Ullah, Salma Bibi, Anderson Emanuel Ximim Gavim, Andreia Gerniski Macedo, Wilson Jose da Silva, Fabio Kurt Schneider, Asif Ali Tahir, Mohd Asri Mat Teridi, et al. A hysteresis-free perovskite transistor with exceptional stability through molecular cross-linking and amine-based surface passivation. *Nanoscale*, 12(14):7641–7650, 2020.

List of Figures

1.1	Classification of perovskite material.	2
1.2	Crystal structure of 3D hybrid perovskite with the chemical formula of $\text{CH}_3\text{NH}_3\text{SnI}_3$, where methylammonium (CH_3NH_3^+) cations embedded in the space of corner-sharing $[\text{SnI}_6]^{4-}$ framework.	3
1.3	Three different types of LD hybrid perovskites based on crystallographic slicing of 3D perovskite through different crystal planes such as (100), (110), and (111).	4
1.4	The most popular (100) type LD perovskites, these can be future categorized into (a) RP, (b) DJ and (c) ACI phases based on type of organic spacer cation. Where RP phase contain single monoammonium cation as organic spacer, DJ phase consist of diammonium cation as organic spacer and ACI phase is a mixture of monoammonium and diammonium cations.	4
1.5	Crystal structure of 2D RP perovskite with chemical formula $[\text{CH}_3(\text{CH}_2)_3\text{NH}_3]_2\text{SnI}_4$. The butylammonium cations act as spacers between the layered inorganic framework.	5
1.6	Crystal structure of 2D perovskite with DJ phase, which consists of chemical formula $[\text{NH}_3\text{C}_{10}\text{H}_6\text{NH}_3]\text{PbI}_4$, where Naphthalene-1,5-diammonium ($[\text{NH}_3\text{C}_{10}\text{H}_6\text{NH}_3]^{2+}$) cations are spaced between inorganic layers, In contrast to RP phase, Van der Waals gap between the spacer cations has been eliminated due to single diammonium organic cation which connects between inorganic layers.	6
1.7	The crystal structure of 2D perovskite with ACI phase, which has a chemical formula of $[\text{C}(\text{NH}_2)_3][\text{CH}_3\text{NH}_3]\text{PbI}_4$, where mixed methylammonium (CH_3NH_3^+) and Guanidinium ($[\text{C}(\text{NH}_2)_3]^+$) cations are organized between the layers of inorganic cations.	7
1.8	The perovskite material decomposes into a precursor or 0D hydrate phase when exposed to heat, moisture, or UV light. The degradation of perovskite material causes a reduction in device efficiency and light absorption properties.	7
1.9	Degradation mechanism in hybrid tin-iodide perovskite when exposed to ambient air.	9

1.10	(a,b) Schottky and Frenkel defects, (c) channel in grain boundaries, (e) lattice dislocations, (g) softening of the lattice by lamination, and (f) strain-induced extended defects by piezoelectric effect are ion migration pathways in hybrid perovskites.	11
1.11	Over the past decade, there has been an exponential increase in the number of publications and citations on the topic of “2D halide perovskite materials”. Data collected from the web of science.	14
1.12	The organic cations have been reported in the literature as spacers in 2D tin-iodide hybrid perovskites.	16
1.13	The device structure of the 2D perovskite field-effect transistor in this research.	17
1.14	Illustration of the reported device structures in the hybrid perovskite field-effect transistor.	18
2.1	Overall process flow of device preparation.	22
2.2	Commonly used characterization methods for perovskites.	23
2.3	Sample analysis with an X-ray diffractometer.	24
2.4	2D GIWAXS pattern with scattering profile.	25
2.5	The shape of GIWAXS diffraction (a). Ring, (b). Arc, (c). Ellipse.	26
2.6	Absorption spectrum of $(\text{BA})_2(\text{MA})_{n-1}\text{Sn}_n\text{I}_{3n+1}$ when n becomes infinity it is considered as 3D perovskite. A shift in the optical bandgap of the material is observed, with 3D perovskites having a bandgap of 1.20 eV, while pure 2D perovskites have a higher bandgap of 1.83 eV.	27
2.7	The absorption spectrum of 2D hybrid Sn(II)-based perovskite with bench-marked organic cation PEA.	28
3.1	Illustration of 2D quantum well structure and exciton binding energy band diagram.	30
3.2	The absorption spectrum of 2D alkyl ammonium perovskites films, prepared at a concentration of 0.2 M in DMF:DMSO (1:1), spin coated at 4000 rpm and annealed at 100 °C for 10 minutes.	32
3.3	Absorbance spectrum and corresponding Elliot fit curves are used to calculate the optical band gap (E_g) and exciton binding energy (E_b) of 2D perovskite.	34
3.4	Optical microscopy images of perovskite films, prepared at a concentration of 0.1 M in DMF, spin-coated at 4000 rpm and annealed at 100 °C for 10 minutes. The optical microscopy images of alkyl ammonium perovskites prepared with different recipes are attached in appendix A.	35

3.5	Atomic force microscopy images of different perovskite films, prepared at a concentration of 0.1 M in DMF, spin coated at 4000 <i>rpm</i> and annealed at 100 °C for 10 minutes. The AFM images of alkyl ammonium perovskites prepared with different recipes are attached in appendix B.	36
3.6	X-ray diffraction patterns of perovskite films with different alkyl ammonium cations, prepared at a concentration of 0.2 M in DMF:DMSO (1:1), spin coated at 4000 <i>rpm</i> and annealed at 100 °C for 10 minutes.	38
3.7	The calculated inter-layer distances of alkyl ammonium-based perovskites.	39
3.8	GIWAXS images of perovskite films, prepared at a concentration of 0.2 M in DMF, spin-coated at 4000 <i>rpm</i> and annealed at 100 °C for 10 minutes. The GIWAXS images of alkyl ammonium perovskites prepared with different recipes are attached in appendix C.	40
3.9	Experimental GIWAXS diffraction images and corresponding simulated pattern with miller indices.	41
3.10	Transfer characteristics of 2D alkyl ammonium based perovskite FETs measured at (a) 100 K, (b) 200 K, and (c) 295 K. The channel length and width are $L = 80 \mu\text{m}$, $W = 1000 \mu\text{m}$. The gray curve (I_g) shows the leakage current of the device prepared at 0.1 M in DMF, spin coated at 4000 <i>rpm</i> , and annealed at 100 °C for 10 minutes. The transfer characteristics of alkyl ammonium perovskite transistors prepared with different recipes are attached in appendix D.	43
3.11	The charge-carrier mobility of tin-iodide-based 2D hybrid perovskite FETs with a different number of carbon atoms in alkyl ammonium spacers.	46
3.12	Intrinsic mobility of lead-iodide-based 2D hybrid perovskites with a different number of carbon atoms in alkyl ammonium spacers.	47
3.13	The calculated contact resistance of the alkyl ammonium spacers.	48
5.1	Optical microscopy images of perovskite films, which was prepared at a concentration of 0.2 M in DMF, spin coated at 4000 <i>rpm</i> and annealed at 100 °C for 10 minutes.	vii
5.2	Optical microscopy images of perovskite films, which was prepared at a concentration of 0.2 M in DMF:DMSO (1:1), spin coated at 4000 <i>rpm</i> and annealed at 100 °C for 10 minutes.	viii
5.3	Atomic force microscopy images of different perovskite films, which was prepared at a concentration of 0.2 M in DMF, spin coated at 4000 <i>rpm</i> and annealed at 100 °C for 10 minutes.	viii
5.4	Atomic force microscopy images of different perovskite films, which was prepared at a concentration of 0.2 M in DMF:DMSO (1:1), spin coated at 4000 <i>rpm</i> and annealed at 100 °C for 10 minutes.	ix

- 5.5 GIWAXS images of perovskite films, which was prepared at a concentration of 0.1 M in DMF, spin coated at 4000 *rpm* and annealed at 100 °C for 10 minutes. x
- 5.6 GIWAXS images of perovskite films, which was prepared at a concentration of 0.2 M in DMF:DMSO (1:1), spin coated at 4000 *rpm* and annealed at 100 °C for 10 minutes. xi
- 5.7 Transfer characteristics of 2D alkyl ammonium based perovskite FETs measured at (a) 100 *K*, (b) 200 *K*, and (c) 295 *K*. The channel length and width are $L = 80 \mu m$, $W = 1000 \mu m$. The gray curve (I_g) shows the leakage current of the device prepared at 0.2 M in DMF, spin coated at 4000 *rpm*, and annealed at 100 °C for 10 minutes. xiii
- 5.8 Transfer characteristics of 2D alkyl ammonium based perovskite FETs measured at (a) 100 *K*, (b) 200 *K*, and (c) 295 *K*. The channel length and width are $L = 80 \mu m$, $W = 1000 \mu m$. The gray curve (I_g) shows the leakage current of the device prepared at 0.2 M in DMF:DMSO (1:1), spin coated at 4000 *rpm*, and annealed at 100 °C for 10 minutes. xv

List of Tables

1.1	Effects of ion migration in hybrid perovskite are sometimes referred to as a "double-edged sword" because all the consequences of ion migration in semiconductor devices are not detrimental.	12
3.1	Dielectric constant values of alkyl ammonium cations, as the number of carbon atoms in the chain increases, the dielectric constant decreases proportionally.	32
3.2	Surface roughness and the average size of grain boundaries of perovskite films.	37
3.3	Calculated inter-layer spacing of perovskite with different alkyl ammonium cations.	39
3.4	Consolidated summary of charge carrier mobility for alkyl ammonium-based perovskite field-effect transistors fabricated with different precursor recipes (A, B & C).	45
3.5	Consolidated summary of threshold voltage for alkyl ammonium-based perovskite FETs fabricated with different precursor recipes (A, B & C).	49

List of Acronyms

OIHP	Organic inorganic hybrid perovskite
PCE	Power conversion efficiency
2D	Two dimension
3D	Three dimension
RP	Ruddlesden-Popper
DJ	Dion-Jacobson
ACI	Alternating cation inter-layer
PA	Propylammonium
BA	Butylammonium
PentA	Pentylammonium
HxA	Hexylammonium
HeptA	Heptanammonium
PEA	Phenethylammonium
XRD	X-ray diffraction
GIWAXS	Grazing incidence wide angle X-ray scattering
AFM	Atomic force microscopy
KPFM	Kelvin probe force microscopy
XPS	X-ray photoemission spectroscopy
FET	Field-effect transistor

Chapter 5

Appendices

A Optical microscopy

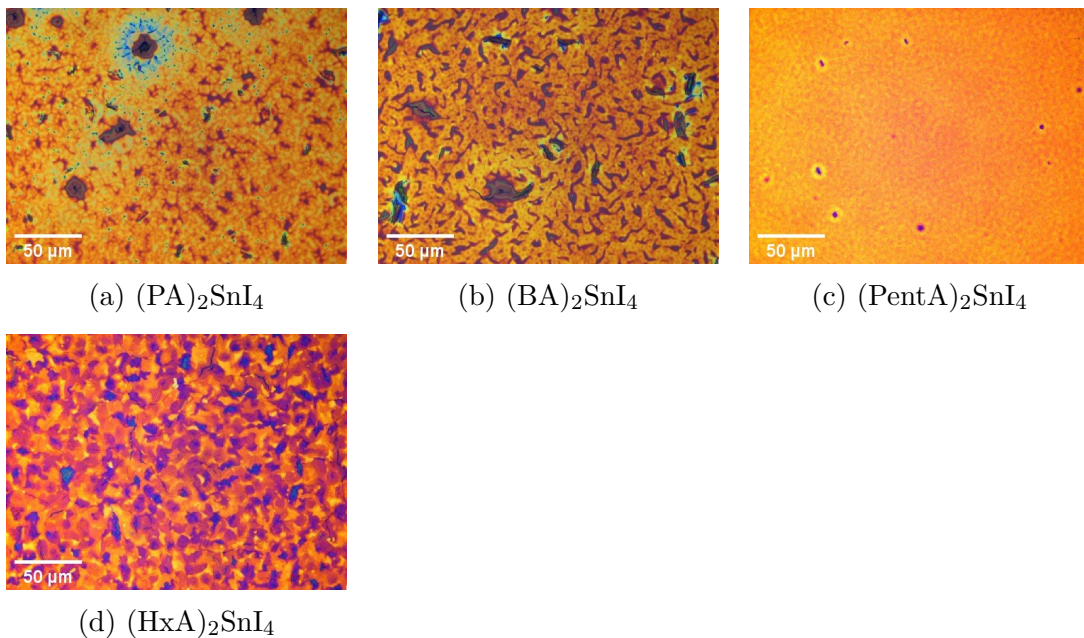


Figure 5.1: Optical microscopy images of perovskite films, which was prepared at a concentration of 0.2 M in DMF, spin coated at 4000 *rpm* and annealed at 100 °C for 10 minutes.

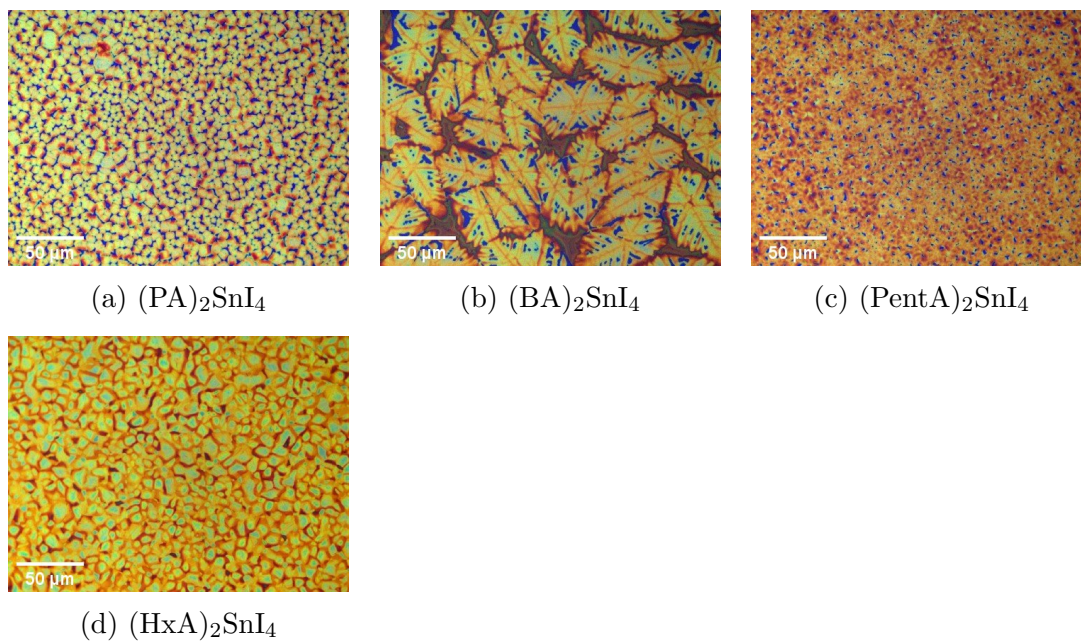


Figure 5.2: Optical microscopy images of perovskite films, which was prepared at a concentration of 0.2 M in DMF:DMSO (1:1), spin coated at 4000 *rpm* and annealed at 100 °C for 10 minutes.

B Atomic force microscopy

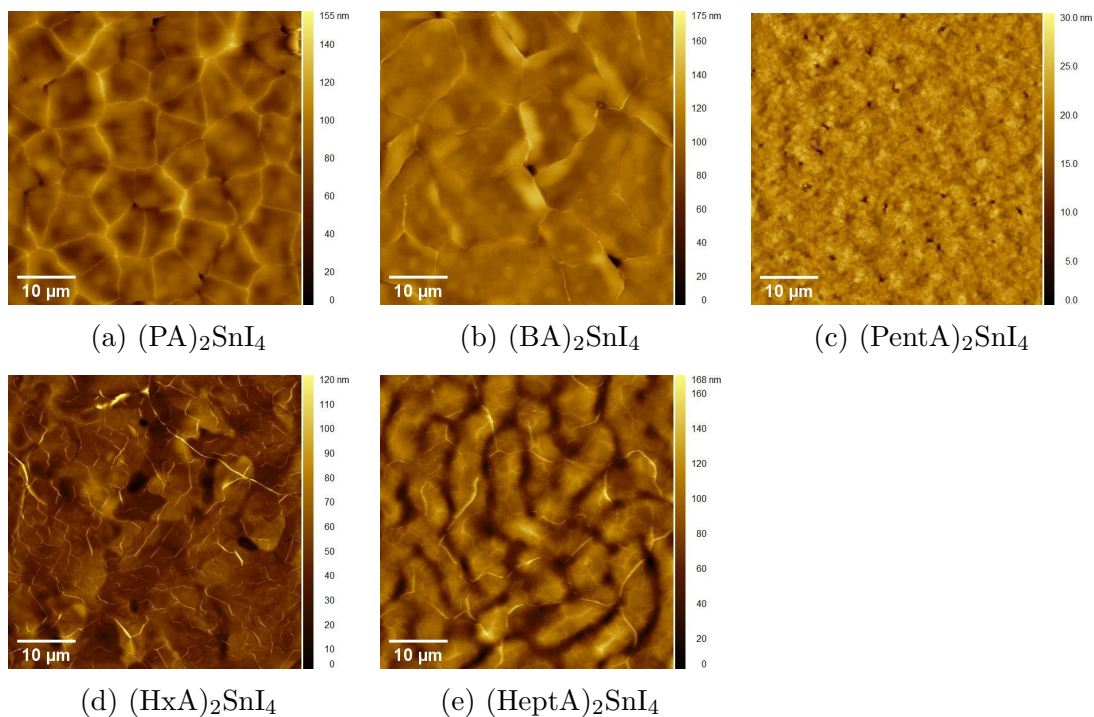


Figure 5.3: Atomic force microscopy images of different perovskite films, which was prepared at a concentration of 0.2 M in DMF, spin coated at 4000 *rpm* and annealed at 100 °C for 10 minutes.

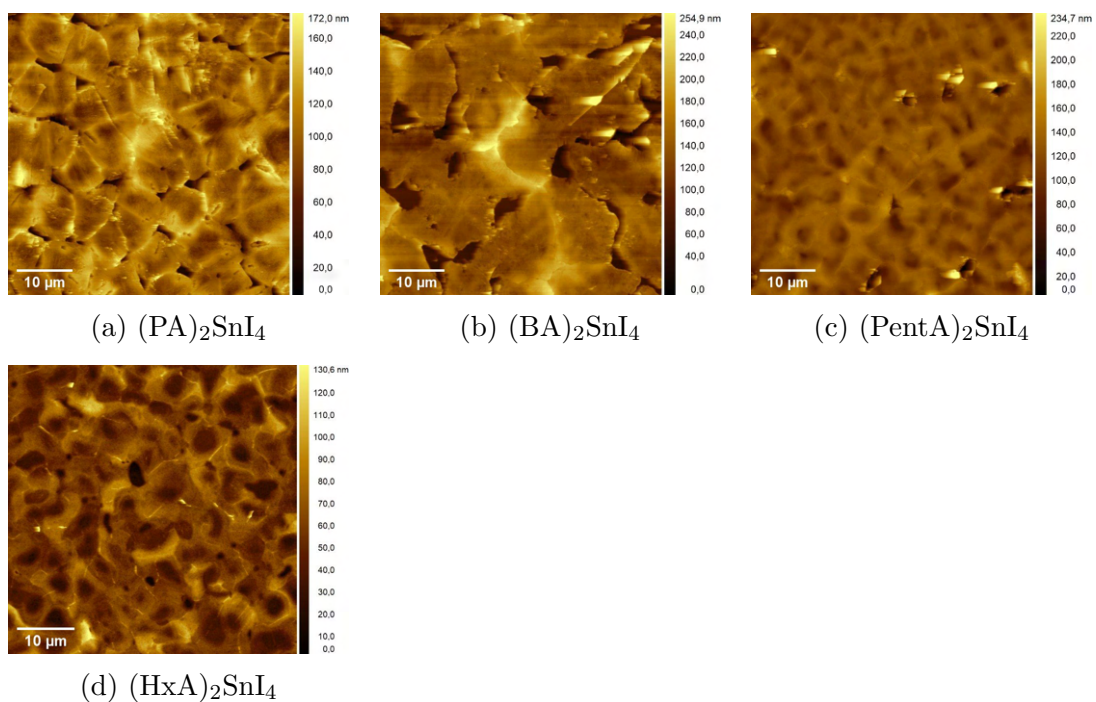


Figure 5.4: Atomic force microscopy images of different perovskite films, which was prepared at a concentration of 0.2 M in DMF:DMSO (1:1), spin coated at 4000 *rpm* and annealed at 100 °C for 10 minutes.

C Grazing incidence wide angle X-ray scattering

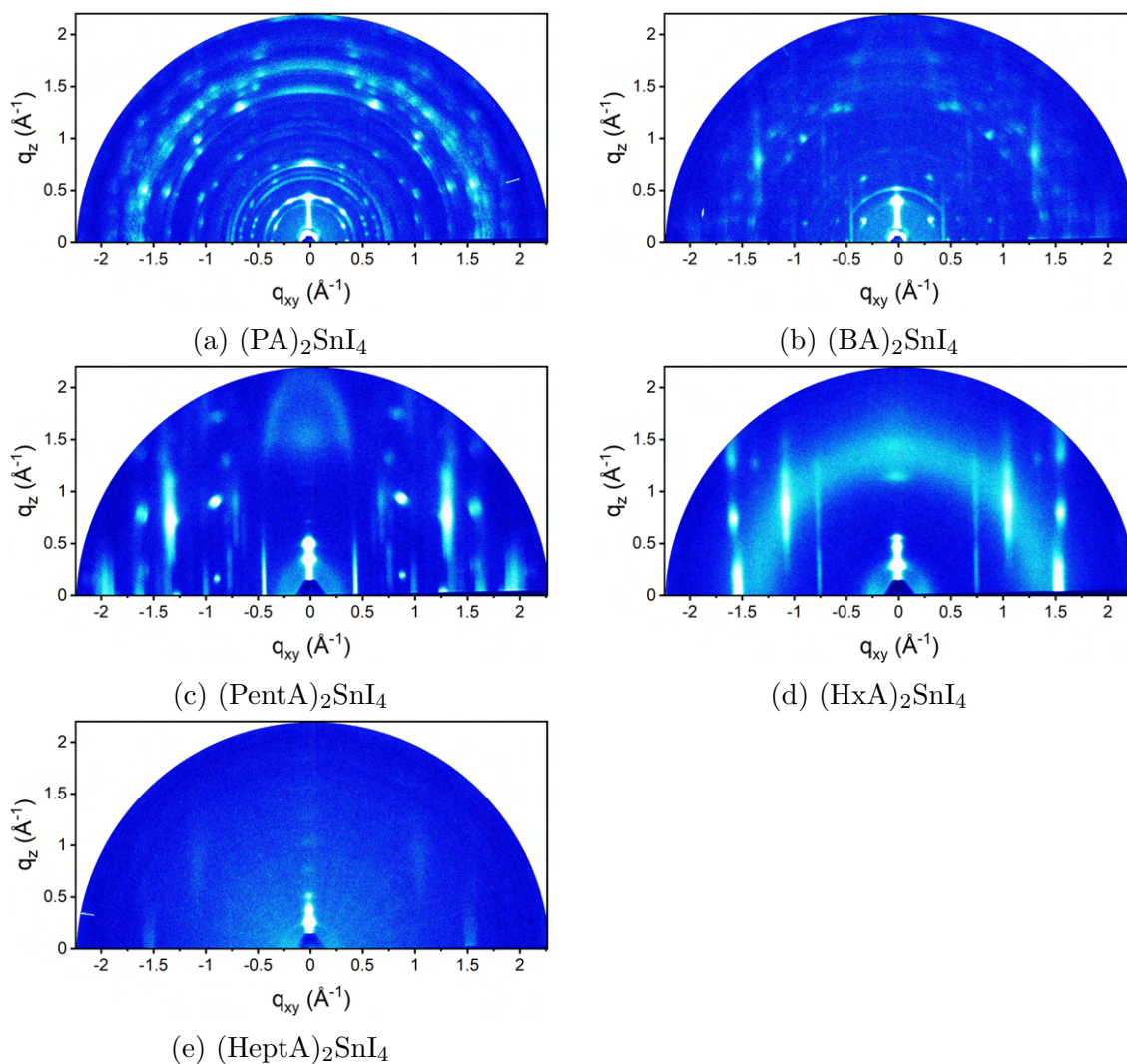


Figure 5.5: GIWAXS images of perovskite films, which was prepared at a concentration of 0.1 M in DMF, spin coated at 4000 *rpm* and annealed at 100 °C for 10 minutes.

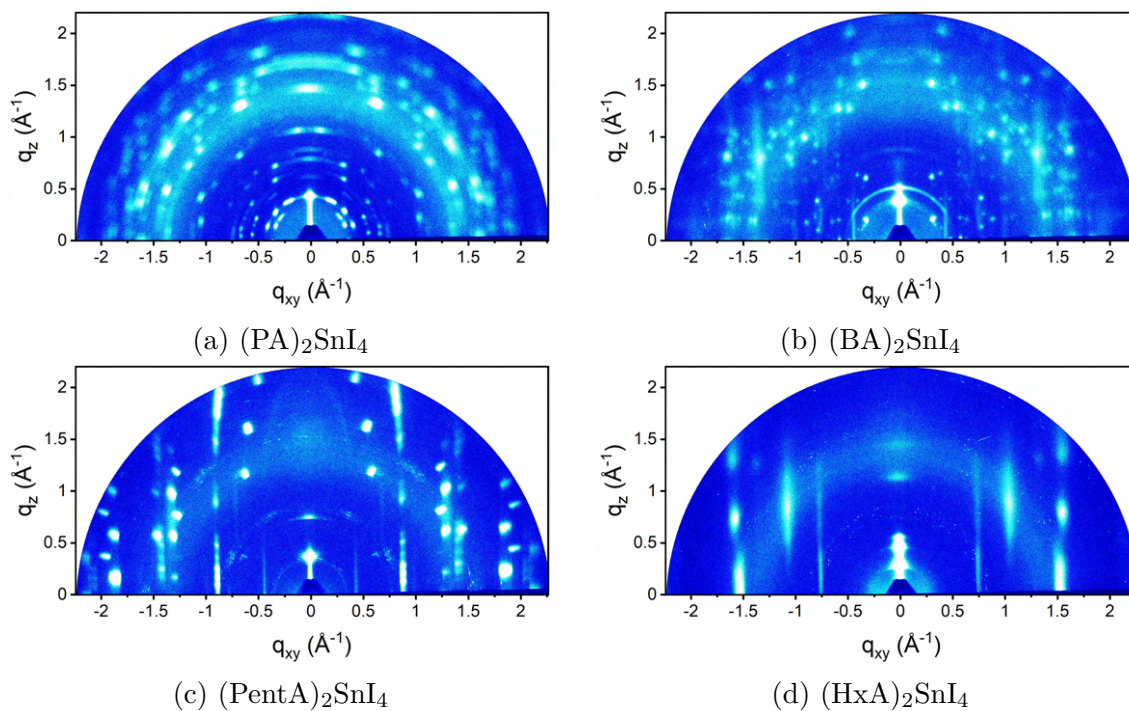
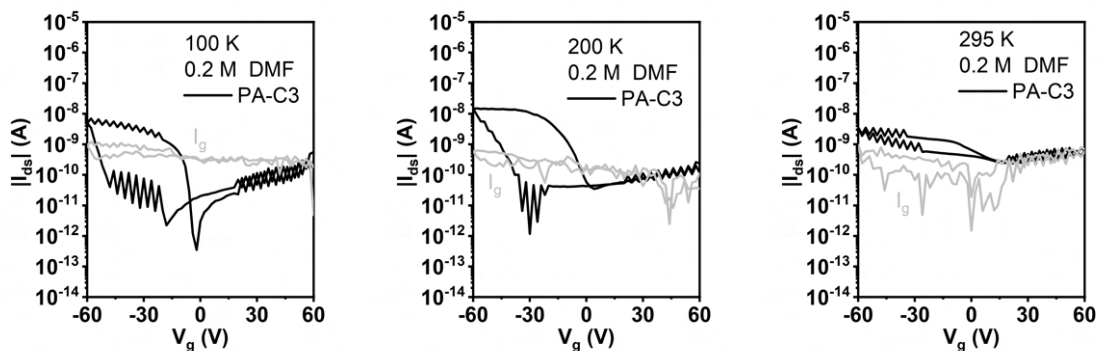
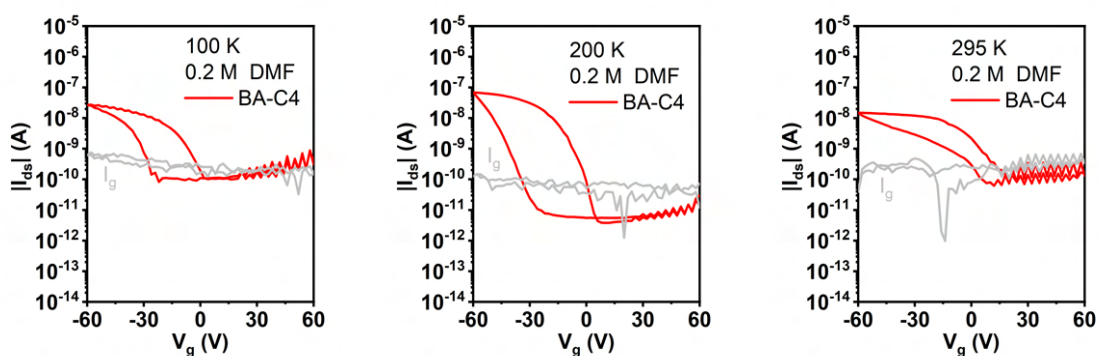
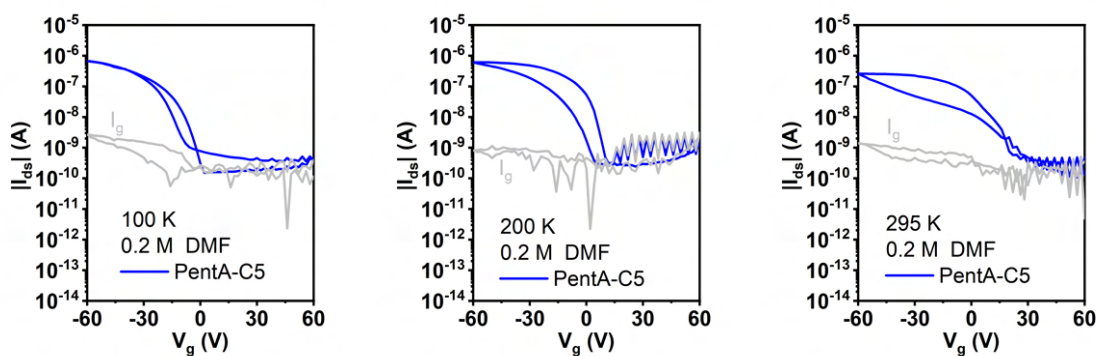


Figure 5.6: GIWAXS images of perovskite films, which was prepared at a concentration of 0.2 M in DMF:DMSO (1:1), spin coated at 4000 *rpm* and annealed at 100 °C for 10 minutes.

D Device measurement

(a) $(\text{PA})_2\text{SnI}_4$ (b) $(\text{BA})_2\text{SnI}_4$ (c) $(\text{PentA})_2\text{SnI}_4$

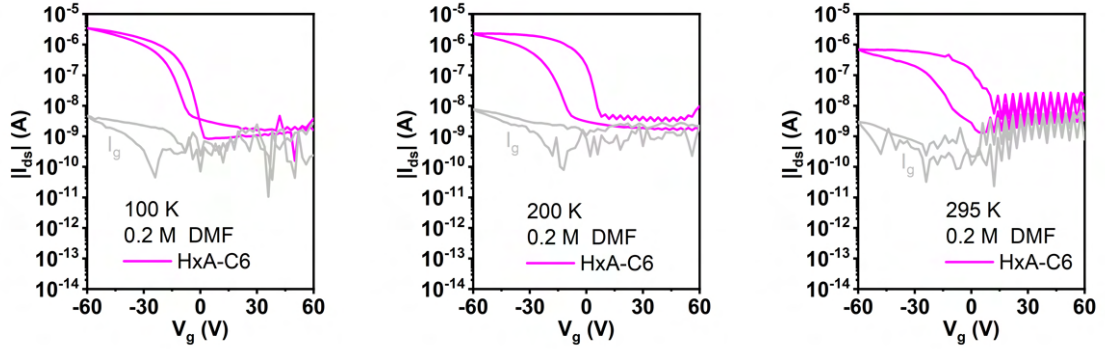
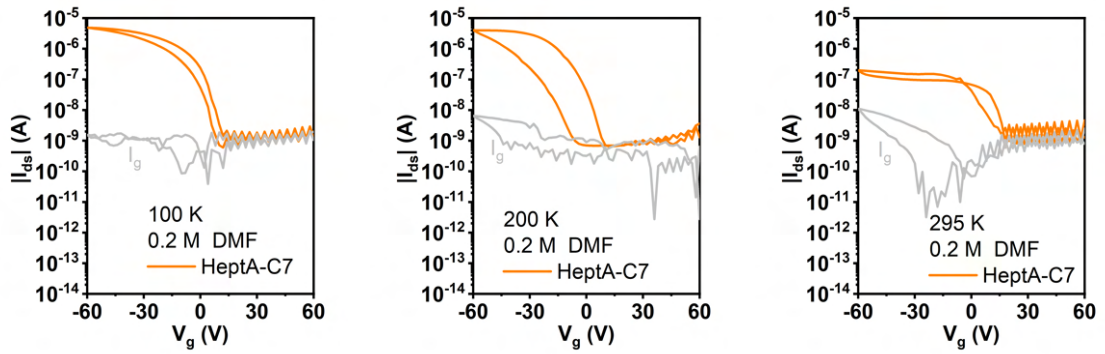
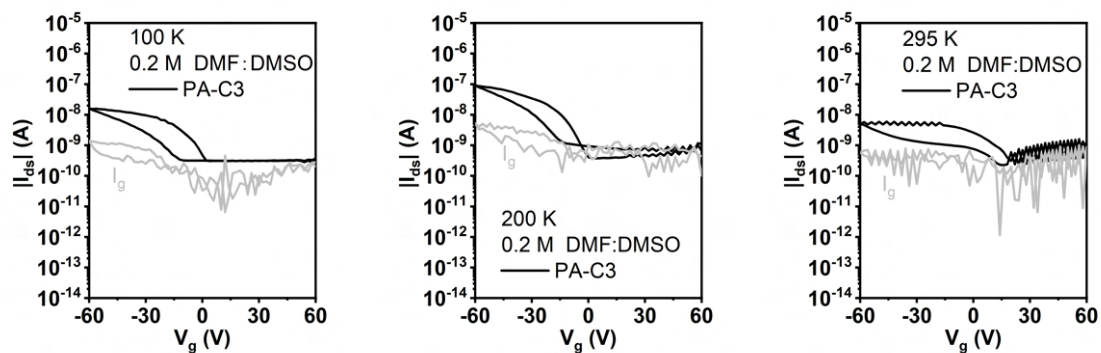
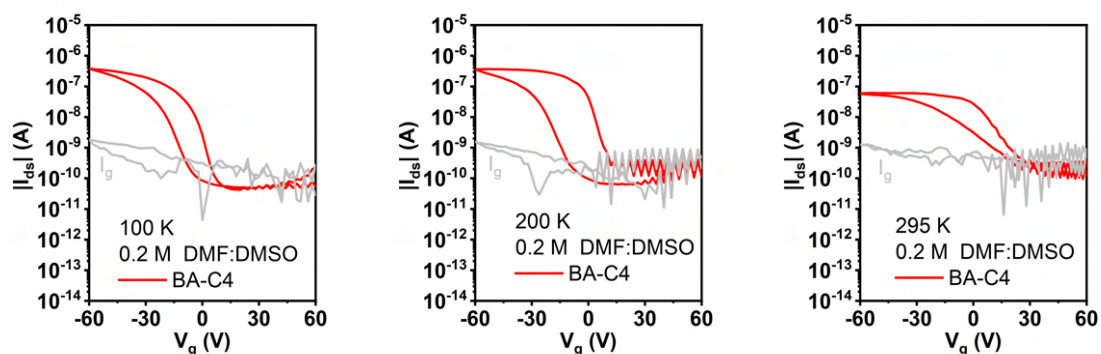
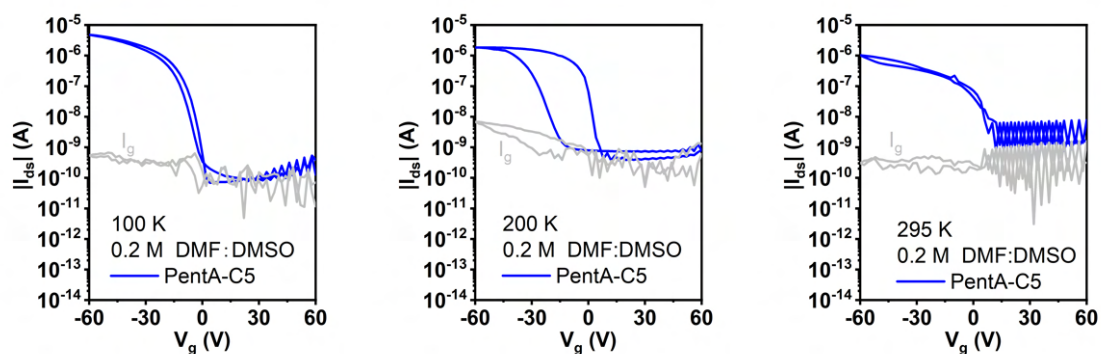
(d) $(\text{HxA})_2\text{SnI}_4$ (e) $(\text{HeptA})_2\text{SnI}_4$

Figure 5.7: Transfer characteristics of 2D alkyl ammonium based perovskite FETs measured at (a) 100 K, (b) 200 K, and (c) 295 K. The channel length and width are $L = 80 \mu\text{m}$, $W = 1000 \mu\text{m}$. The gray curve (I_g) shows the leakage current of the device prepared at 0.2 M in DMF, spin coated at 4000 rpm, and annealed at 100 °C for 10 minutes.

(a) $(PA)_2SnI_4$ (b) $(BA)_2SnI_4$ (c) $(PentA)_2SnI_4$

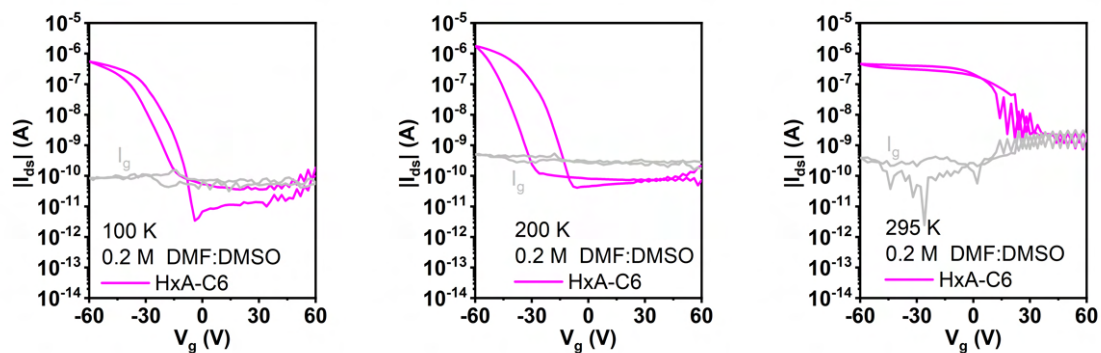
(d) $(\text{HxA})_2\text{SnI}_4$

Figure 5.8: Transfer characteristics of 2D alkyl ammonium based perovskite FETs measured at (a) 100 K, (b) 200 K, and (c) 295 K. The channel length and width are $L = 80 \mu\text{m}$, $W = 1000 \mu\text{m}$. The gray curve (I_g) shows the leakage current of the device prepared at 0.2 M in DMF:DMSO (1:1), spin coated at 4000 rpm, and annealed at 100 °C for 10 minutes.

Declaration of originality

I hereby declare that this thesis was created autonomously without using other than the stated references. All parts which are cited directly or indirectly are marked as such. This thesis has not been used in the same or similar forms in parts or total in other examinations.

Signature